QUANTIFYING CONTACT FORCE ARTEFACT IN NEAR INFRARED SPECTROSCOPY

by

Timothy Schwab

BASc, University of British Columbia, 2003
MASc, University of British Columbia, 2006
BEd, University of British Columbia, 2009

DISSERTATION SUBMITTED IN PARTIAL FULFILLMENT OF
THE REQUIREMENTS FOR THE DEGREE OF
DOCTOR OF PHILOSOPHY
IN
HEALTH SCIENCES

UNIVERSITY OF NORTHERN BRITISH COLUMBIA

February 2021

ABSTRACT

Transcutaneous near infrared spectroscopy (NIRS) of muscle requires coupling between the device and the skin. An unfortunate by-product of this coupling is contact force artefact, where the amount of contact force between the device and the skin affects measurements. Contact force artefact is well known, but largely ignored in most NIRS research.

We performed preliminary investigations of contact force artefact to quantify tissue behaviour to inform future NIRS designs. Specifically, we conducted three studies on contact force artefact: (i) an experimental investigation of static load at varied levels of contact force and muscle activation, (ii) an experimental investigation of oscillating load at varied levels of contact force and frequency, and (iii) a Monte Carlo simulation of photon propagation through skin, adipose tissue, and muscle.

Our results confirmed that contact force artefact is a confounding factor in NIRS muscle measurements because contact force affects measured hemoglobin concentrations in a manner consistent with muscle contractions. Further, the effects of contact force are not altered by muscle contraction and a likely candidate for the mechanism responsible for contact force artefact is the viscoelastic compression of superficial tissues (skin and adipose) during loading. Simulation data suggests that adipose tissue plays a key role in diffuse reflectance of photons, so any compression of the superficial tissues will affect the reflected signal. Further research is required to fully understand the mechanisms behind contact force artefact, which will, in turn, inform future NIRS device designs.

TABLE OF CONTENTS

LIST OF TABLES

LIST OF FIGURES

LIST OF ABBREVIATIONS

AD	Average depth	MVC	Maximum voluntary contraction
BB	Biceps brachii	μ_a	Absorption coefficient
CAM	Cyclic amplitude	μ_s	Scattering coefficient
CAV	Cyclic average	μ_s'	Reduced scattering coefficient
c_F	Regression coefficient for contact force	n	Index of refraction
c_{MVC}	Regression coefficient for MVC	NAM	Normalized absorption in muscle
CR	Cyclic reoxygenation rate	NIRS	Near infrared spectroscopy
CW	Continuous wave	ξ	Random number between 0 and 1
DPF	Differential pathlength factor	O_2Hb	Oxygenated hemoglobin
ε	Extinction coefficient	PC	Peak changes
ED	Extensor digitorum	PLM	Path length in muscle
F	Contact force	SDS	Source detector separation
FR	Final reoxygenation rate	SCM	Sternocleidomastoid
g	Anisotropy coefficient	STT	Superficial tissue thickness
G	Constant representing other light losses	tHb	Total hemoglobin
Hb	Hemoglobin (inclusive of myoglobin in muscle)	TOI	Tissue oxygenation index
HHb	Deoxygenated hemoglobin	VL	Vastus lateralis
L	Photon step size		

DEDICATION

This work is dedicated to my children:

Sophia, Owen, Kaitlin and Matthew

Always keep learning and exploring

ACKNOWLEDGEMENTS

Thank you to all those who made it possible for me to complete my hobby thesis. First, I need to thank my wife, Janis, who tolerated my late nights and associated tired days as I completed this work.

Second, thank you to all those at UNBC who supported my learning. Specifically, I would like to thank my supervisors, Dr. Harris and Dr. Aravind, and all those who collaborated with me on my experiments.

PREFACE

An introduction to my research requires an introduction to me. My academic background is in mechanical and biomedical engineering, so I am interested in device design and optimization. My previous research areas include orthopaedic biomechanics, orthopaedic device design, biological materials testing and forensic analysis. Near infrared spectroscopy (NIRS) was a new field to me when I started my PhD and over the past few years I developed a keen interest in developing non-invasive measurement modalities.

In my future career, I hope to continue to develop NIRS systems and NIRS analysis while expanding my expertise to other modalities in hopes of creating non-invasive multimodal measurements. For example, NIRS, ultrasound, electromyography, motion capture, and even MRI provide complementary information that can be combined to offer a better understanding of *in vivo* processes.

Lastly, I would like to explain why I chose to write a paper-based thesis. Peer-reviewed journal articles are the main modality for scientific knowledge transfer in my field, and very few manuscripts reference full length monographs; therefore, I believe it makes sense to write my thesis in a way that will lead directly to peer-reviewed journal articles.

CHAPTER 1: INTRODUCTION

1.1 BACKGROUND

Currently, near infrared spectroscopy (NIRS) is more commonly applied within academic research communities than it is applied clinically, though researchers are keen to translate their knowledge to the clinical realm[1-3]. There are a few reasons why NIRS has not seen a large clinical uptake, but large inter-subject variability seems to the most salient among them. I believe that superficial tissues (skin and adipose tissue) and associated measurement artifacts are a potential source of inter-subject variability during transcutaneous muscle measurements. My research explores some of the effects of superficial tissues on NIRS measurements with specific focus on the effects on contact force. I view these initial studies as the first steps in my research career that will improve NIRS devices to the point where they are a valued and integral part of clinical imaging.

The following section is intended to provide context and background for readers who are unfamiliar with NIRS. NIRS experts can skip the following section and proceed to the 1.3 Research Objectives on page 11.

1.2 NEAR INFRARED SPECTROSCOPY

NIRS is a non-invasive, non-ionising imaging modality that has been researched and refined since 1977[4,5]. Almost all NIRS devices operate under the

principle of diffuse reflectance, where light is emitted from a source, photons are diffusely scattered within tissue and some are re-emitted into a detector. See Figure 1 for a schematic representation of this process.

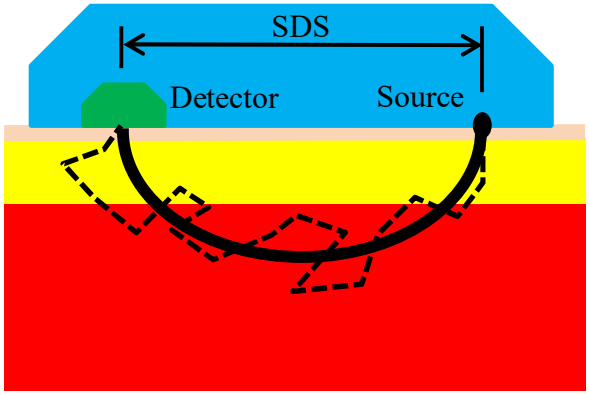

Figure 1: Schematic representation of a NIRS device with one source (emitter) operating in diffuse reflectance. Re-emitted light, on average, follows a 'banana-shape' path in a homogenous medium (solid line) with maximum absorption occurring at a depth roughly 20% to 30% of the source-detector distance (SDS)[6], although each photon will follow a random path (dashed line) influenced by the reduced scattering coefficient. This idealised schematic is not necessarily representative of true photon paths in layered media and is generated based on homogeneous medium data.

The exact path of individual photons is unknown, though some aggregate metrics (for example, pathlength) can be determined with time-domain and frequency-domain systems[7-9]. The two main factors affecting photon propagation within tissue are geometry and tissue optical properties. When source-detector separation (SDS, see Figure 1) increases, the average photon path penetrates deeper into tissue, though the exact penetration depths *in vivo* are poorly defined. Experimental phantom investigations[6,10,11] and computer simulations[12-18] provide estimates of expected propagation paths.

Biological tissue optical properties also influence photon propagation. As a photon propagates in tissue, it interacts with the tissue through both scattering and absorption, which are quantified by the reduced scattering coefficient (μ_s', accounting for both scattering and material anisotropy) and the absorption coefficient (μ_a). Cell and nuclear membranes are thought to be a source of scattering in human tissue[19] though cellular organelles and collagen fibres likely play a more important role for near infrared wavelengths[20].

The chromophores (molecules that absorb specific wavelengths of light) vary with wavelength, and, in the near infrared spectrum, oxygenated hemoglobin (O_2Hb) and deoxygenated hemoglobin (HHb) are thought to be the main chromophores (see 1.2.1Assumptions and Limitations section below) and the summation of these two values is called the total hemoglobin (tHb). Higher μ_a causes more photons to be absorbed in the tissue so less light is re-emitted into a detector, and lower μ_a increases the intensity of re-emitted light. Figure 2 shows the absorption of O_2Hb and HHb[21] plotted against typical NIRS wavelengths.

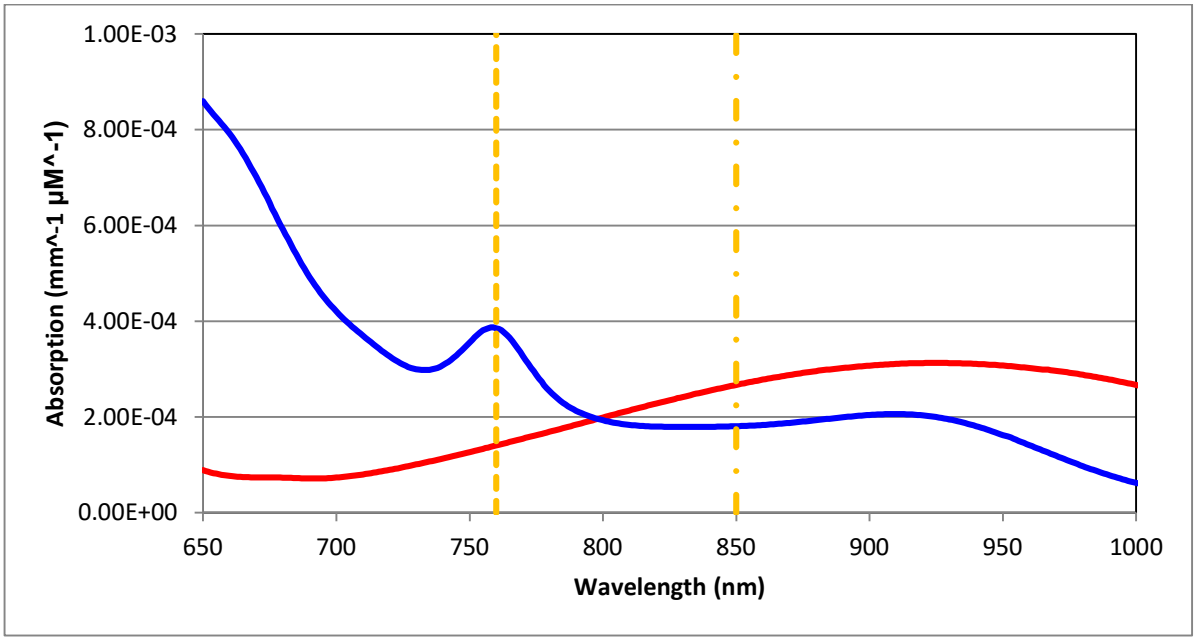

Figure 2: Specific absorption of O_2Hb (red line) and HHb (blue line)[21]. Wavelengths used by NIRS devices are chosen to maximise differences in hemoglobin absorption while minimising the absorption of water. Wavelengths utilized by the OxiTor (yellow lines), the NIRS device during experimental data acquisition, are plotted for reference.

If the interrogated tissue contains muscle, such as the measurements taken in the experimental portions of this thesis, myoglobin will also contribute to the light absorption in a similar fashion to hemoglobin (Hb) such that the two contributions to the absorbance are indistinguishable. At present, the contribution of myoglobin to NIRS data is unknown and estimates range from less than 10%[22] to approximately 70%[23]. For clarity, the term Hb used in this thesis implies an aggregate of both Hb and myoglobin within muscle tissue.

As discussed above, light is both scattered away and absorbed by the tissue causing an attenuation of the light intensity before it enters the detector. While scattering is thought to be roughly constant once a probe is in position[24,25], the

absorption changes as Hb concentrations changes. Differences in detected intensities are used to determine the relative amount of O_2Hb and HHb using a modified Beer-Lambert's Law[26] as described by Equation (1).

$$(1) \qquad \boldsymbol{A = \left(\varepsilon_{O_2Hb}[O_2Hb] + \varepsilon_{HHb}[HHb]\right) \cdot SDS \cdot DPF + G}$$

Where:

A is the light extinction, which is the log of the ratio of transmitted intensity to detected intensity ($\log\frac{I_o}{I}$)

ε_{O_2Hb} is the extinction coefficient for O_2Hb ($mm^{-1}\mu M^{-1}$)

ε_{HHb} are the extinction coefficient for HHb ($mm^{-1}\mu M^{-1}$)

$[O_2Hb]$ is the concentration of O_2Hb (μM)

$[HHb]$ is the concentration of HHb (μM)

SDS is the source-detector separation (mm)

DPF is the differential path length factor

G is a factor accounting for other light losses

Concentrations of O_2Hb and HHb can be used to compute total hemoglobin (tHb) through simple addition. The above method of interpreting signal attenuation with a modified Beer-Lambert Law has been implemented in many studies and it is an appropriate model to determine Hb concentrations using diffuse reflectance; however, the method requires some assumptions and has associated limitations.

1.2.1 ASSUMPTIONS AND LIMITATIONS

Near infrared spectroscopy is subject to certain assumptions and limitations and many of the following concerns about NIRS methodology are areas of active research. The main assumption required for calculations of O_2Hb and HHb is that both O_2Hb and HHb are the primary chromophores in the tissue at the specified wavelengths. This is not entirely true because, in addition to O_2Hb and HHb, water is an absorber in the near infrared spectrum. To minimize error, wavelengths are selected that minimize water absorption and maximize Hb absorption, or water content is estimated (for example, the OxiplexTS made by ISS Inc. assumes a user-defined water content with a default of 70%). Despite careful wavelength selection, there is potential for NIRS measurements to be affected by sweat. Other potential absorbers (for example, cytochrome C oxidase[21,27] or carboxyhemoglobin) are ignored during calculations because their relative contributions are deemed negligible[28] or coupled[29] to Hb concentration. Additionally, natural skin pigmentation, tattoos, or the presence of hair can alter subject-specific absorption. The variation of the properties of superficial tissues increases inter-subject variation a lead most NIRS researchers to monitor relative changes in Hb. Based on the modified Beer-Lambert law, all NIRS devices are capable of computing relative changes in Hb, though the majority of systems are not capable of determining absolute values.

Only time-domain and frequency-domain systems are capable of providing absolute Hb concentrations because they are capable of estimating DPF. Continuous wave systems, like the OxiTor M2 (Pathonix Innovation Inc., Vancouver, Canada) can only estimate DPF based on published values, so absolute values can not be

computed with accuracy. Instead, Hb concentrations changes are reported with reference to a steady-state baseline. Baseline values differ depending on tissue composition and physiologic demands, so between-subject baselines can not be compared. For example, subjects with different superficial tissue thickness (STT, the combined thickness of skin and subcutaneous adipose tissue) over muscle will have different signal attenuation, so their baseline values will be different.

Adipose tissue thickness (subcutaneous) is the main source of between-subjects STT variance, and is a major confounding factor of NIRS muscle Hb data because light is highly scattered in adipose tissue[30]. The contributions of intramyocellular lipids are typically disregarded because the concentrations are low enough[31,32] to be deemed negligible. Larger STT is associated with an underestimation of Hb concentrations (O_2Hb, HHb, and tHb)[33,34]. In practice, all NIRS measurements should be accompanied by a measurement of adipose tissue thickness using ultrasound, MRI, broadband NIRS or skinfold calliper. Ultrasound may be considered the gold standard, but ultrasound has been correlated with each of these other modalities, which facilitates computational corrections[33]. Algorithms used to correct for the effects of adipose tissue thickness on NIRS data are currently based on a combination of experimental data, numerical models[35,36] and unverified physiologic assumptions[37]. Despite the importance of adipose tissue thickness, most researchers do not apply corrective calculations because there is no commonly accepted method. Instead, NIRS research is typically conducted on subjects with minimal STT.

Another major limitation of diffuse reflectance NIRS devices is the ambiguous propagation of light through *in vivo* tissue. As discussed above, exact penetration depth of near infrared light within tissue is poorly understood. Maximum NIRS penetration depths are commonly quoted to be roughly 50% of the SDS[38,39], though experiments based on homogeneous tissue phantoms[6,10,11] suggest that the average photon penetration depth is less than 50% SDS. Qualitative interpretation of these results suggests that mean penetration depth is likely closer to 30% SDS, though exact values have not been reported. Monte Carlo simulations of cerebral NIRS suggest a similar penetration depth of approximately 30% SDS[12]. Experiments[6,10] and simulations[12] produced spatial sensitivity maps suggest that the distribution of light penetration depth is skewed toward shallow tissue and the most probable penetration depth may even be less than 30% SDS. A schematic of depth sensitivity in a tissue phantom is provided in Figure 3 for clarity, though current research has not fully quantified the effects of layered media during NIRS muscle measurements.

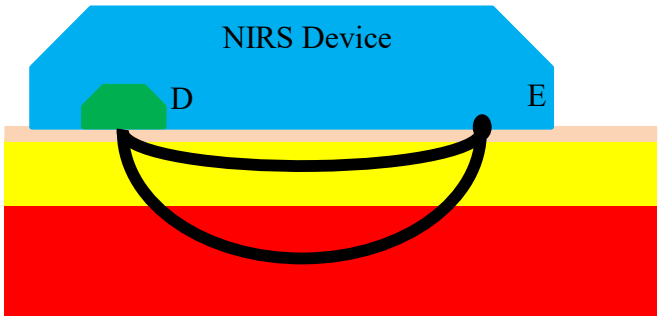

Figure 3: Schematic depicting idealized penetration depths based on experimental work in tissue phantoms. Photons are thought to propagate within the banana shape region between the two solid black curved lines that connect the emitter (E) and the detector (D), though the highly scattering effects of the adipose tissue layer may skew the penetration depths to smaller values.

In vivo penetration depths are very difficult to estimate without making assumptions about tissue properties and photon path lengths based on published data[7,8,13]. Both tissue properties and differential path length factors have high variation, so many researchers run numerical simulations to estimate penetration depth. Unfortunately, most light propagation simulations[12,14,15] focus on cerebral tissue rather than on muscle, so light penetration within muscle is relatively poorly understood. Additional insight into probable penetration depths within muscle could be collected by changing the gate times on a time-domain NIRS device because time of flight can be related to light penetration depth[40]; however, there is no time-domain NIRS device available at the University of Northern British Columbia.

Despite the ambiguity of NIRS penetration depth, research is being conducted to eliminate the contribution of superficial tissue to hemodynamic data, though most of this research is focused on cerebral NIRS. Scholkmann et al.[41] provide an in-depth description of techniques used in near infrared imaging to eliminate superficial noise. Briefly, a short-distance (roughly 5 mm SDS) optode is added in close proximity[42] to a typical-distance optode (SDS of roughly 30 to 40 mm). Data from both short- and long-separation optodes are processed to determine hemodynamic values, and then a numerical analysis is performed under the assumption that the shallow penetration (short optode) hemodynamic data can be subtracted from the deep (long optode) data. Algorithms used to determine the relative weighting of each signal rely on least squares regression[43-45], physiologic assumptions[46], or adaptive filtering[16,47,48]. These subtraction techniques are thought to remove systemic noise (for example, heart rate or ventilation rate) that presents in superficial tissues (by, for example, skin blood

flow[49]). In theory, superficial filtering may be able to remove demonstrated effects of temperature and sweat on NIRS data[50]. Unfortunately, the superficial filters are primarily focused on cerebral measurements and have not been implemented in muscle measurements.

Near infrared spectroscopy measurements on muscle differ slightly from cerebral measurements because tissue compliance is different. In cerebral NIRS, the skull prevents deeper tissues from deforming under load, so filtering surface tissue contribution to the hemodynamic response should be an adequate method to eliminate effect of contact force between the device and the skin. However, no such rigid barrier exists around muscles, and superficial tissue filtering may not remove the effects of contact force because the tissues deform under load[51] and STT is more variable. By their nature, NIRS devices need to be coupled to the skin, and fixation techniques can result in different, or even time-varying, contact forces. If these varied contact forces cause differences in tissue structure then photons may propagate differently within the tissue composite (skin, adipose and muscle) causing a measurement artefact. Researchers are aware of the potential issues relating to contact force and they often attempt to prevent "excessive eternal pressure"[52] or provide "sufficient care … not to occlude blood flow"[53] when fixing NIRS devices to subjects; however, very little published research has aimed at quantifying or remediating this potential issue.

As discussed above, continuous wave NIRS collects useful, non-invasive, *in vivo,* local tissue data (relative O_2Hb, HHb, and tHb concentration changes). These

data are beneficial to physiologic investigations; however, NIRS devices suffer from limitations that need to be overcome before clinical uptake is increased.

1.3 RESEARCH OBJECTIVES

My long-term research goal is to minimize measurement artefacts in NIRS devices to refine clinical indices and encourage clinical uptake. The objective of my current work was to investigate measurement artefact related to contact force. All NIRS devices need to be coupled to skin[54] in some fashion and one of the most basic questions is, “How firmly should a NIRS device be attached to the skin?”

Surprisingly, there is little guidance in published literature, possibly because the majority of NIRS investigations focus on cerebral measurements or researchers are willing to accept contact force artefact as a limitation of the methods. With little guidance from published literature, I decided to investigate this issue in a series of studies with the goal of quantifying the effects of contact force on NIRS measurements. In theory, understanding contact force artefact should inform both NIRS data analysis and NIRS device design to increase reliability. The studies included two experimental approaches and one computer simulation.

1.3.1 STATIC CONTACT FORCE ARTEFACT

As a starting point for my research, I conducted an experiment to quantify the effects of contact force on NIRS muscle measurements. With minimal published research available to reference, I assumed that the structural properties (for example,

structural stiffness, which influences the mechanical deformation under load) would influence contact force effects; therefore, I decided to measure from several muscles, each with varied muscle activation. The geometry and supporting structure of each muscle was different, so the structural stiffness differs as well. Also, when muscle generates more force, intramuscular pressure increases[55] and stiffness increases. Both muscle location and muscle contractile intensity were varied with contact force to determine main effects and interactions, and this investigation provided some baseline data that informed the following studies.

1.3.2 OSCILLATING CONTACT FORCE ARTEFACT

Based on the findings of the static contact force investigation, I decided to explore the time-dependent behaviour of contact force on NIRS muscle measurements. Human tissues exhibit a viscoelastic response to loading[56], so the structural response is expected to change with duration of loading; therefore, the static investigation results were only applicable to isometric exercises, and additional data was needed to apply these findings to dynamic contractions where contact forces fluctuate as a result of geometrical changes. The oscillating contact force investigation was intended to address how contact force effects are altered by magnitude and frequency of external loads.

1.3.3 PHOTON PROPAGATION IN A TISSUE COMPOSITE

The final investigation of my thesis was originally planned as a tool to be used in future NIRS device design. In the work discussed in this dissertation, however, the simulation was used to examine the effects of adipose tissue compression to help

infer the underlying mechanisms responsible for contact force artefact when measuring from skeletal muscle. A computer simulation of photon propagation through a tissue composite of skin, adipose and muscle tissue was created and input variables were varied to examine the effect of STT and SDS on photon propagation.

CHAPTER 2: STATIC CONTACT FORCE ARTEFACT

Disclaimer: The content of this chapter has been submitted to a peer-reviewed journal and copywrite for the manuscript will agree with the journal's policy. The roles of each contributing author are listed in Table 1.

Table 1: The roles of each author for the static contact force investigation.

Author	Role
Timothy Schwab	• Design and construction of loading rigs • Data collection • Analyze data • Write paper
Colton Jensen	• Data collection
Dr. Alex Aravind	• Act in a supervisory role including, but not limited to, the following aspects of the investigation: experimental design, data analysis, and manuscript review.
Dr. R Luke Harris	• Act in a supervisory role including, but not limited to, the following aspects of the investigation: experimental design, data analysis, and manuscript review.

2.1 ABSTRACT

Near infrared spectroscopy is used to measure oxygenated hemoglobin and deoxygenated hemoglobin in muscle. An emitter and a detector (sometimes more than one of each) are placed in contact with the skin for such measurements. Computed hemoglobin concentrations are influenced by the magnitude of contact force (i.e. of the device against the soft tissue) but these effects are not well quantified. Therefore, with 12 healthy, adult participants, we quantified these effects by varying contact force (2, 20, 40 and 60 N), muscle contraction intensity (0, 10, 30, 50, and 70% maximum voluntary contraction) and muscle location (biceps brachii, extensor digitorum, vastus lateralis, and sternocleidomastoid). All three main effects (i.e. contact force, contraction intensity and location) were statistically significant, though no interactions were detected. In general, post hoc comparisons indicated that the lowest contact force was significantly different from all other contact forces and the remaining contact forces were not different from each other. We regressed our data to determine corrective values to minimise the effects of contact force. The relative influence of contact force is greater at lower contraction intensities. These findings can be applied to future diffuse reflectance spectroscopy investigations of both static and dynamic muscle contractions.

2.2 INTRODUCTION

In vivo concentrations of oxygenated hemoglobin (O_2Hb) and deoxygenated hemoglobin (HHb) can be measured using near infrared diffuse reflectance

spectroscopy, which is commonly simplified as near infrared spectroscopy (NIRS). NIRS devices consist of one or more light sources and one or more detectors, and rely on the diffuse reflectance of tissue to redirect emitted photons back toward the detector. The intensity (and in some cases, phase shift or timing) of reflected light is then related to hemoglobin concentrations with a modified Beer-Lambert law[57].

Using NIRS to measure hemoglobin concentration in muscle is challenging, in part because the device needs to be properly fixed to a specific location in contact with the skin overlying the target muscle. This is typically done with a strap or with tape to limit the migration of the device and to prevent decoupling of the instrument from the skin, which would result in ambient light leakage. Unfortunately, these techniques can lead to varied contact forces when muscles undergo dimensional changes during contraction. Researchers sometimes acknowledge that contact force variations have the potential to influence NIRS measurements, but the effects have yet to be quantified and, as such, have been largely ignored during acquisition. At most, researchers prevent “excessive external pressure”[52] or provide “sufficient care … not to occlude blood flow”[53] when coupling NIRS devices to the skin. In fact, only a few studies[58-64] have investigated the effects of contact force on diffuse reflectance of tissue *in vivo*.

2.2.1 PREVIOUS RESEARCH RELATING TO CONTACT FORCE

Most published research relating contact force and diffuse reflectance has been performed with isolated tissues, rather than composite structures. The literature reviewed here focused on separate investigations of muscle[58,59], adipose tissue[60]

(represented by measurements on breast tissue) and skin[61-63,65,66], because photons propagate through each of these tissues when measuring hemoglobin/myoglobin content of muscle. In these studies, there is no consistency in wavelengths, source-detector separation or measured variables, so some degree of inconsistency in results was expected. Reif *et al*[59] observed increases in oxygen saturation and reduced scattering coefficient with increased contact force (between 40 kPa and 200 kPa) on mouse thigh muscle with superficial tissues resected. Ti and Lin[58] demonstrated decreased oxygenation and total hemoglobin (tHb) only at high contact pressures (48 kPa) in rat heart following a sternotomy. Similar trends occur in compressed breast tissue, where decreases in tHb, oxygen saturation and reduced scattering coefficient were observed in response to increased contact force[60]. When skin is subjected to increased contact force (between 9 and 152 kPa), tHb and oxygen saturation both decrease[61,63]. In skin, the change in reduced scattering coefficient in response to increased contact force is less consistent: some authors demonstrate increases[63,65] but others demonstrate decreases[61,66]. These inconsistencies may result from wavelength dependent inter-subject variations[62] or from differences in methodology.

The previous studies provide valuable insight into the diffuse reflectance of tissues under varied loading, but they do not address how a composite structure of different tissue reacts to varied contact force. In a series of papers, Cugmas and coworkers[64,67,68] used diffuse reflectance spectroscopy to differentiate between different soft tissues *in vivo*. When measuring skin superficial to pollicis brevis, they observed an increased absorption coefficient, a decreased reduced scattering coefficient and decreased oxygen saturation in response to increased contact force.

Based on site specific results, they speculated that higher contact force may result in partial measurement of deeper tissues (for example, bones in the wrist) rather than from more superficial soft tissue[64]. However, practically speaking, their findings are difficult to apply to physiological NIRS measurements from muscle because they applied very high contact pressures that would be uncomfortable during muscle activation studies, and they used longer wavelengths than those typically employed when measuring hemoglobin.

Cheng *et al*[69] demonstrated that NIRS measurements from composite structures are affected by contact force. Specifically, they varied contact force between 0 N and 20 N (contact pressure not reported) on calf, thigh and breast tissue. Each tissue exhibited a decrease in tHb in response to external loading and site-specific differences in magnitude were reported; however, their results are limited to one low load (20 N), that is difficult to translate to different NIRS devices because the contact area, and, therefore, contact pressure, was not reported.

The previous studies failed to quantify the effects of varied levels of contact force and muscle activation on the hemoglobin content of human muscle tissue *in vivo*. Such data would be relevant to any study where diffuse reflectance is employed to study muscle during static or dynamic contractions.

2.3 PURPOSE

Our primary goal was to quantify the effects of contact force on NIRS measurements *in vivo* by varying contact force and muscle activation at various

muscle measurement sites. The results will be used to achieve our long-term goal of limiting the variability in NIRS data resulting from contact pressure when measuring from muscle tissue.

2.4 METHODS

2.4.1 EXPERIMENTAL DESIGN

Institutional Research Ethics Board approved all procedures in this study and 12 volunteers provided consent before taking part. NIRS data was recorded using an OxiTor M2 (portable continuous wave device with a source-detector separation of 35 mm; Pathonix Innovation Inc., Vancouver, BC, Canada). We recorded NIRS data from each participant during isometric contractions of biceps brachii (BB), extensor digitorum (ED; i.e. of the forearm), vastus lateralis (VL), and sternocleidomastoid (SCM). At the beginning of each measurement session, the participant's skinfold thickness was measured. The participant then performed three × three-second isometric contractions at maximum effort to determine the maximum voluntary contraction (MVC). The highest recorded torque (see section 2.2) in these three trials was defined as the MVC and all subsequent contractions were normalized to this level. Participants were then asked to perform a series of submaximal contractions in a randomized order. Each submaximal contraction was 0.5 minutes long and the minimum rest period between contractions was 4.5 minutes, though most rest periods were approximately 5 minutes.

Both muscle contraction intensity and NIRS contact force were varied for these submaximal contractions. Muscle contraction intensity was defined as a percent of MVC (%MVC): 0, 10, 30, 50, and 70% of MVC. The contact force levels for BB, ED, and VL were 2, 20, 40 and 60 N. The 60 N contact force level could not be maintained comfortably on SCM so 2, 20, 30, and 40 N contact forces were used instead. For reference, the contact area between the OxiTor and the skin is 24.4 cm^2, so the contact forces 2, 20, 30, 40, and 60 N correspond, respectively, to contact pressures of approximately 0.82, 8.2, 12, 16 and 25 kPa. The lowest contact force (2 N) was selected because we determined that this was the minimal contact force level that could be used without device-skin decoupling occurring during contraction.

2.4.2 LOADING APPARATUS

We constructed custom rigs to measure joint torques and contact forces during isometric contraction. Joint torques were measured with a ±1130 Nm torque cell (TFF600, Futek, Irvine, CA, USA). The torque cell was aligned with the axis of rotation for the BB (elbow) and the VL (knee). For ED and SCM contractions, force applied was perpendicular to the moment arm of the torque cell. Participants maintained a specified %MVC with the aid of a visual display.

Contact forces were recorded with a uniaxial load cell attached to a custom clamp. The load cell (±220 N, LSB200, Futek, Irvine, CA, USA) was aligned with geometric center of the OxiTor and held in place with set screws. Contact forces were applied by hand following a visual display. Both joint torque and contact force were

recorded with a computer (IPM 650 and Sensit software, Futek, Irvine, CA, USA). Sample data traces are depicted in Figure 4.

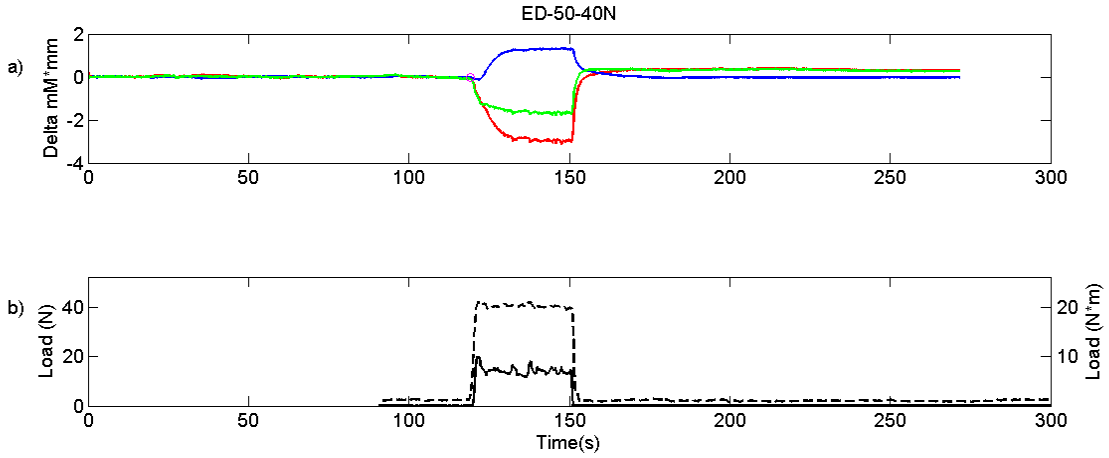

Figure 4: Sample data traces of (a) O_2Hb (red), HHb (blue) and tHb (green) in response to a contraction at 50% MVC, and (b) torque (solid black line) and contact force (dashed black line).

2.4.3 ANALYSIS

2.4.3.1 NIRS ANALYSIS

We analyzed relative peak-concentration-changes (measured in mM·mm) of O_2Hb, HHb and tHb. The baseline bias values were computed by taking the average of each data trace (O_2Hb, HHb, or tHb) in the 30 seconds prior to the beginning of each contraction. The peak-concentration-changes were defined as the largest change from baseline that was recorded during the contraction.

2.4.3.2 STATISTICS

Peak concentration changes were analyzed with a three-way repeated measures ANOVA (using R Project software, https://www.r-project.org/about.html) with factors of contraction intensity, contact force and muscle location. *Post hoc* comparisons were performed using paired t-tests with Bonferroni correction. This analysis was completed separately for each of O_2Hb, HHb and tHb.

2.4.3.3 CONTACT FORCE CORRECTIONS

We determined a corrective equation intended to help compare NIRS data recorded with higher contact forces to those recorded with minimal contact force (2 N). Peak concentration changes were biased with respect to 2 N contact force and 0%MVC for each muscle location. These zeroed-peak-concentration-changes were regressed with a multiple least-squares regression on contact force and contraction intensity to give

(2) $$\widehat{Hb} = c_F \, ln(F) + c_{MVC} \cdot \%MVC$$

Where:

$\widehat{Hb}$ is the estimate of hemoglobin (O_2Hb, HHb or tHb) zeroed-peak-concentration-change;

F is contact force in Newtons;

$\%MVC$ is the contraction intensity as a percent of maximum voluntary contraction

c_F and c_{MVC} are the regression coefficients.

All regressions were forced through the origin.

2.5 RESULTS

2.5.1 PARTICIPANT DESCRIPTIVE STATISTICS

Nine male participants and three female participants completed the study protocol. The average and standard deviation of height, weight and age were 171 cm ± 8.6 cm, 76 kg ± 15 kg, and 29 years ± 8.1 years, respectively. Adipose tissue thickness was approximated as half the skinfold thickness and was recorded for BB (3.5 mm ± 2.5 mm), ED (2 mm ± 1.5 mm), VL (6 mm ± 4.5 mm), and SCM (2 mm ± 1.5 mm).

Participants were able to maintain the submaximal target loads of 10% MVC, 30% MVC, 50% MVC and 70% MVC with one standard deviation equal to 1.2% MVC, 2.4% MVC, 4.0% MVC and 5.6% MVC for each target, respectively. Contact force was manually applied by one researcher (CJ) and was acceptably close to target loads: 2.02 N ± 0.65 N, 20.2 N ± 1.6 N, 39.6 N ± 1.9 N, 28.9 ± 1.4 N, and 59.5 N ± 2.0 N.

2.5.2 STATISTICAL FINDINGS

Peak-concentration-change results for O_2Hb, HHb, and tHb are displayed in Figure 5 and Figure 6. The main effects of contraction intensity, contact force and muscle location were all statistically significant ($p < 0.001$ for all main effects). No statistically significant interactions were detected between contact force and contraction intensity ($p = 0.66$), contact force and muscle location ($p = 0.41$), or contact force and both contraction intensity and muscle location ($p = 0.95$). Some general trends are evident in Figure 5 and Figure 6: O_2Hb and tHb both decreased and HHb increased when muscle tissues were subjected to increased contact forces. These changes persisted at all levels of contraction intensity with greater magnitudes due to the added effect of the contraction. Magnitudes also varied across muscle location ($p<0.001$), with greater changes in large muscles (BB and VL).

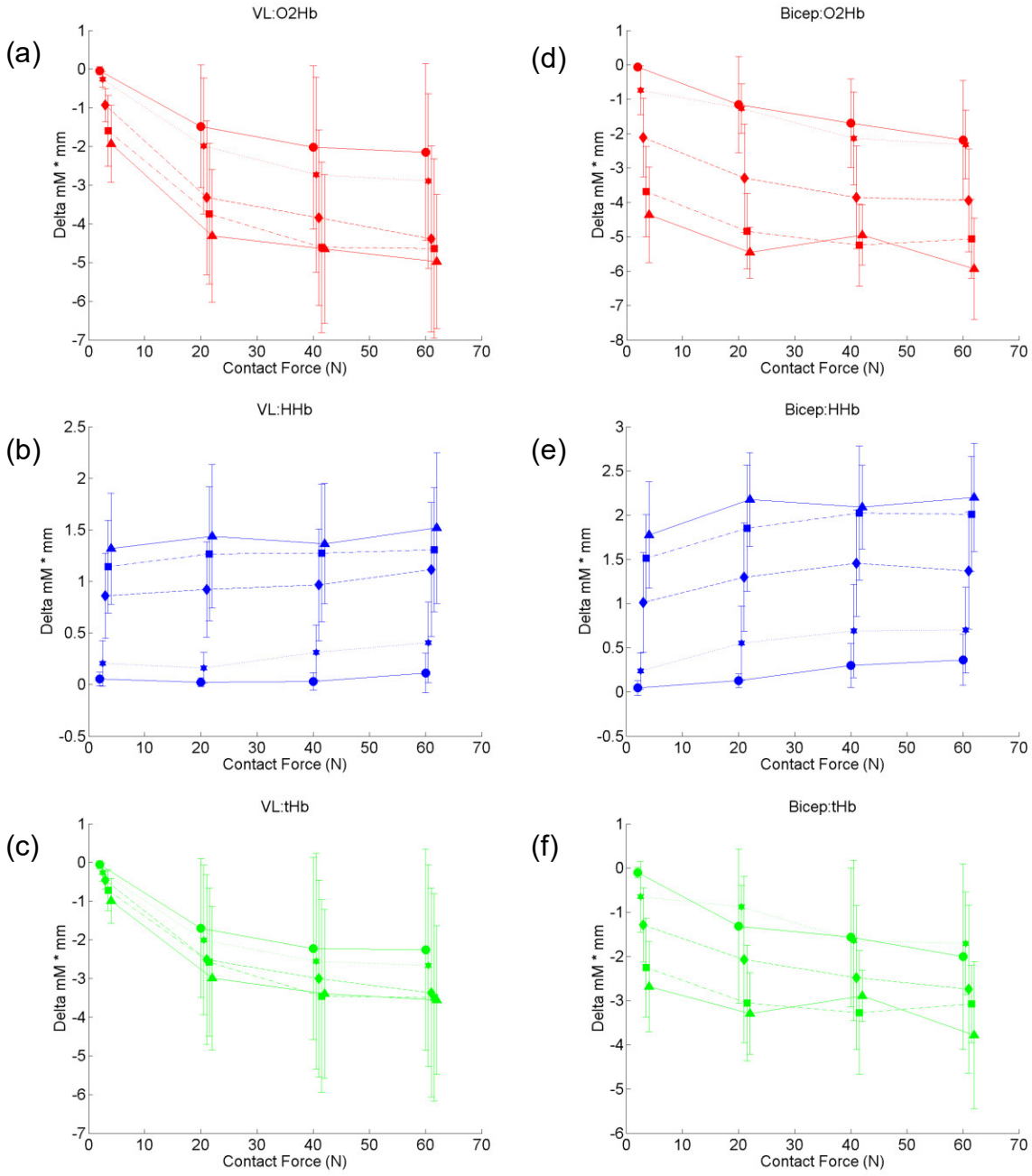

Figure 5: Peak changes for VL (a) O_2Hb, (b) HHb, (c) tHb, and for ED (d) O_2Hb, (e) HHb, (f) tHb. Each mark represents a different level of contraction (● = 0% MVC; ✸ = 10% MVC; ♦ = 30% MVC; ■ = 50% MVC; ▲ = 70% MVC). Data points for 10%, 30%, 50% and 70% MVC are offset slightly to clarify error bars (±SD).

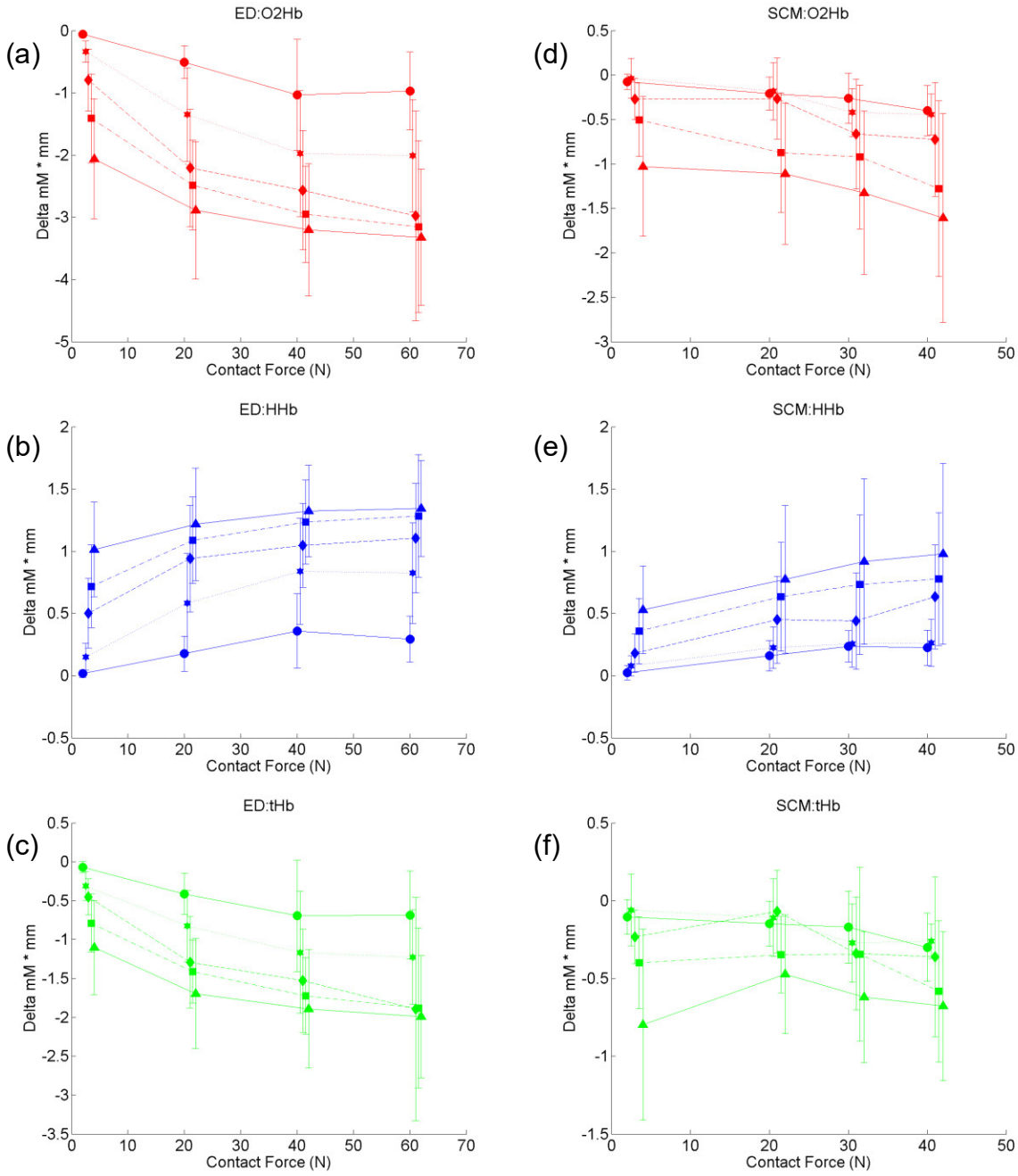

Figure 6: Peak changes for ED (a) O_2Hb, (b) HHb, (c) tHb, and for SCM (d) O_2Hb, (e) HHb, (f) tHb. Each mark represents a different level of contraction (● = 0% MVC; ✸ = 10% MVC; ♦ = 30% MVC; ■ = 50% MVC; ▲ = 70% MVC). Data points for 10%, 30%, 50% and 70% MVC are offset slightly to clarify error bars (±SD).

The effects of contact force were further investigated with *post hoc* comparisons. The contact force levels differed for SCM, so comparisons for each muscle location were computed separately. For almost all combinations of contraction intensity and muscle, statistically significant differences in peak-concentration-change were detected between 2 N contact force and all other contact force levels, except for BB-HHb, SCM-tHb and VL-HHb. When comparing contact force levels above 2 N, we observed a single statistically significant difference (tHb values between 20 N and 40 N on SCM), but all other comparisons (n=35) were not statistically significant, which suggests that, above 20 N, there is limited effect of contact force on peak-concentration-change.

2.5.3 REGRESSIONS

Zeroed-peak-concentration-changes (see Contact Force Corrections section above) were regressed on the natural logarithm of contact force (N) and contraction intensity (%MVC) with a least-squares method. Data from each muscle location was regressed separately because the levels of contact force were different for SCM—this decision was supported by a *post hoc* analysis that revealed significant differences between the coefficients at each muscle location. The regression coefficients and adjusted correlation coefficients are listed in Table 2. All of the slope coefficients were significantly different from zero, with the exception of one (SCM, tHb, ln(contact force)). All slope coefficients were negative for O_2Hb and tHb and were positive for HHb. Adjusted correlation coefficients (adjusted r^2) ranged from 0.373 (SCM, tHb) to 0.896 (BB, O_2Hb), with all r^2 values being statistically significant.

Table 2: Regression coefficients for each predicted variable (O_2Hb, HHb, and tHb) at each muscle location (BB, ED, SCM and VL). Standard errors are quoted in parentheses. Superscript symbols indicate p-values of each coefficient and the total regression equation (*** p<0.001; ** p<0.01; * p<0.05).

Muscle Location	Predicted Variable	ln(Force) c_F	Contraction Intensity c_{MVC}	Adjusted r^2
BB	O_2Hb	-0.444 (0.035)***	-0.059 (0.003)***	0.896***
BB	HHb	0.104 (0.016)***	0.026 (0.001)***	0.857***
BB	tHb	-0.359 (0.038)***	-0.031 (0.003)***	0.748***
ED	O_2Hb	-0.368 (0.026)***	-0.027 (0.002)***	0.842***
ED	HHb	0.133 (0.010)***	0.013 (0.001)***	0.865***
ED	tHb	-0.230 (0.018)***	-0.014 (0.001)***	0.789***
SCM	O_2Hb	-0.064 (0.020)**	-0.013 (0.001)***	0.542***
SCM	HHb	0.064 (0.011)***	0.008 (0.001)***	0.660***
SCM	tHb	-0.011 (0.011)	-0.006 (0.001)***	0.373***
VL	O_2Hb	-0.662 (0.052)***	-0.031 (0.004)***	0.748***
VL	HHb	0.034 (0.014)*	0.020 (0.001)***	0.770***
VL	tHb	-0.641 (0.058)***	-0.013 (0.004)**	0.595***

2.6 DISCUSSION

2.6.1 MAIN FINDINGS

The main finding from our experiment was that the magnitudes of O_2Hb, HHb and tHb values measured with continuous wave NIRS are affected by the contact force with which the NIRS device is applied to the soft tissue being studied. Specifically, increasing contact force amplifies decreases in O_2Hb and tHb such as

those that are typically associated with a contraction; increasing contact force also amplifies the corresponding increases in HHb. Importantly, these effects of contact force on the observed hemoglobin concentration changes in skeletal muscle are not further altered by the degree of muscle activation. We also determined regression equations that could correct for these contact force effects during isometric contractions.

2.6.2 APPLYING THE FINDINGS

We demonstrated that contact force influences hemoglobin values determined by NIRS. The influence of contact force appears to be limited to lower contact force levels (≤ 20 N). We detected one statistically significant difference between contact force greater than 20 N (comparing 20 N to 40 N for tHb in SCM), but this may be a type I error because it is not consistent with the other 35 pairwise comparisons we performed at force levels at or above 20 N, for which no differences in hemoglobin concentration changes were observed. This threshold pattern is similar to those documented in skin (see Lim et al's[61] Figure 4 for a subjective comparison).

Two different approaches could be used to minimize contact force effects. The simplest technique would be to ensure that instrument fixation maintains a minimum of 20 N contact force (8.2 kPa contact pressure) regardless of changes to muscle geometry or muscle engorgement due to contractile activity. This is feasible for short durations, but our experience indicates that contact forces above 20 N cause discomfort during longer sessions (greater than 20 minutes).

The second approach would be to directly measure contact force during NIRS data collection and adjust hemoglobin concentrations with the regression coefficients listed in Table 2. Our findings are preliminary and only applicable to isometric contractions, but if future investigations verify findings, then the slope coefficient for ln(Contact Force) could be used for this adjustment; however, site-specific differences suggest that this technique would be limited to one of the four muscle locations examined in the current study. Additional locations could be documented with less effort because we have shown no interaction between contact force and muscle activation, so only contact force needs to be varied.

Our regression coefficients demonstrate the potential errors caused by ignoring the effects of contact force. For example, predicted peak-concentration-changes changes in O_2Hb (in BB, see Table 2) associated with 20 N and 10% MVC are -1.33 mM·mm and -0.59 mM·mm, respectively. This suggests that the peak-concentration-change in O_2Hb reported by the device is dominated by contact force at low contraction levels. In contrast, at 70% MVC the peak-concentration-change in O_2Hb resulting from contraction intensity is estimated as -4.13 mM·mm, so contact force has a smaller relative effect at higher muscle contraction intensities. In other words, approximately 69% of the hemoglobin changes are a contact force artefact when measuring from muscle during low contractile intensities. When measuring from muscle during higher contractile intensities, the contact force artefact accounts for 25% of the measured hemoglobin changes. Similar trends exist at all muscle locations and all outcomes (O_2Hb, HHb, and tHb).

We believe that, after further verification, mathematically correcting NIRS-derived hemoglobin concentrations is the best approach, especially when performing studies with low levels of muscle activation or when participants will be studied for prolonged periods.

2.6.3 SYNTHESIS WITH PUBLISHED LITERATURE

No previous study has investigated the relationship between different levels of contact force and *in vivo* NIRS muscle hemoglobin data, though previous studies provide insight into the possible mechanisms for our findings.

Previous NIRS research suggests that increased contact force compresses soft tissue by redistributing fluid (both water and blood) away from the interrogated volume. Fluid redistribution is a suggested mechanism for findings in isolated muscle tissue[58,59] and multi-layered *in vivo* structures[68,69]. The effects of tissue compression vary with tissue and absorber type. In isolated muscle, reduced scattering coefficient is increased, presumably because scattering components become closer together when fluid is forced from the tissue[59]. When blood within muscle is redistributed away from the interrogated volume, decreases in tHb are observed[58]. Consistent with this, tHb decreased as contact force increased in our experiment, which suggests that some of the observed changes may be the result of blood redistribution.

Determining where the fluid redistribution occurs is difficult. We tested a multi-layered tissue composite composed of skin, adipose tissue and muscle. The phenomenon of decreased tHb and increased scattering has been observed in skin[61,63], adipose tissue[60] and muscle[58,59], so it is unknown what tissue layer, if any, is

the dominant source of fluid redistribution. Cugmas et al[64,67,68] have quantified tissue specific responses to pressure, but they reported that their results were "frequently inconsistent"[68] under 16 kPa (40 N in our study), and they used different light wavelengths with much shorter source-detector separations from those in our study, so little guidance can be derived from their work to explain our findings. Cheng *et al*[69] suggest that viscoelastic creep of tissues while under load may result in signal contamination from bone below the measurement site, and result in gradual increases in tHb during loading. We did not observe similar tHb recovery during loading and we speculate that Cheng *et al.*'s contact pressure was less than ours and resulted in less complete occlusion of the microvasculature.

A finite element model[70] indicates that increased muscle activation decreases muscle deformation during mechanical indentation, though skin deformation is unaffected by muscle activation. Adipose tissue deformation during indentation is governed by its thickness, rather than muscle activation. We did not observe an interaction between contact force and activation, so we speculate that fluid redistribution in the skin or subcutaneous adipose tissue might be the source of the contact force effects, but further experimentation is required to confirm this.

2.6.4 CURRENT LIMITATIONS AND FUTURE DIRECTIONS

Our study was not designed to determine the mechanisms responsible for contact force effects, though future research will be geared toward determining these mechanisms. If contact force effects are driven by fluid redistribution in superficial tissues, then these effects could be filtered from the signal using short source-detector

separation optodes. Until this is verified or disproven, we suggest that NIRS data be adjusted as discussed in the previous section to minimize data variability.

As with most NIRS studies, our variability was high. We may be able to explain more variation by adding more factors to our regression (for example, adipose tissue thickness); however, the intention of the regression was to quantify the NIRS changes associated with increasing contact force rather than identifying all sources of variation. We included muscle activation because that was a controlled factor in our experiment. We forced our regressions though the origin because non-zero intercepts would be illogical when computing corrective values for contact force.

We performed this experiment with a continuous wave NIRS device that was unable to record absolute values of O_2Hb, HHb, tHb or tissue oxygenation index. Instead our data reports the changes relative to baseline prior to each contraction (30 second average), so there is a potential confounding effect of reactive hyperemia influencing the baseline of the next contraction. We allowed at least 4.5 minutes of rest between contractions to minimize this risk and did not observe baseline drift.

We conducted our experiment with an OxiTor M2, so caution should be used when applying our results to other NIRS devices because alternate form factors may influence the changes induced by varied contact force. In particular, the emitters and detectors protrude from the body of the OxiTor. These protrusions may act as stress risers resulting in higher contact pressures around the protrusions. Despite these potential inhomogeneities in contact force, we suspect that similar results would be

obtained with other NIRS devices, assuming their contact surface is similar to the OxiTor (rectangle; 65 mm x 37.5 mm).

2.6.5 CONCLUSION

We demonstrate that contact force affects hemoglobin concentrations determined by NIRS and we suggest possible techniques to minimize these variations. Our experiment was conducted with isometric contractions, so our findings are applicable to static analysis. However, our findings also may provide insight into dynamic contractions because we failed to detect an interaction between contraction intensity and contact force.

2.6.6 ACKNOWLEDGMENTS

We would like to acknowledge the financial support of a NSERC Engage Grant awarded by the Natural Sciences and Engineering Research Council of Canada to AA and TS in collaboration with Pathonix Innovation Inc., Vancouver, BC, Canada.

We would also like to acknowledge the assistance of Dr. Shadgan and Dr. Molavi at Pathonix Innovation Inc. for their input on experimental design and analysis. Also, we would like to thank Shamitha Aravind for her contributions during data acquisition.

CHAPTER 3: OSCILLATING CONTACT FORCE ARTEFACT

Disclaimer: The content of this chapter will be submitted to a peer-reviewed journal for publication and copywrite for the manuscript will agree with the journal's policy. The roles of each contributing author are listed in Table 3.

Table 3: The roles of each author for the oscillating contact force investigation.

Author	Role
Timothy Schwab	• Data collection • Data analysis • Interpret findings • Write paper
Shamitha Aravind	• Data collection • Data analysis
Dr. Alex Aravind	• Act in a supervisory role including, but not limited to, the following aspects of the investigation: experimental design, data analysis, and manuscript review.
Dr. R Luke Harris	• Act in a supervisory role including, but not limited to, the following aspects of the investigation: experimental design, data analysis, and manuscript review.

3.1 ABSTRACT

Near infrared spectroscopy (NIRS) measurements of hemoglobin (Hb) concentration in skeletal muscle tissue are influenced by contact force between the NIRS device and soft tissue. Measurements taken during *in vivo* dynamic exercise may be subject to contact forces that vary over time, and these time-dependent effects on hemoglobin measurements have not been quantified. The purpose of this study was to evaluate how different magnitudes and periods of cyclic square-wave loading affects relative hemoglobin concentrations. Higher contact loads were associated with greater peak changes, reoxygenation rates, cyclic amplitudes and cyclic averages. Longer cyclic periods resulted in larger cyclic amplitudes and cyclic averages, and these magnitudes changed over the duration of loading. Greater superficial tissue thickness was associated with trends similar to those observed with increased contact loads. These effects need to be considered when interpreting NIRS data, in order to differentiate between real physiologic changes and measurement artefacts.

3.2 INTRODUCTION

Near infrared spectroscopy (NIRS) is a technique in which two or more wavelengths of light are emitted into human tissue. Emitted photons undergo diffuse reflectance within the tissue and a portion of re-emitted photons is detected by the NIRS device. Oxygenated hemoglobin (O_2Hb) and deoxygenated hemoglobin (HHb) have different absorption spectra, enabling relative concentrations of O_2Hb and HHb

to be computed using a modified Beer-Lambert law[26]. Total hemoglobin (tHb) concentration is then computed as the summation of O_2Hb and HHb concentrations.

NIRS measurements and subsequent computations rely on proper coupling between the NIRS device and skin. If a device de-couples from the skin, ambient light leakage contaminates the data[54]. The inverse is also true: elevated contact force can also influence data quality. This contact force artefact is complicated by the layering of interrogated tissues. *In vivo* measurements of muscle metabolic activity are made when photons propagate through skin, subcutaneous adipose and muscle tissues, so NIRS contact force effects need to be characterized for the complete skin-adipose-muscle composite. All three layers interact to produce a specific mechanical response to external loading. For example, the tissue composite's overall viscoelasticity and compressive strain is influenced by the material properties of each constituent layer[51,71]. This combined tissue response to compression can influence NIRS data.

One method to evaluate the *in vivo* tissue optical response is to study each constituent layer independently and create a theoretical model to combine the results. At the present time, the relevant layers have not all been thoroughly examined independently to provide the detail required for this, though previous investigations explored optical effects when isolated tissues are subjected to compression[58,59,66].

Both rat heart[58] and mouse skeletal muscle[59] experienced a decrease in tHb when contact force was increased. Both studies also demonstrated increased HHb and deceased tissue oxygenation index (TOI) when higher contact forces were

applied. Time-dependent effects were not reported for skeletal muscle[59] and they were difficult to quantify in heart because of heart movement throughout the cardiac cycle.

Time dependent effects in the optical behaviour of skin were demonstrated by Chen *et al*[72]. The authors determined that the optimal contact pressure to measure blood glucose from skin is 66 kPa. At this pressure, signal variability was decreased and little additional signal optimization resulted from higher contact pressures. At 66 kPa, NIRS data took approximately 30 seconds to stabilize, which we interpret as a viscoelastic response of the skin. A different study[61] demonstrated a clear decrease in skin TOI over 60 seconds of elevated contact pressure. This effect was site-specific, with TOI stabilizing after 20 seconds when measured from the forehead. Stabilization was less evident on the finger and neck (see their Figure 4 for details).

Instead of building a theoretical model, based on constituent layers, it is more feasible to directly measure the optical response of tissue composites *in vivo*. Previous work[73] demonstrated time-dependent response of breast tissue (skin-adipose composite) in response to cyclic contact force. tHb was also observed to decrease in association with increased contact force. The SDS used for the study ranged from 1.5 to 2.6 cm, so diffuse reflectance occurred in both skin and adipose tissue.

Cugmas *et al*[68] measured *in vivo* NIRS response to contact force with the intent of tissue classification. One of their measurements sites was over the abductor pollicis brevis muscle, so it consisted of a skin-adipose-muscle composite; however, their SDS was geared toward measurements from skin, rather than underlying muscle.

Increased contact force caused increased absorption and decreased reflectance and reduced the cutaneous scattering coefficient.

Previously, we investigated the effects of static contact force on NIRS muscle measurements (unpublished data). Various static contact forces combined with various isometric muscle activations were tested at four different locations, including from the vastus lateralis muscle (VL). Peak changes in tHb, O_2Hb and HHb were affected when contact force increased. Both tHb and O_2Hb decreased and HHb increased. While both contact force and muscle activation significantly affected peak changes, no interaction was detected, which suggested that follow up studies should not need to vary muscle activation. However, these findings only apply to isometric contractions with static loading (unpublished results). Given that fixation techniques usually involve straps, dynamic motions are expected to affect contact force as muscle geometry changes. Dynamic loading is usually cyclic (for example, recording from VL during cycling), so time dependent effects are also important. The current study addresses these issues by measuring NIRS response to cyclic loading at different periods.

3.3 PURPOSE

The objective of this study was to quantify the relationship between computed changes in O_2Hb, HHb and tHb concentrations in response to varied contact force, period of loading and cycle number. Contact force, period and cycle number were

expected to influence the behaviour of computed O_2Hb, HHb and tHb for all outcome measurements.

3.4 METHODS

3.4.1 PROTOCOL

Eighteen volunteers, ten males and eight females, participated in the study after providing informed consent. All procedures were reviewed and approved by the institutional research ethics board. NIRS data was acquired from the thigh by placing a NIRS device (OxiTor M2, Pathonix Innovation Inc., Vancouver, BC, Canada) superficial to the midline of vastus lateralis. Longitudinal placement was determined by landmarking both the greater trochanter and the distal end of vastus lateralis. The NIRS device was placed 60% of the distance between the two landmarks (referenced from the greater trochanter), using the greater trochanter as a reference. Skinfold thicknesses were recorded three times at the NIRS measurement location and the average of these three measurements multiplied by 0.5 was used to estimate superficial tissue thickness (STT, consisting of skin and subcutaneous adipose tissue).

Participants sat in a chair with their hip and knee each at 90 degrees of flexion and they were asked to refrain from activating vastus lateralis and other leg muscles throughout the experiment. Varied levels of contact force were applied to the NIRS device with the aid of a custom loading cradle (Figure 7) and load cell (±220 N,

LSB200, Futek, Irvine, CA, USA). One investigator (TS) applied the contact force with one hand while bracing the participant's knee to prevent motion and muscle activation.

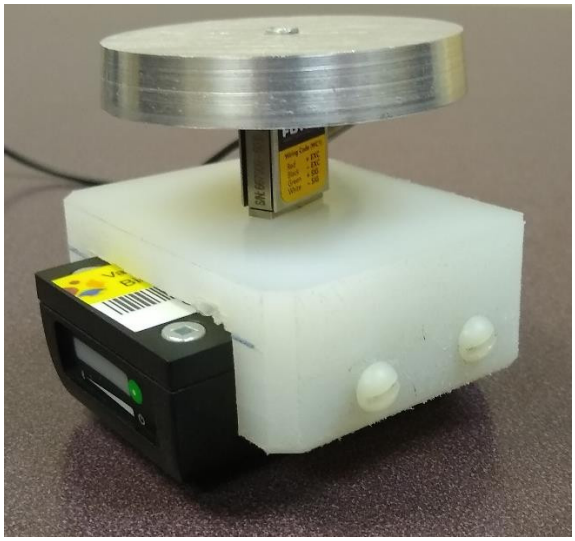

Figure 7: Custom loading cradle and load cell.

The loading protocol consisted of 13 trials, each with 2 minutes of baseline measurement, 2 minutes of contact force loading and 2 minutes of recovery. The entire protocol took approximately 1.5 hours and was conducted in a mostly darkened room to minimize the potential for ambient light contamination. During the contact force loading, both the level of contact force and the cyclic period were varied randomly. Peak load levels were 15 N, 30 N and 60 N. Cyclic loading consisted of square waves starting at 1 N and stepping up to the peak load with periods of 5 s, 10 s, 20 s and 240 s. Loading with a period of 240 s approximated the static load condition.

3.4.2 ANALYSIS

Relative concentration changes in O_2Hb, HHb and tHb, measured in mM*mm, were computed with respect to the average values recorded in the 2-minute baseline measurement immediately preceding each loading trial. Five outcome measurements were computed from O_2Hb, HHb and tHb data. TOI values were not analyzed because they were not fully implemented in our NIRS device. Outcomes quantified both the overall response (i.e., PC and FR) for each trial and the cyclic response (i.e., CAM, CAV, and CR; these five abbreviations are explained below). For each trial, the peak change (PC) is the largest magnitude change from baseline during the entire loading period; and final reoxygenation rate (FR) is the least-squares regression slope of the O_2Hb curve for 3 s at the end of loading[74]. Cycle-specific outcomes include the following. (i) Cyclic average (CAV) is the average relative hemoglobin concentration change during one complete cycle, which is synonymous with DC offset for each cycle. (ii) Cyclic amplitude (CAM) is the difference between the maximum and minimum hemoglobin concentrations during one full loading cycle. (iii) Cyclic reoxygenation rate (CR) is the same as FR, but computed at the beginning of the unloaded portion of each loading cycle. A 3-second window was not possible for CR because the shortest period was 5 seconds, so a 1-second interval was chosen instead. All cyclic measurements—CAV, CAM and CR—were computed for each loading cycle. Both PC and FR were computed to provide an indication of the aggregate response to each loading block. CAV, CAM and CR were computed to quantify the time-dependent nature of contact force artefact. A schematic description of the outcome measurements is displayed in Figure 8.

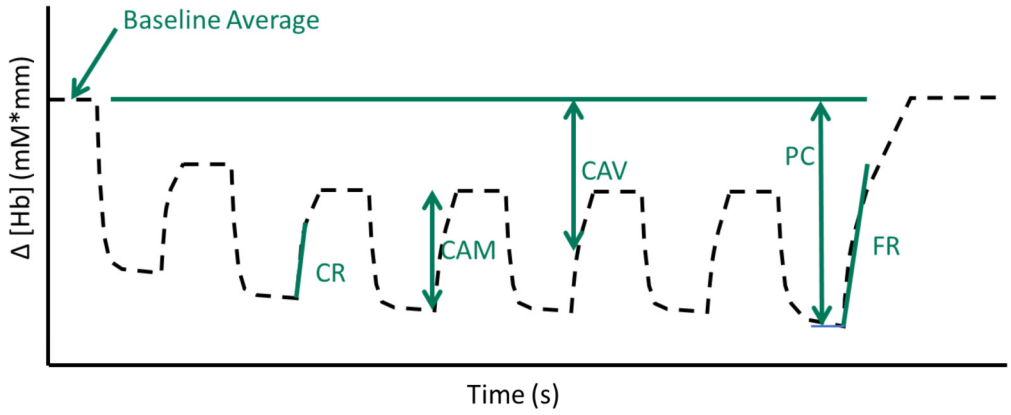

Figure 8: Schematic representation of PC, CAV, CAM, CR and FR for one trial (20 sec period and 60 N load)

3.4.3 STATISTICS

Peak data were analyzed with a three factor ANOVA, with load, period and STT as within-subject factors. Cyclic data contained different numbers of data points because different loading periods resulted in different numbers of loading cycles; therefore, a mixed-effects model was used to analyze cyclic data. Load, period, cycle and STT were fixed effects, subject was a random effect, and model residuals were checked to ensure statistical models were appropriate.

Post hoc comparisons were made with t-tests and p-values were adjusted for multiple comparisons using the Holm-Bonferroni method. All levels within each factor were compared in the post hoc tests for the ANOVA results, and an equivalent approach was used with the post hoc tests for load and period cyclic data (mixed model results). Post hoc tests based on cycle number were restricted to comparisons between the first cycle vs. each remaining cycle. This approach was taken to avoid an

excess number of post hoc test and qualitative analysis of the results suggested that cyclic effects where largely restricted to the first cycle.

3.5 RESULTS

A total of 18 subject participated in the study and their descriptive statistics are listed in Table 4. Fifteen out of 18 participants responded to contact force, both static and cyclic, in a similar pattern. O_2Hb, HHb and tHb decreased from baseline during loading and values returned to baseline following the removal of the load. This typical response is presented in Figure 9 a). The recovery was more variable, with some subject exhibited a hyperemic response, and some simply returned to baseline values asymptotically. The response to loading in three subjects did not follow these typical patterns. In these three subjects, O_2Hb and tHb decreased and HHb increased (Figure 9, b and d), in a similar fashion to what would be expected during a contraction. These three subjects were included in the statistical analysis and their presence did not alter significance levels in a meaningful manner.

Table 4:Descriptive statistics of subjects.

	Mean	Standard Deviation
Age (years)	29.4	9.9
Height (m)	1.74	0.07
Weight (kg)	76.3	19.7
BMI	24.9	4.45

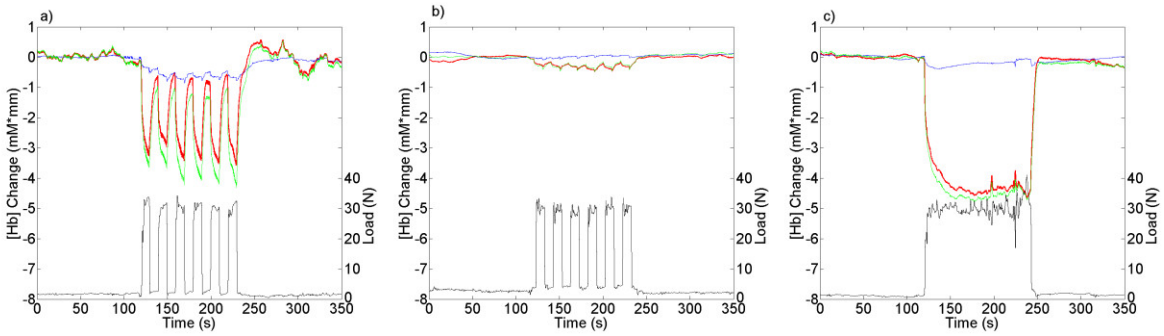

Figure 9: Example trial data. Each chart displays hemoglobin changes, with O_2Hb in red, HHb in blue and tHb in green. The corresponding square wave loading is drawn in black and plotted against the secondary y-axis. a) is representative of the typical NIRS response to external load (15 out of 18 subjects). b) is representative of the atypical NIRS pattern, which is similar to a muscular contraction where HHb increases over time, though the magnitude is much smaller than that expected with a contraction. c) is representative of a static hold.

Load period and cycle effects were largely consistent on all outcome measures for O_2Hb, tHb and HHb. Some general trends included the following. (i) Increased contact force resulted in a greater magnitude of PC, CAV, CAM, CR and FR. (ii) A longer period caused a greater magnitude of CAV and CAM. (iii) The effects of cycle were mostly limited to the first one or two loadings cycles. These cycles had smaller magnitudes of CAV and larger magnitudes of CAM when compared to the remaining cycles. (iv) Subjects with greater STT typically exhibited larger magnitudes of PC, CAV, CAM, CR and FR. There were some exceptions to the above general trends. As previously mentioned, HHb exhibited a more variable response than O_2Hb and tHb because HHb sometimes decreased and sometimes increased in response to each elevated load, so main effects were not always statistically significantly. In contrast,

O_2Hb and tHb both decreased in response to treatments so there we detected statistically significant changes. The following paragraphs provide detailed results, grouped by outcome measurement.

3.5.1 PEAK CHANGES

PC was affected by contact force and STT. All levels of contact force were different from each other for both O_2Hb and tHb ($p<0.0001$ for both). No effect of contact force on HHb was detected. Similarly, a significant main effect of STT on PC was detected for O_2Hb and tHb ($p<0.0001$ for both), but not HHb. No post hoc t-tests were performed for STT levels because some subjects had equivalent STTs (see Figure 10 description for more details) and there were many levels of STT. No effect of period on PC was detected for O_2Hb, tHb or HHb.

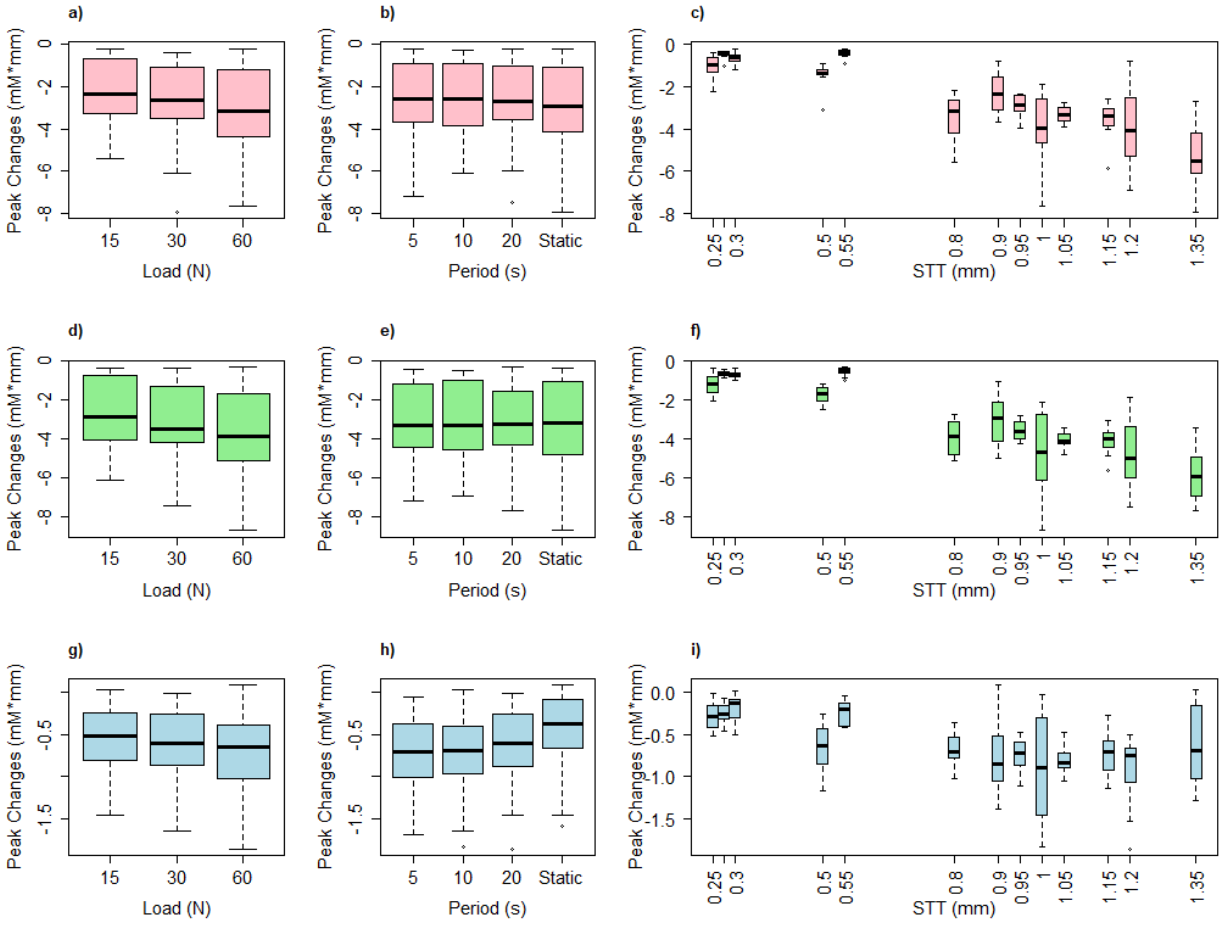

Figure 10: Boxplots depicting the effects of contact force, period and STT on peak changes (PC). O_2Hb data is displayed in a, b and c, tHb data is displayed in d, e and f and HHb data is depicted in g, h and i. Only 13 boxes are shown in c, f and i because each of the following STTs had two subjects with equivalent values: 0.3, 0.9, 1.0, 1.2 and 1.35 mm.

3.5.2 FINAL REOXYGENATION RATE

FR was affected by contact force ($p=0.003$), period ($p=0.037$) and STT ($p<0.001$). Post hoc comparisons revealed differences between 15 N and 60 N ($p=0.003$) and 30 N and 60 N ($p=0.039$). FR following static loading was significantly different than periods of 5 s ($p<0.001$), 10 s ($p<0.001$) and 20 s ($p<0.001$), and we

failed to detect differences in FR for all cyclic periods. Similar to the PC analysis, no post hoc comparisons were made for FR as a function of STT (see Figure 11).

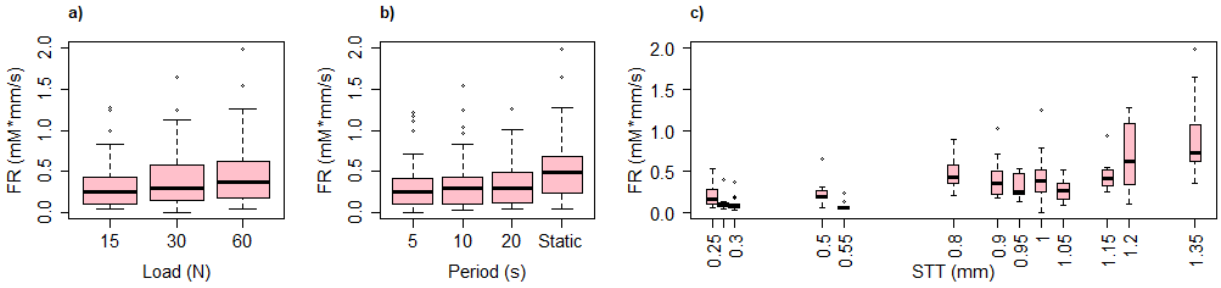

Figure 11: Boxplots of final reoxygenation rate (FR) as a function of (a) contact force, (b) period and (c) STT.

3.5.3 CYCLIC AVERAGE

Contact force affected CAV for O_2Hb, tHb and HHb and all levels of contact force were different from each other ($p<0.0001$). There was also a significant main effect of period on CAV and post hoc comparisons revealed differences between 5-s and 10-s periods in their effects on CAV for both O_2Hb ($p=0.0001$) and tHb ($p=0.0003$). There was also a significant difference between the 10-s and 20-s period effects on HHb ($p<0.0001$, see Figure 12). Cycle number affected CAV for O_2Hb ($p<0.0001$), tHb ($p<0.0001$) and HHb ($p<0.0001$), and post hoc results demonstrated that the first cycle was significantly different from the remaining cycles. STT also affected CAV for O_2Hb ($p<0.0001$) and tHb ($p<0.0001$), but there was no significant effect of STT on CAV for HHb ($p=0.078$). See Figure 13 for a summary of STT results.

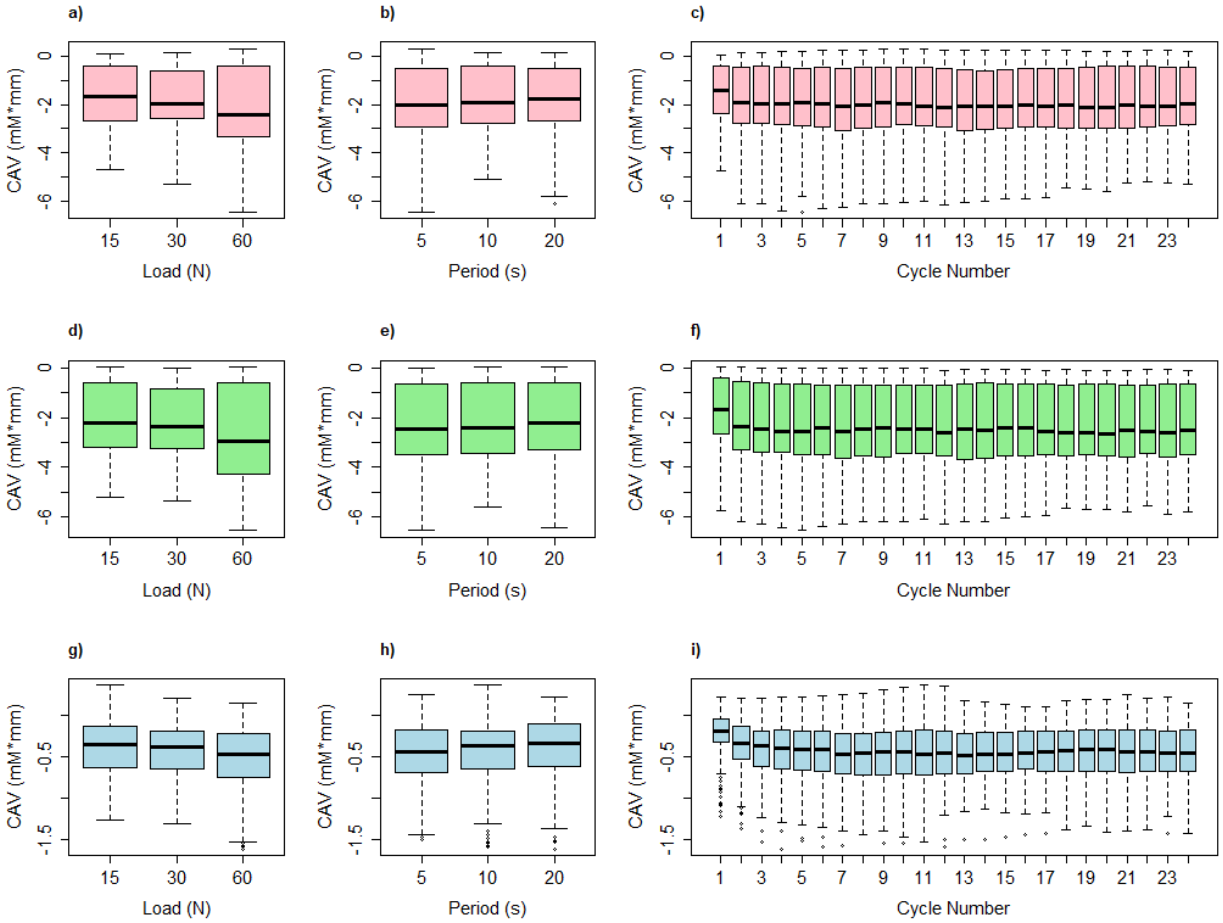

Figure 12: Box plots of cyclic average (CAV) data for O_2Hb (a, b and c), tHb (d, e and f), and HHb (g, h and i).

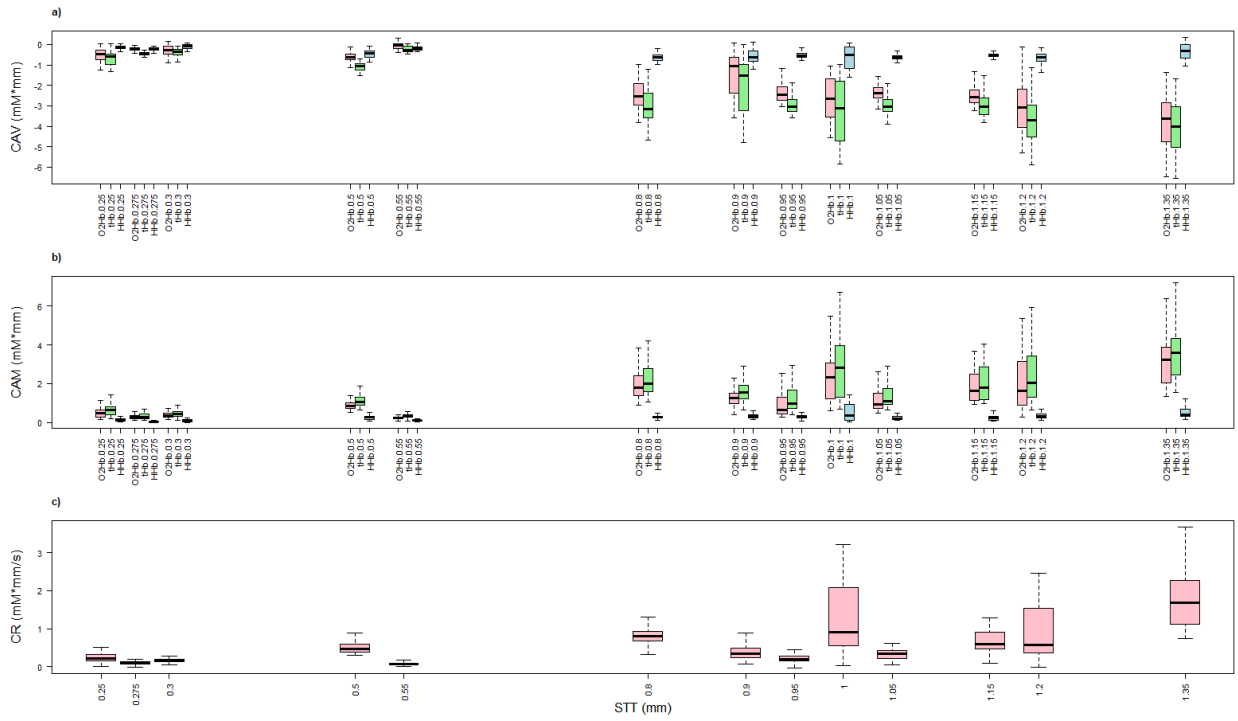

Figure 13: Boxplots depicting the effects of superficial tissue thickness, STT, on (a) CAV, (b) CAM and (c) CR. O_2Hb, HHb and tHb are shown in red, blue and green, respectively.

3.5.4 CYCLIC AMPLITUDE

CAM increased in response to increased load for O_2Hb, tHb and HHb ($p<0.0001$ for all three). All post hoc pairwise comparisons between 15 N, 30 N and 60 N were significant for all hemoglobin measures ($p<0.0001$) and are depicted in Figure 14. Similar results occurred when period was increased. CAM increased with increasing period and all pairwise comparisons between 5 sec, 10 sec and 20 sec were significant ($p<0.0001$) for O_2Hb, tHb and HHb. A significant main effect of cycle number was detected for O_2Hb, tHb and HHb ($p<0.0001$). Post hoc comparison revealed that the first cycle had significantly larger CAM for O_2Hb, tHb and HHb

(p<0.0001). There was also an effect of STT on CAM for O_2Hb, tHb and HHb. When STT increased, CAM also increased.

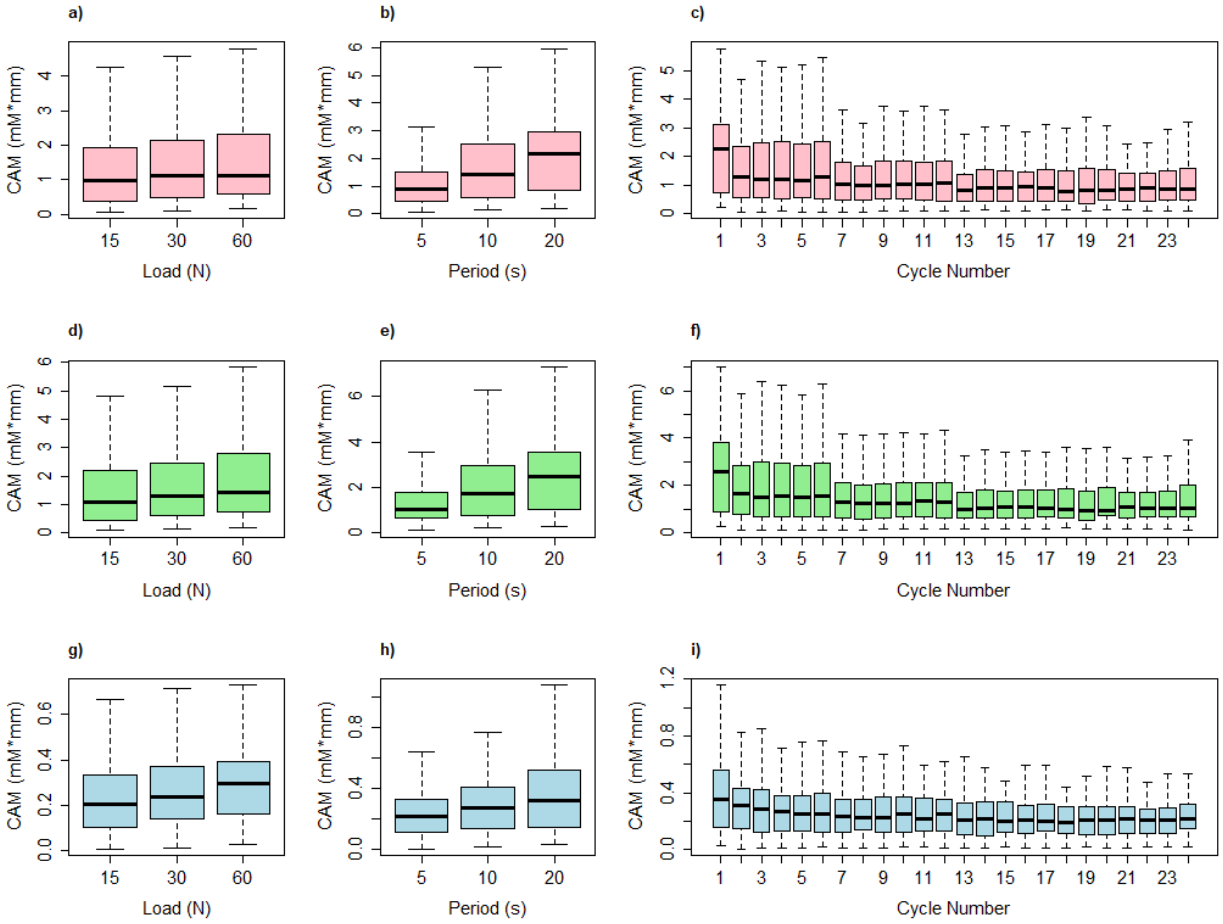

Figure 14: Box plots of cyclic amplitude (CAM) data for O2Hb (a, b and c), tHb (d, e and f) and HHb (g, h and i).

3.5.5 CYCLIC REOXYGENATION RATE

CR increased slightly when contact force was increased and post hoc pairwise comparisons revealed differences between all load levels (p<0.05). No effect of period or cycle was detected for CR. There was a significant effect of STT on CR (p=0.003).

3.6 DISCUSSION

In this study, we demonstrate that transcutaneous skeletal muscle NIRS data is susceptible to contact force artefact, and this artefact is affected by both magnitude and duration of external loading. In addition, contact force artefact is magnified by increased STT.

Oscillating contact forces between 15 N to 60 N (approximately 6.3 to 25 kPa) cause O_2Hb and tHb concentration changes that resemble data generated during active, cyclic muscular contractions because both O_2Hb and tHb decreased during the applied contact load and recover toward baseline when the contact load is released; however, the magnitude of decrease is smaller than decreases associated with muscle contractions (unpublished results). HHb data during elevated contact force do not follow trends normally observed during muscular contractions because, in this study, the typical response to contact load is a decrease in HHb concentration. These general patterns were observed during both static and cyclic loading, with the magnitude of contact load influencing all outcome measurements (peak changes, PC; cyclic average, CAV; cyclic amplitude, CAM; cyclic reoxygenation rate, CR; and final reoxygenation rate, FR).

Varying the period of cyclic loading had no effect on PC or CR, but longer periods were associated with differences in CAM and CAV. Similar rates of change during unloading (i.e. CR) and loading should be associated with greater CAM at longer periods because the tissue has more time to react to the applied load. Logically, then, if CAM increases then CAV should increase as well. Reoxygenation rates have

been shown to be influenced by ischemic injury[74], which is unlikely in our experiment because contact load magnitudes were low and the duration was brief, so the recorded effects of period are reasonable.

Cycle number affected CAM and CAV, where the initial loading cycle differed from the remaining cycles. The tissue's viscoelastic response to load is most likely the main cause for this finding. Unbound fluid, either blood within vasculature or interstitial fluid, may be redistributed away from the measurement volume during loading, which causes a time-varied response that stabilizes after initial fluid motion. During loading, tHb decreases and these changes suggest an associated decrease in blood volume. As interstitial fluid is redistributed away from the measurement volume, the density of scattering components of the tissues increases, which will affect the scattering coefficient and affect NIRS data[59]. Fluid motion was also suggested as an explanation for why breast tissue has a time-varying response to compressive loading [73]. Skin also exhibits a time varied response to contact load during the first 30 seconds of loading at 66 kPa [72].

Fluid redistribution is likely accompanied by compression of the superficial tissues. Toomey *et al.*[75] used ultrasound to demonstrate that 40 kPa (12.7×47.1 mm contact area, 7.2 N applied force) of contact pressure resulted in a 24% reduction in STT on mid-thigh. Approximately 25 kPa was applied to the thigh in the current study, so it is reasonable to assume that some compression of the superficial tissues occurred.

Larger STT were associated with a greater magnitude of response for all outcome measures (PC, CAV, CAM, CR and FR) and this effect may be related to the compression of superficial tissue while under load. Li and Tin [58] performed contact force measurement directly on rat heart tissue and suggested that small contact pressures (approximately 50 kPa) were not sufficient to compress muscle tissue. In their case, the heart was beating, so the modulus of elasticity may be greater than relaxed skeletal muscle, though it suggests that compression might be isolated to overlying tissues. Unpublished results from our lab demonstrated no interaction between muscle activation and the effects of NIRS contact force, which also suggests that STT is the primary contributor to contact force artefact. As superficial tissue is compressed, detected photons spend, on average, a greater time within muscle tissue (based on unpublished simulation results). Compressed superficial tissues take up a smaller portion of the 'banana shape' that photons traverse during measurements; therefore, photons spend more time in muscle tissue. This is an oversimplification, but it serves as a conceptual idealization. Experimental evidence[65] of increased transmittance through *in vitro* tissues subjected to compression supports the idea that a greater proportion of photons should reach underlying muscle. Given that muscle has higher absorption coefficient[76], in part from myoglobin concentrations, the optical density can increase during external loading. The interplay between increased transmittance through superficial tissue and greater optical density of muscle[77] is likely one of the main causes for the trends we observed in response to contact loads.

Computed changes in hemoglobin concentrations are influenced by thickness changes in the superficial tissues, but they may reflect the *in vivo* hemodynamic

response to loading. Specifically, vascular compression could influence the measured relative concentrations of O_2Hb and HHb. Bringard *et al*[78], demonstrated that HHb decreased and TOI increased when subjects wore compression stockings with low contact pressure (at 3 kPa). They suggested that venous vasculature was compressed at 3 kPa, but arterial vasculature was not. Consequently, HHb should be redistributed away from the measurement volume, but O_2Hb should not, thereby increasing the TOI. Carp *et al*[73] suggested a similar mechanism to explain NIRS data from breast tissue subjected to compression. The authors suggest that the non-vascular portion of breast tissue supported external loads and prevented total arterial occlusion, which resulted in observed increases in tHb during sustained loads. The loads associated with tissue compression in Carp's study were not well quantified, though contact pressures during mammograms is roughly 10 kPa[79,80].

In contrast to these increases in TOI and tHb observed with, respectively, lower extremity compression garments and compression of breast tissue, in the current study, tHb did *not* increase while the contact force was applied. This strongly indicates that blood was redistributed *away* from the measurement volume when external load was present. It may be caused by arterial occlusion during loading, consistent with measurements of capillary closing pressure of ~4 to 4.6 kPa[81], which is less than what was applied in this study but greater than the estimated pressure of the aforementioned compression garments[78]. When contact pressure is applied directly to cardiac[58] and skeletal[59] muscle tissues, tHb decreases in response. In both tissues, vascular compression is proposed as a possible mechanism. Concomitant increases in HHb and decreases in TOI[58,59] suggest that both arterial and venous vasculature

compression occurs in striated muscle. Non-vascular components of muscle tissue may not be able to support external loads without vascular compression in a manner similar to that speculated in breast tissue[73], so muscle should be more susceptible to decreased tHb and increased HHb during loading. In the current study, three subjects experienced an initial decrease in tHb followed by a gradual increase in HHb, which would be consistent with O_2Hb to HHb conversion. These subjects had lower STT, so it is possible that the effects of vascular compression in participants with less subcutaneous adipose tissue (i.e., thinner STT layers) were more characteristic of skeletal muscle than they were in participants with more subcutaneous adipose tissue (i.e., thicker STT layers). A contributing factor to the response of these three subjects may be athletic fitness. This was not formally explored in the study, but two of these three subjects maintained physically active lifestyles, so increased capillarization, myoglobin concentrations and/or mitochondrial capacity may also play a role in the hemodynamic response.

These different hemodynamic trends suggest an interplay between two different mechanisms that affect NIRS data. In subjects with thinner STT, NIRS instruments may be able to detect compression of skeletal muscle vasculature, especially capillaries. In subjects with thicker STT, on the other hand, NIRS instrument may be susceptible to artefact caused by altered optical properties associated with superficial tissue compression. While the results lend support the to the second (measurement artefact) mechanism, further work is required to confirm vascular compression as a function of STT and contact pressure.

3.6.1 LIMITATIONS AND FUTURE WORK

The author applying the contact load (TS) braced each subject's knee to minimize the subject's tendency to provide a resistive force to the contact loading. Preliminary trials with and without bracing suggested that bracing the knee was adequate to prevent involuntary muscle activation, though muscle activation could have influenced the NIRS data of the three subjects who exhibited gradual increases in HHb during loading. Muscle electrical activity was not monitored with electromyography during contact pressure loading, so we cannot confirm any possible role of muscle activation in data from these or other subjects.

STT measurements were made with calipers, and they were not expected to give accurate values when compared to ultrasound measurements; however, the trends of STT should be robust to the accuracy of the calipers because both caliper measurements and ultrasound measurements are linearly related to STT[33]. However, the relative error associated with calipers is estimated at 43% when compared to ultrasound, so our statistical results for STT were focused on trends rather than direct comparisons between exact values.

To address these issues, future work will measure STT directly using ultrasound in conjunction with NIRS measurements. In addition, direct measurement of vascular compression or microvascular flow during external loading would provide evidence to either support or refute the speculated mechanisms.

3.6.2 SIGNIFICANCE OF FINDINGS

Computed hemoglobin data from NIRS measurements of vastus lateralis are sensitive to contact forces between the NIRS device and skin. These effects need to be considered when interpreting NIRS data to differentiate between real physiologic changes and measurement artefacts. At the very least, NIRS measurements subjected to varied contact forces (for example, measuring from vastus lateralis during cycling could result in varied contact forces, depending on fixation techniques) should be given a preconditioning period before baseline measurements are recorded. This will minimize viscoelastic effects associated with the first few loading cycles. STT may play an important role when quantifying measurement artefacts related to contact force. Future development of photon propagation simulations and a device capable of real time STT monitoring and NIRS will help to quantify measurement artefacts.

CHAPTER 4: PHOTON PROPAGATION IN A TISSUE COMPOSITE

Disclaimer: The content of this chapter will be submitted to a peer-reviewed for publication and copywrite for the manuscript will agree with the journal's policy. The roles of each contributing author are listed in Table 5.

Table 5: The roles of each author for the photon propagation investigation.

Author	Role
Timothy Schwab	• Determine simulation design requirements and inputs • Data extraction and analysis • Interpret findings • Write paper
Rodrigo Santoro Silverio	• Reproduce original C code in JAVA and implement multithreading
Dr. Alex Aravind	• Act in a supervisory role including, but not limited to, the following aspects of the investigation: simulation design, data analysis, and manuscript review.
Dr. R Luke Harris	• Act in a supervisory role including, but not limited to, the following aspects of the investigation: simulation design, data analysis, and manuscript review.

4.1 ABSTRACT

Near infrared spectroscopy (NIRS) is an imaging modality that computes relative changes in oxygenated and deoxygenated hemoglobin based the diffuse reflectance of photons emitted into tissue. When determining hemoglobin contractions in muscle, photons propagate through superficial tissues (skin and adipose tissue) before and after passing through muscle. Knowledge of the path of photons is critical to accurate measurement of underlying muscle and this path is influenced by the optical properties and thickness of the superficial tissue. Our purpose was to simulate the effects of tissue optical properties and superficial tissue thickness on photon propagation through a composite of skin, adipose tissue and muscle. Our Monte Carlo simulation suggests that photon-muscle interactions are strongly influenced by superficial tissue thickness, and muscle properties could be recorded at depths less than 12 mm. Future work with our model will aim to optimize NIRS hardware design.

4.2 BACKGROUND

Near infrared spectroscopy (NIRS) is a method for measuring *in vivo* hemoglobin concentration changes in tissue. Concentration changes are measured relative to a baseline and are computed with the intensity of diffuse reflectance, coupled with a modified Beer-Lambert law[26]. Measured hemoglobin concentration changes are simply trends that can be difficult to compare across individuals. Some NIRS systems - time-domain and frequency-domain - are able to measure absolute values of hemoglobin concentrations. Both the time and frequency domain systems

achieve this by measuring time of flight to infer the pathlength of reflected photons travelling in tissue. While knowledge of the pathlength is valuable for hemoglobin concentration calculations, it does not define where the photons are travelling within tissue. For example, pathlength does not quantify how far photons propagate in each layer of a tissue composite.

Computer simulations and experimental models[6,10,11,34,35,82,83] provide better estimates of how photons propagate through tissue. Many simulations focus on how photons propagate through brain[12-15,17,84], though a few studies have investigated how photons propagate through muscle[18,34,35,82,83]. While both measurements sites are modelled through either diffusion equations or Monte Carlo simulations, the anatomic variability in subcutaneous adipose tissue thickness is an added variable that confound NIRS muscle measurements. To measure from muscle, re-emitted photons must propagate though a composite of skin, adipose tissue and muscle (together, referred to as a tissue composite), so reflected intensity is a result of the combined absorption and scattering in all of these tissues. Given the variation in thicknesses and optical properties of these tissues, the relative contribution of muscle to the reflected signal intensity is not fully understood.

Knowledge of photon propagation through a tissue composite is critical to obtaining the most accurate data from the underlying muscle tissue, especially in situations where superficial tissue thickness (STT) varies dynamically in response to contact pressures[75] between the NIRS device and the skin. Previous layered media simulations of photon propagation in muscle are very informative regarding potential crosstalk and underestimation errors[34], maximum STT where a homogeneous media

assumption is acceptable[34,82,83] and spatial sensitivity maps[18,82]. These previous investigations used either single values[34,35,82] or a tight range on values[18,83] for inputted absorption and scattering coefficients. These optical properties may not reflect natural intra-subject and inter-subject variation that is observed *in vivo*[19,76]. In addition, scattering coefficients are thought to change when contact loads are increased[59,69]. Two of these studies[18,82] investigated photon propagation with short source-detector separations (SDS), though the spatial sensitivity maps for these short-SDS were not presented. Additional data regarding the spatial sensitivity of short SDS would be beneficial when attempting to filter the contributions of superficial tissues when STT is dynamically changed (for example, during cyclic motions where contact loads fluctuate as a result of fixation techniques).

Lastly, researchers quote maximum penetration depths equal to one half of the SDS[38,39,77], when experimental[6,10,11] and computational models[12-15,17,34,35,82-84] suggest average penetration depths closer to one third of the SDS. Despite this discrepancy, we suggest that average (or maximum) depth may not adequately describe where the reflected signal attenuation occurs. A computational model that tracks how photons propagate in each tissue layer would be more informative and could be used to optimize NIRS device design. For example, detailed knowledge of photon propagation through a tissue composite could be used to optimize superficial tissue filtering, by adapting SDS based on tissue thicknesses, or enhancing depth selectivity within muscle.

4.3 PURPOSE

Our purpose was to model photon propagation and absorption through a tissue composite of skin, adipose tissue and muscle. We were interested in quantifying photon paths during diffuse reflectance, with a focus on (i) how far the photons propagated through muscle, (ii) how much absorption occurred in muscle and (iii) describing the path behaviour through aggregate tissue. Specific emphasis was leant to photon propagations between short SDS.

4.4 METHODS

4.4.1 OVERVIEW OF MONTE CARLO

We implemented a Monte Carlo simulation of photon propagation that was first described by Wang *et al*[85] and we used the simulation to model diffuse reflectance of photons propagating through skin, adipose tissue and muscle. In the simulation, photon packets are launched from a point source and undergo diffuse reflectance within the tissue composite. When each photon packet enters the tissue, it is displaced within the tissue to a point where it undergoes both an absorption event and a scattering event. The distance a photon packet travels between events is governed by an exponential distribution based on the scattering and absorption coefficients (distance=-ln(ξ)/(μ_s+μ_a), where ξ is a random number between 0 and 1, μ_s is the scattering coefficient, and μ_a is the absorption coefficient). The cosine of the scattering angle is computed with the Henyey-Greenstein phase function as described by Wang

et al, which models experimental data well[86]. Absorption decrement was computed by multiplying the photon packet weight by (μ_a*L-0.5(μ_a*L)^2) which was used to approximate the expression exp(-μ_a*L), where L is the photon packet step size. It is this decrement that leads to the term photon packet, instead of simply referring to photons. For simplicity, we will use the term photon for the remainder of the paper. At boundaries between tissue layers, Fresnel's equations were used to determine the probability of internal reflection.

This process of scattering and absorption occurs in 3 dimensions and the path of a photon is recorded if the photon exits the tissue and enters a virtual detector. The detectors are square (5 mm x 5 mm) and located at SDS = 2.5, 5, 7.5, 10, 20, 30, and 40 mm.

Our simulation is implemented in Java (Java 8, Oracle Corporation, USA) and optimized for multi-threading to decrease simulation times.

4.4.2 MONTE CARLO DETAILS

Photon propagation is dependent on the values of μ_s, μ_a, anisotropy (g), and the index of refraction (n) for each layer. Published values for these optical properties vary depending on the experimental technique used to observe them, so our simulation incorporates a range of possible optical properties because previous work suggest that simulation results can be sensitive to optical inputs[34]. Table 6 lists the ranges of each optical property at similar wavelengths to those commonly used in NIRS (600 nm to 850 nm). For simplicity, variables listed in Table 6 are assumed to have a uniform distribution between the lower and upper bounds because the true

underlying distribution is unknown. The values of each optical property were randomly selected from the ranges defined in Table 6 for each photon-tissue interaction.

Table 6: Ranges of optical properties of skin, adipose tissue and muscle

	Skin	Adipose	Muscle
μa (cm-1)	0.16 to 0.64 [19]	0.003 to .09 [76]	0.12 to 1.08 [19]
μ_s' (cm^{-1})	21 to 29 [76]	12 to 14 [76]	4 to 6 [76]
g	0.45 to 0.9 [76]	0.9 to 0.93 [76]	0.7 to 0.95 [76]
n	1.37 to 1.38 [87]	1.455 to 1.467 [88,89]	1.38 to 1.405 [88-90]

We purposefully varied two factors: adipose tissue thickness and SDS. Adipose tissue thickness was assigned values of 1, 4, 7, 10, 13, 16, 19, and 21 mm. The SDS was set at 2.5, 5, 7.5, 10, 20, 30, and 40 mm. We held the skin thickness constant at 2 mm as this was a representative value given that site specific values vary between 1.6 mm and 2.5 mm[91]; therefore, we combined the adipose tissue thickness with the skin thickness to define the overall STT. This resulted in STT values of 3, 6, 9, 12, 15, 18, 21 and 24 mm. NIRS is typically used to measure from muscles where the STT is less than 10 mm[92], so the larger values of our inputs may seem less applicable; however, clinical populations often exhibit these higher STT.

4.4.3 ANALYSIS

When a photon was re-emitted into a detector, we stored the path coordinates and computed several outcomes. We computed differential path length factor (DPF) by adding the displacements between scattering locations along a photon's path and

dividing by the SDS. We computed the average depth (AD) by taking the average of the scattering locations. We quantified the interaction with muscle by defining the path length in muscle (PLM, %) and normalized absorption in muscle (NAM, %). PLM is computed by adding the displacements between scattering locations within muscle and is expressed as a percent of the total pathlength. NAM is the percent attenuation caused by absorption while the photon was within muscle tissue. To visualize how photons propagated through the tissue composite, we generated spatial sensitivity maps where the depth of photon-tissue interactions was characterized with respect to the axis defined by the emitter and detector (x-axis). Each profile was normalized to the maximum number of tissue interactions recorded in a specific pixel.

4.5 RESULTS

We ran 56 simulations, one for each STT and SDS combination, and recorded the paths and intensities of photons that were re-emitted into the detector. Based on preliminary simulations, we aimed to record 400 photons at each detector. This was easily obtained (577 ± 140, mean ± standard deviation, with a minimum of 409) by launching between a minimum of $1x10^5$ photons (STT = 24 mm, SDS = 2.5 mm) and a maximum of $2x10^9$ photons (STT = 3 mm, SDS = 40 mm).

Both STT and SDS affected PLM, NAM and AD. Means and standard errors for the outcomes are shown in Figure 15. AD increased with increasing STT and increasing SDS, though this greater AD did not correspond to more muscle penetration. Both PLM and NAM increased with decreasing STT and increasing SDS.

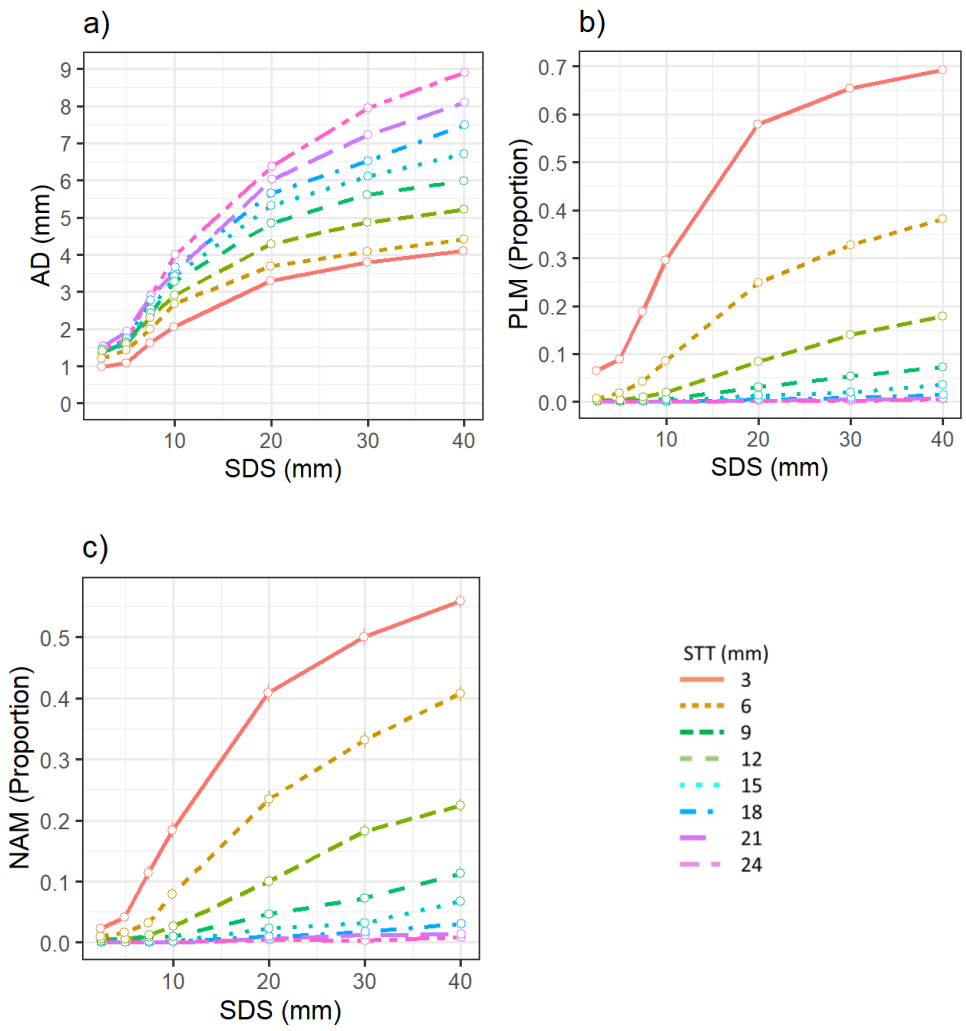

Figure 15: a) Average depth, b) path length in muscle, and c) normalized absorption in muscle as a function of SDS. Each line represents a different STT (cm) as labeled below the chart. The points represent mean values and the whiskers are the standard errors.

Inspection of Figure 15 suggests some potentially important thresholds. Measurements and simulations of cerebral photon propagation [9] suggest that a partial pathlength factor (equivalent to PLM) of 5% is sufficient to measure hemoglobin changes, so this was chosen as a threshold. PLM was below 5% at all SDS when STT was greater than or equal to 15 mm. PLM was above 5% at SDS ≥ 3 (typical distances

employed in NIRS measurements) when STT was 12 mm or less. At these same SDS and STT ranges, NAM had a minimum value of 7.3%. At short SDS (≤ 5 mm), PLM was less than 5% for all STT except STT = 3 mm. Also, at SDS ≤ 5 mm, NAM was below 1.6% for all STT, except STT = 3 mm. When STT was 3 mm, PLM had a minimum value of 6.5% and NAM had a minimum value of 2.3%.

Spatial sensitivity maps displaying where photons interact with tissue are depicted in Figure 16. The two outermost contours in the figure correspond to 1% and 5% of the max number of tissue-photons interactions, and the remaining contours are 10% increments (i.e. 10%, 20%, 30%...). When STT is thick (≥15 mm), the photon propagation in the tissue composite was very similar to that expected in a homogeneous medium because photons largely travelled in the adipose layer. In these cases, the expected “banana shape” was evident. However, when STT was thin (<12 mm), the banana shape was compressed because photons reflected from the tissue boundaries.

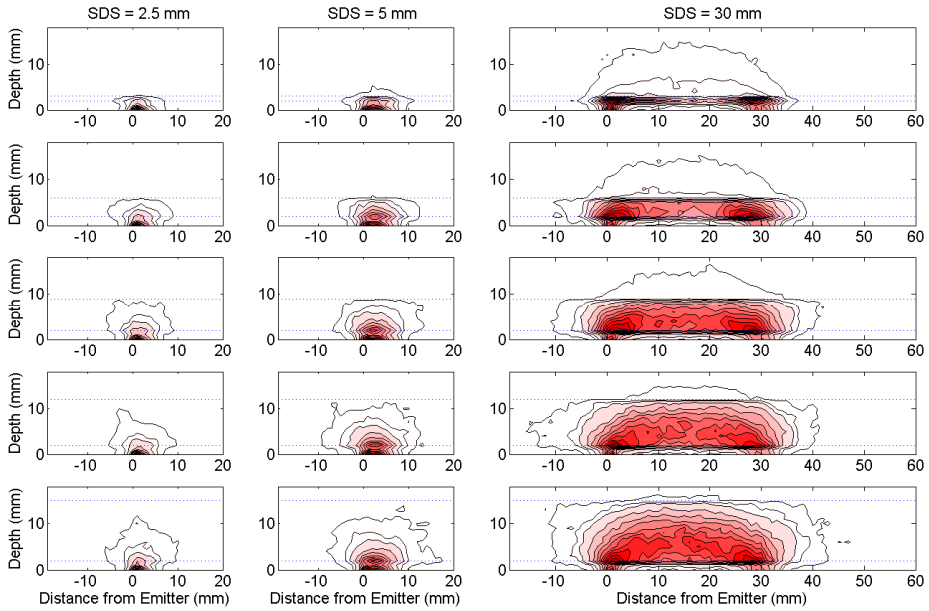

Figure 16: Spatial sensitivity maps depicting depth of photon-tissue interactions for a variety of SDS and STT. STT = 3, 6, 9, 12, and 15, arranged in rows with 3 in the top row. Horizontal dashed lines depict the boundaries of the adipose tissue layer. The two outermost contours correspond to 1% and 5% of the max number of tissue-photons interactions, and the remaining contours are 10% increments (i.e. 10%, 20%, 30%...). Contours at SDS = 40 mm were similar to that of SDS = 30 mm, so they were not displayed.

The spatial sensitivity maps show a difference between muscle penetration at different SDS. Longer SDSs are associated with more muscle penetration. For example, some 5% contour lines penetrate muscle at SDS = 30 mm and 40 mm, but not at SDS = 2.5 mm and 5 mm. While not evident in Figure 16, the 1% contour does penetrate into muscle with an SDS of 2.5 mm and an STT of 3 mm, but not at greater STT. Contours at SDS = 40 mm were very similar to SDS = 30 mm, so they were omitted from the figure.

4.6 DISCUSSION

Our simulations yield three main findings: (1) our model is valid because our computed values agree with published experimental and simulation results, (2) a cut off threshold for STT (approximately 12 mm at an SDS of 4 cm) exists where photons fail to propagate a large amount in muscle, and (3) limiting photon propagation to superficial tissues can be accomplished with different SDS for each STT.

4.6.1 MODEL VALIDATION

We compared our DPF (Figure 17) to literature values to validate our simulations. Duncan *et al*[8] used a frequency domain NIRS system (SDS = 45 mm with wavelengths between 690 and 832 nm) to compute the DPF on forearm, calf and head. DPF varied with both location and sex, and the authors suggested that these effects were influenced by adipose tissue thickness, though specific values were not reported. Our data corroborates this suggestion because we found that DPF was influenced by STT. In Duncan *et al.*'s study, DPF values were lowest on male forearms, with a range of 3.53 to 3.96, presumably because adipose tissue thickness was the smallest. The highest DPF measured from transcutaneous muscle measurement was from female calf muscle, ranging from 5.9 to 6.41. A direct comparison between these data to a specific STT is difficult because adipose tissue thickness was not reported by Duncan *et al*; however, typical forearm STT is 3 mm in males[30] and typical calf STT ranges from 4 to 21 mm in females[93]. Based on these STT values, our DPF on male forearm would be 4.3 (approximated with SDS of 40 mm). Our computed DPF on female calf would be between 5.0 and 16.8. Our DPF

estimate for forearm is within 15% of experimental findings, and our low range estimate of calf DPF aligns with experimental results, though our upper limit is much higher than experimental results. In an experimental setting, an STT of 21 mm will compress when a NIRS device is applied (for example a 25% reduction is expected at typical NIRS contact pressures[75]) so the effective STT will be thinner and the measured DPF may be lower than expected given an uncompressed thickness. When adjusting for a 25% reduction, our simulated DPF is still higher than experimental results. This comparison suggests that our simulation may overestimate DPF but thinner STT simulations are reasonable. Some of the disagreement between *Duncan et al.'s* experimental evidence and our simulation results likely stems from the uncertainty of their unreported STT. Despite these differences, our PLM results agree with other experimentally validated simulation results[34,35] and minor differences between these studies can be attributed to differences in computing photon decrement values.

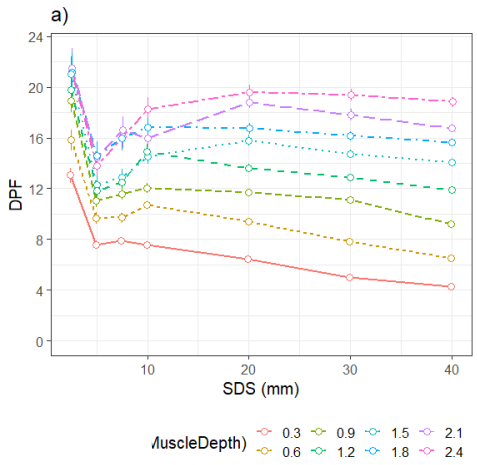

Figure 17: a) Differential pathlength factor (DPF) as a function of SDS (cm). Each line represents a different STT (cm) as labeled below the chart. The points represent mean values and the whiskers are the standard errors. No post hoc significant differences detected between SDS 3 and SDS 4, though all other SDS comparisons yielded statistically significant results.

Comparison of our average penetration depth to experimental data is more challenging because experimental data is typically based on homogenous phantoms with different optical properties than that of a tissue composite. Cui *et al*[6] used a phantom with optical properties similar to adipose tissue to determine the depth where photons are most likely to dwell as a function of SDS (Depth = 0.22*SDS+0.092 cm). Their results are very similar to our simulated AD when STT was thick enough to approximate a homogenous medium (18 mm ≤ STT ≤ 24 mm). For example, our AD at SDS = 3 and STT = 24 mm was 7.9 mm in comparison to 7.5 mm estimated by Cui *et al.*'s empirical curve.

In addition, our data is similar to that measured by Patil *et al*[10]. Patil determined probability distributions for the penetration depth in a phantom (with optical properties

similar to a combination of adipose and muscle tissue) and quantified the penetration depth with the 3rd quartile of the distribution. They reported 3rd quartile penetration depths of 10, 13 and 15 mm for SDS of 20, 30, and 40 mm, respectively. Our simulation that best approximated their experimental setup has an STT of 24 mm. Third quartile depths of our data are 10.5, 11.9 and 12.8 mm, which are very close to those of Patil *et al*.

The above comparisons suggest that our simulated DPF, AD and spatial distributions are reasonably close to experimental data collected from both *in vivo* tissues and tissue phantoms. Given this corroboration and the fact that the Wang *et al*[85] physics engine is widely accepted as an appropriate model, we are confident that our simulated data is representative of *in vivo* data.

4.6.2 PHOTON-MUSCLE INTERACTIONS

We are interested in measuring hemoglobin concentration changes in muscle using NIRS, so quantifying the interactions between photons and muscle tissue and delimiting these interactions from those between photons and superficial tissues is important. These interactions are best quantified with PLM and NAM. Not surprisingly, both PLM and NAM follow the same general trends, and we focus on PLM because there is published simulation data[18,34,35] for comparison. Figure 18 depicts the PLM data from these studies with an SDS of 30 mm. All data follow the same general trend where PLM increases with decreasing STT, though our data seems to undergo less pronounced changes when compared to other simulations. This smaller rate of

change in our simulations are most evident at mid-range STT where our data may overestimate PLM.

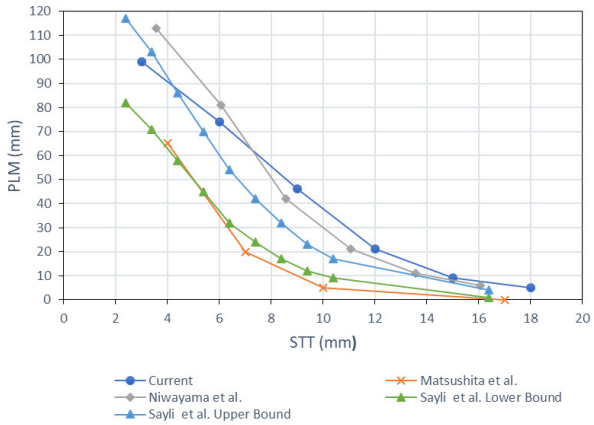

Figure 18: Absolute values of pathlength in muscle (PLM) in mm, rather than % of total pathlength, as a function of superficial tissue thickness (STT). Data was extracted from the following published figures: Niwayama et al, Fig 1; Matsushita et al, Fig 3; Sayli et al, Fig 3.

At what PLM is useful information still attainable? Cerebral work (Figure 7a in [9]) suggests that a partial pathlength factor (PLM) of 5% is sensitive enough to examine deeper tissues. While a 5% cut off may seem somewhat arbitrary, it agrees with previous work[83] where errors are minimized with an STT less than 5 mm and an SDS of 30 mm. In other words, at an SDS of 30 mm, a homogeneous media assumption (non-layered) is acceptable for STT less than 5 mm. Inspection of Figure 16 reveals that the 5% contour extends into muscle with a STT of 6 mm; therefore, we suggest cases where the 5% contour extends into muscle be acceptable to assess hemoglobin changes within muscle.

Our simulations indicate that PLM muscle was below 1% at all SDS when superficial tissues were at least 15 mm thick, and we are doubtful that this is sensitive enough to detect hemoglobin changes within muscle; therefore 12 mm would be the maximum STT where useful information could be acquired from muscle tissue. Given that our simulation estimates higher PLM, some caution should be used when applying this 12 mm cut-off and this should be taken as an absolute maximum though it generally agrees with the 10 mm cut-off often implemented by NIRS researchers[92]. For comparison, Matsushita *et al.*'s model predicted that a 0.1% contour would fall within muscle at STT = 15 mm. Our data suggest that NIRS techniques may function adequately when superficial tissues are slightly thicker than the commonly accepted cut-off values of 10 mm, especially if superficial tissue contribution is filtered out (see Section 4.3).

A 12 mm cut-off does not mean that clinical populations with greater STT cannot be measured using NIRS. When a NIRS device is applied to the skin, superficial tissues will compress[75] and the effective STT will be lower than that in an unloaded state. If sampling from populations with larger STT, simultaneous readings of NIRS data and STT would be beneficial to assess data integrity and this concept will be explored in future research.

4.6.3 IMPLICATIONS FOR SUPERFICIAL TISSUE FILTERING

Some NIRS devices rely on a superficial filter to separate the effects of superficial tissues from those of deeper tissue, especially cerebral NIRS systems. Cerebral superficial filters are implemented with a short SDS (5 mm or less) used in

combination with longer SDS (30 to 45 mm). These distances work for cerebral measurements, though they might not be applicable for muscle measurements because STT is more variable between subjects. In muscle measurements, filtering should be able to accommodate a variable STT.

As discussed in the previous section, our PLM results suggest that a cut-off below 12 mm would still allow some muscle tissue penetration for an SDS of 40 mm, and our NAM results agree with these values. We computed a NAM of at least 11% occurred with superficial tissue thickness of 12 mm or less (using an SDS of 40 mm). Near these lower limits of photon propagation in muscle, the contributions of superficial tissues should be filtered from the signal. Diffusion theory can be used to demonstrate that superficial layers less than 4 mm may not require filtering[94,95] and measurements through superficial layers greater than 12 mm are not representative of deeper layers[94]. Similarly, Yang *et al*[83] used a 2 layer Monte Carlo simulation to demonstrate that an adipose layer less than 5 mm may not require correction for the superficial layer. Based on these results, we suggest that intermediate STT values, those between 3 mm and 12 mm, should be filtered to remove superficial signal because the signal contains information from both layers.

The implementation of a superficial filter for muscle measurements is also influenced by the between-subjects variability of superficial tissue thickness. Our simulations suggest that an SDS of 2.5 mm would be adequate for STT greater than 3 mm (where both PLM and NAM are less than 1%). Data presented in Figure 16 suggest that an SDS of 2.5 mm would provide information weighted on the skin layer and may not reflect optical changes in the adipose layer. In the case where data from

the adipose layer would be considered beneficial, then an SDS of 5 to 10 mm, depending on adipose layer thickness, could be used for the main signal with a filtering SDS less than 2.5 mm. Further, a simulation, like the one presented in this paper, would be an excellent tool for developing a NIRS instrument that optimizes superficial filtering based on superficial tissue thickness.

4.6.4 LIMITATIONS AND FUTURE DIRECTION

Our simulations had several limitations that we plan to explore and develop with future research. First, there is a high amount of variability in published tissue optical properties and this variability influences the results[34,83]. Published optical properties largely agree with each other, though differences exist due either to methodological differences, to wavelength dependencies or to between-subject variability. Rather than selecting specific values for each optical property, we chose to input a range of optical input values. Input ranges add variation to simulated data, though they might be more representative of the variability in human tissue.

The geometry of our tissue was a simple horizontal layering. Simple layering does not represent the complex geometry associated with shape of muscles and their overlying tissues. Nor does it account for geometric changes associated with tissue compression; however, we expect that the effects of these geometric inputs and the optical properties would not be as pronounced as that of STT.

As seen in Figure 16, a combination of geometry and optical properties strongly influences photon propagation. The high scattering coefficient in adipose tissue concentrates photons within the adipose layer during propagation [35,82,96]. When

boundary layers are modelled[18], high scattering is coupled with internal reflection off boundary layers which influences the spatial sensitivity. Our simplification of a flat boundary causes a more delineated propagation boundary between skin and adipose tissue than we expect in reality because the optical properties are more likely to display a gradual shift rather than an instantaneous change. The *in vivo* boundary between adipose and muscle aligns better with our model though we did not attempt to model the influence of muscle fascia.

Our model predicts larger DPFs than experimental results and we suspect this is due to the influence of adipose tissue. *In vivo*, superficial tissues are compressed when a NIRS device is fixed in place, so we question whether STT measurements prior to measurement are adequate to describe STT. To investigate this effect, we plan to design a new device that incorporates real-time STT measurements during NIRS data acquisition to clarify the connection, if any, between DPF and STT.

In the future, we plan to add some new functionality to our model. First, we will incorporate muscle anisotropy as we suspect this will influence how photons propagate within muscle. Second, we need to model hemoglobin changes in the tissue layers to help refine our PLM cut-off values. In this paper we suggest a 5% PLM may be sufficient to collect data from underlying muscle. Future modelling of hemodynamics will help to refine this value and will inform design decisions of new hardware that incorporates in superficial filtering.

4.6.5 CONCLUSION

We conclude that our simulation provides valuable insight into the propagation of photons within a tissue composite. Perhaps most striking is the influence of the superficial tissues on photon propagation and this helps explain why superficial tissue compression results in a measurement artefact (unpublished results). From a practical perspective, we suggest that NIRS data should not be recorded when superficial tissues are thicker than 12 mm, though this value is somewhat preliminary and tissue compression should be factored in. Lastly, we conclude that superficial filtering is important for muscle measurements and this filtering could be optimized with different source detector distances for different superficial tissue thicknesses.

CHAPTER 5: GENERAL DISCUSSION AND SIGNIFICANCE OF MY RESEARCH

The new knowledge contributed by my research can be summarized as follows.

5.1 SUMMARY STATEMENT OF MY RESEARCH

Contact force artefact is a confounding factor in the transcutaneous measurement of muscle Hb using NIRS because its effects mimic muscle activation; therefore, ideally, contact force effects need to be removed from detected signals to provide a better estimate of physiologic changes present in underlying muscle tissue. This phenomenon is not restricted to static forces. Rather, measurements taken during dynamic activities, where contact forces oscillate, will display a time-dependent nature, which adds a layer of complexity to the analysis of contact force artefact.

When interpreted together, the findings presented from each of my individual research experiments present possible mechanisms responsible for contact force artefact, and, therefore, the combined results can inform future research and drive strategies to minimize the artefact. Experimental and simulation results strongly suggest that STT is the primary contributor to contact force artefact. When superficial tissues are compressed in response to elevated contact force, a greater percentage of photons propagate through muscle whereby the NIRS signal is altered. In NIRS measurements involving thinner STT, contact forces may induce compression of underlying skeletal muscle vasculature. Regardless of the thickness of superficial

tissues, NIRS instruments may be susceptible to artefact caused by altered optical properties associated with superficial tissue compression.

5.2 OVERVIEW OF MAIN FINDINGS

5.2.1 STATIC CONTACT FORCE

An elevated, constant contact force is associated with increases in peak changes in O_2Hb, HHb and tHb in a manner similar to that expected during a muscle contraction. This pattern is consistent regardless of measurement location or muscle activation, though the magnitude of the changes is greater when measured from larger muscles (for example, VL) in comparison to smaller muscles (for example, SCM). Despite the differences in magnitude between measurement locations, there is no interaction between measurement location and contact force, which means that all muscles behaved in a similar fashion in response to contact force increases.

In general, peak changes associated with contact force alone are smaller in magnitude than those associated with muscular contraction, regardless of the measurement location. Both contact force and muscle contraction have similar responses that are superimposed, making it difficult to separate the two effects during physiological investigations.

Static contact force results depict clear effects for the main factors, but the results are only applicable to situations where contact forces are kept constant during

testing. This is difficult to accomplish when measuring a dynamic motion, so additional insight into the time-dependent behaviour of contact force is required.

5.2.2 OSCILLATING CONTACT FORCE

Oscillating contact force alters NIRS data in a time-dependent manner, presumably as a result of tissue viscoelastic properties. Similar to a static contact force, the greater oscillating contact forces magnify the peak changes in O_2Hb, HHb and tHb. Data show a viscoelastic-like response when tissues are subjected to an oscillating force. Specifically, Hb concentration deviates from baseline during the initial loading cycle(s) and does not return to baseline during the unloaded portion of each subsequent loading cycle. Following an appropriate recovery time (4 minutes recovery between trials) this phenomenon is evident again and this suggests that fluid redistribution plays a role in the tissue response.

Recovery rates (CR and FR) depend on the magnitude of contact force and are independent of period of loading. Here again, fluid redistribution may be the mechanism behind this behaviour. Tissue compression is associated with a loss of fluid[69,73] and tissue compresses more with higher contact forces. Upon release of a contact force, fluid pressure gradients may cause the tissue to return to its normal thickness. If the compressive strain rates during loading are also governed by magnitude of contact force, and corresponding fluid redistribution, in a similar fashion to recovery rates, then this suggests a mechanism that explains why longer periods are also associated with greater cyclic NIRS data changes (CAV and CAM). There is simply more time for fluid to redistribute and compression to occur. Currently, there is

no direct evidence where this fluid motion occurs. It could occur in skin, adipose, muscle or some combination of all three. Despite this ambiguity STT seems to play a prominent role. Larger STT values are associated with magnified NIRS data responses (PC, CAV, CAM, CR, and FR). The role of STT in contact force artefact likely arises from compression of superficial tissues and altered photon propagation through the tissue composite, though additional data is required to support this postulate.

5.2.3 PHOTON PROPAGATION IN A TISSUE COMPOSITE

Simulation of photon propagation through a tissue composite suggests that superficial tissues strongly influence how photons migrate from source to detector. Spatial sensitivity maps of photon propagation (see Appendix C) indicate that photons preferentially propagate through adipose tissue. This occurs because adipose tissue has a higher μ_s and lower μ_a, meaning that photons scatter more in adipose tissue and they are less likely to be absorbed. This can be thought of as the “path of least resistance” for photons. Even though photons are more likely to propagate within adipose tissue, they do propagate within muscle tissue, especially at lower STT. Beyond 12 mm STT, propagation within muscle diminishes to the point where reflected light does not represent muscle properties. At lower STT (< 3 mm), the detected signal is more representative of muscle tissue, and intermediate values (3 mm < STT < 12 mm) most likely reflect aggregate optical properties of all three tissue layers. When measuring through intermediate STT, superficial filtering would be beneficial to remove the component of the signal associated with the superficial

tissues. Ideally, this filtering could be optimized for varied STT by adjusting the short SDS used to filter the data.

The simulation itself is as important as the results generated with the program. I envision that this simulation will continue to be used and developed to gain insight into future NIRS analyses and help guide research. In the following section, for example, I use the simulation to help interpret some possible mechanisms responsible for contact force artefact.

5.3 GENERAL DISCUSSION

Taken together, the findings of my research inform future research toward understanding the mechanisms underlying contact force artefact and developing NIRS devices that minimise inter-subject variability, which should promote clinical uptake of MIRS measurements.

5.3.1 POTENTIAL MECHANISMS UNDERLYING CONTACT FORCE ARTEFACT

When contact force increases, superficial tissues are compressed[75] and photon propagation is altered. The mechanisms for this optical behaviour are unknown, but my experimental and simulation studies provide evidence that suggests there is an interplay between some or all of the following responses: vascular occlusion, adipose compression, skin compression, changes in optical properties, or improved optical coupling.

My experimental evidence suggests there are at least 2 general trends apparent in the optical response of a tissue composite. In both trends, tHb and O_2Hb concentrations decrease with increasing contact force. The difference between the two trends lies with Hb response. In one trend, Hb decreases with elevated contact force and continues to decrease (or remain somewhat constant) during the remainder of the loading. In the second trend, Hb increases during elevated contact force. These trends are most evident during static loading (see Appendix , 0% contraction data) because data isn't influenced by the recovery time during the unloaded portions of cyclic loading (see all data in Appendix to compare cyclic and static response). These two Hb trends do not appear to be mutually exclusive and, when combined, can result in an initial decrease in Hb followed by an increase in Hb over the duration of loading.

I propose that differing Hb trends are a result of one or more physical mechanisms acting simultaneously (see Table 7). First, vascular occlusion, both arterial and venous, could explain the trends that mimic muscular contraction, those with increasing HHb during elevated contact force. If both arterial occlusion and venous occlusion occur during loading, then tHb should decrease because blood is removed from the measurement volume; and O_2Hb should decrease with a concomitant increase in HHb as oxygen is consumed.

Table 7: Summary of effects for the proposed mechanisms that may be involved in the optical response of a tissue composite subjected to elevated contact load.

Mechanism	tHb	O_2Hb	HHb
Vascular occlusion	↓ if arterial and venous occlusion present ↑ if only venous occlusion present	↓ if arterial and venous occlusion present ↑ if only venous occlusion present	↑ if arterial and venous occlusion present and O_2Hb to HHb conversion
Adipose compression	↑ if adipose thins and a greater proportion of photons are absorbed in muscle ↓ or ↑ if adipose compression is associated with increased scattering	↑ if adipose thins and a greater proportion of photons are absorbed in muscle ↓ or ↑ if adipose compression is associated with increased scattering	↑ if adipose thins and a greater proportion of photons are absorbed in muscle ↓ or ↑ if adipose compression is associated with increased scattering
Skin compression	↓ if skin thins and a smaller proportion of photons are absorbed in skin	↓ if skin thins and a smaller proportion of photons are absorbed in skin	↓ if skin thins and a smaller proportion of photons are absorbed in skin
Increased μ_s'	↓ or ↑	↓ or ↑	↓ or ↑
Decreased μ_a	↓	↓	↓
Improved optical coupling	↓	↓	↓

Vascular occlusion alone does not explain trends with decreasing HHb and some other potential mechanisms likely contribute to the measured response. For instance, improved optical coupling could increase the intensity of re-emitted photons, which could be associated with smaller values of computed Hb values. Given the

configuration of the OxiTor, wherein the emitters and detectors project out from the body of the device, I expect that low loads are sufficient to ensure adequate coupling and elevated contact forces would have a minimal coupling effect. Similarly, decreased aggregate μ_a would be associated with lower values of computed Hb, though given the assumed chromophore absorption (i.e. Hb is the dominant source of absorption), any changes in aggregate μ_a are most likely related to blood volume changes associated with vascular occlusion as discussed above. The assumption that Hb is the main contributor to signal absorption should be somewhat robust to tissue compression, though an increased density of chromophores could result in greater signal attenuation.

Changes in μ_s' probably have a more prominent role in contact force artefact because scatterers are more prevalent than chromophores and scattering is the dominant factor[39] in diffuse reflectance NIRS. Tissue compression is thought to increase the density of scatterers[59], which would influence computed Hb values. Interestingly, my photon propagation simulation suggests adipose compression (without a corresponding change in μ_s') causes photons to propagate deeper into muscle and results in greater signal attenuation. Figure 19 shows how the normalized percent of re-emitted light is influenced by different STT. For clarity, the percent re-emitted photons is the number of photons re-emitted into the detector divided by the total number of photons emitted into the tissue. These values were normalized to the maximum percent of detected photons at each SDS to facilitate graphical comparison between each SDS. As demonstrated in Figure 19, more photon attenuation occurs at lower STT and this effect is exaggerated with longer SDS.

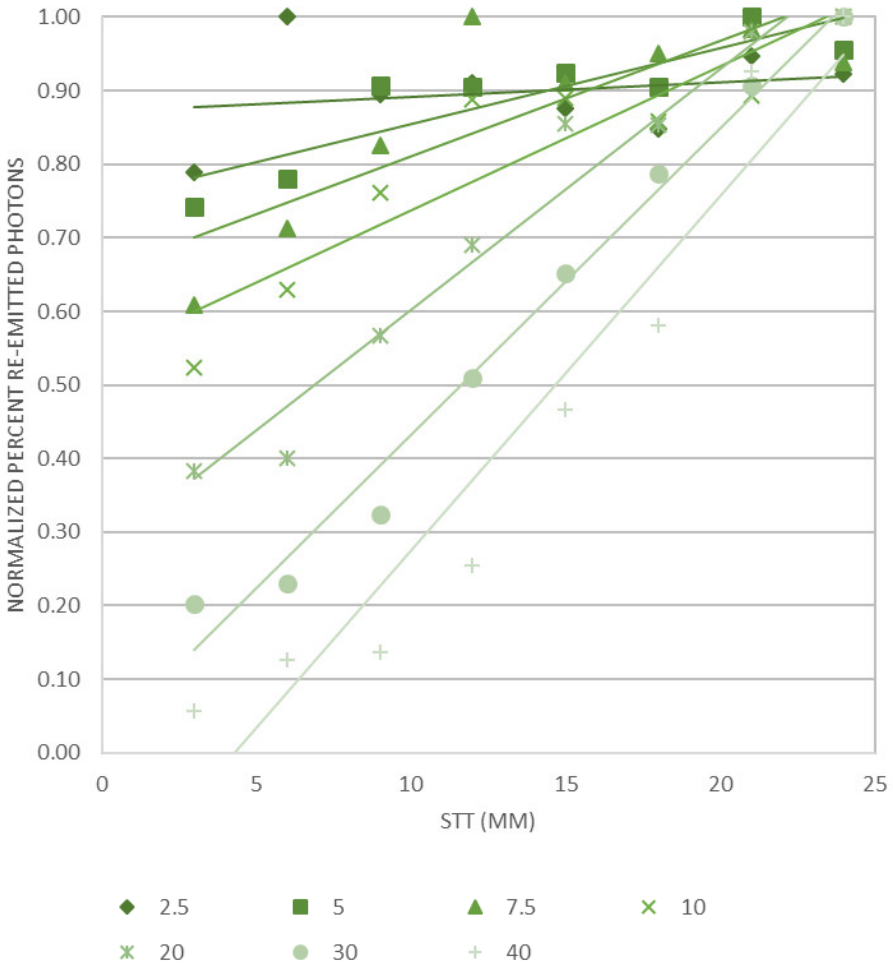

Figure 19: Normalized percent of re-emitted photons as a function of STT for different SDS. Percent re-emitted photons is the number of photons detected by the detector divided by the number to photons emitted into the tissue. The magnitude of these values varied more than an order of magnitude for each SDS, so they were normalized with respect to the maximum value at each SDS.

Figure 19 was created by varying the STT without concomitant changes in μ_s'. The role of μ_s' is less clear, though a general trend of lower detected intensity (lower computed tHb) with greater μ_s' is expected because more photons should undergo more scattering events. However, increased scattering could enhance detected

intensity for specific STT and SDS. Figure 20 demonstrates how the percent of re-emitted photons fluctuates around a general decreasing trend as μ_s' increases. Each data point was determined by simulating $180x10^6$ photons with an SDS of 20 mm and a STT of 6 mm. The fluctuations were evident after initial simulations using $20x10^6$ photons and continued to converge with more simulations, so I am confident that these fluctuations result from the interaction of SDS, STT and μ_s'. As evident in Figure 20, minor changes in μ_s' could result in either an increase or a decrease in re-emitted photons.

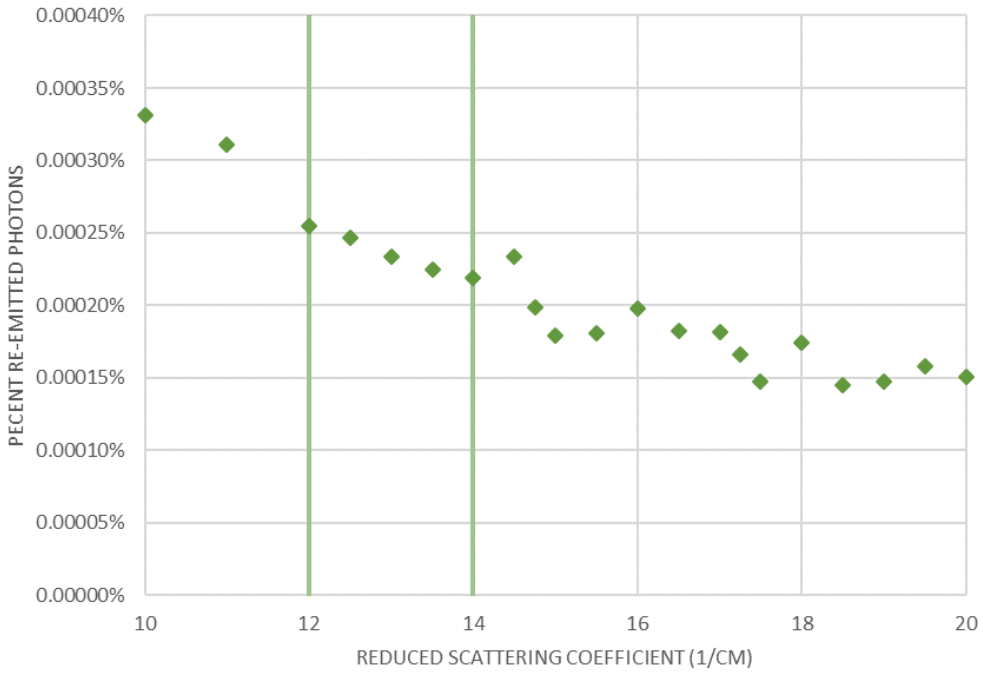

Figure 20: The percent of detected photons (similar to normalized detected light intensity) as a function of reduced scattering coefficient for an SDS of 20 mm and STT of 6 mm. Each data point was computed by simulating 180 million photons. The vertical lines identify the range of μ_s' used in the photon propagation study.

The effects of adipose compression on contact force artefact is not entirely clear. A compression of adipose tissue without changing μ_s' results in greater signal attenuation. In contrast, an increase in μ_s' (presumably caused by tissue compression) could either enhance or diminish signal attenuation. Both of these mechanisms may be present and their relative influence on contact force artefact is unknown. In addition, the data presented in Figure 20 is based on one SDS and one STT and the effects of these two variables are unknown.

Lastly, skin compression may contribute to contact force artefact, though not in a potentially contradictory manner as with adipose compression. Skin has a relatively high μ_a (closer to that of muscle than to that of adipose) and a relatively small thickness (compared to adipose). My simulation results suggest that skin does not act as a photon conduit in the same way adipose tissue does (see Appendix for graphical summary). This behaviour most likely results from the superficial location and smaller thickness; therefore, potential increases in μ_s' caused by changes in scatterer density are negligible. However, decreased skin thickness results in lower photon absorption and less signal attenuation. For example, simulation results indicate a 50% reduction in skin thickness (from 2 mm to 1 mm) results in a 45% increase in percent re-emitted photons at an SDS of 20 mm. This effect is expected to be less pronounced at longer SDS.

In summary, the mechanisms responsible for contact force artefact remain unclear, though the tissue response is governed by some interaction of a vascular

occlusion and superficial tissue compression. Future work is required to clarify the relative contributions of the above-noted mechanisms.

5.3.2 SIGNIFICANCE OF REASERCH: REDUCTION OF CONTACT FORCE ARTEFACT

My experimental results demonstrate that the magnitude of contact force artefact is large enough that it cannot be ignored. This is particularly important when measuring from muscle while contraction intensity is low and contact force is high. Even at high contraction intensity (70%MVC) and moderate contact force (20 N), an error of roughly 25% can be introduced. Moderate contact forces are required to maintain optical coupling and device positioning during dynamic *in vivo* measurements. Initially, I intended to design a device that concurrently measures NIRS parameters and contact force, which could use the empirical relations determined in the static contact force artefact study to correct for applied forces (a working prototype was developed); however, given the small sample size for the empirical relations and the additional findings of the dynamic contact force artefact study, I decided to pursue another device focused on the influence of the superficial layers (see next section for a description).

Until a device that minimizes contact force artefact is developed, I suggest that future studies measure and record contact forces during measurements. This need not be real-time load cell data, but simply reporting approximate contact forces generated by the fixation method would be useful for standardizing data comparisons. In the short term, reporting contact force should be considered a requirement, much

like reporting STT. Most researchers report STT values for reference, though few[97] incorporate it into their calculations.

Ideally, if contact forces are maintained above 20 N (8.2 kPa) then the influence of small contact force fluctuations will be minimized; however, a 20 N contact load causes significant contact force artefact compared to lower contact forces. Hence, there is a need to report contact forces and maintain higher contact forces if real-time load data is not acquired.

The concept of maintaining a minimum contact force of 20 N during oscillating loading is different than the experimentally measured response to an oscillating contact force (page 35) that was acquired with a minimum of 2 N. By maintaining a minimum contact force of 20 N during cyclic loading, the loading profile would be more similar to a static load with a small cyclic component superimposed on the loading profile. In fact, the experimental oscillating contact force data offers little insight into this potential method to minimise contact force artefact. A future study where small cyclic fluctuations are superimposed on a static load would be very insightful to the potential effects of this proposed method.

Maintaining contact loads above 20 N is a simple method to minimize contact force artefact, and, therefore, may be desirable for NIRS researchers, but it may not be ideal. Higher levels of contact force may cause participant discomfort during longer tests and could possibly lead to ischemic injury to the tissue in proximity to the NIRS device. Ideally, if contact force artefact is fully understood, it could be eliminated from NIRS data while maintaining lower, more comfortable, contact forces.

5.3.3 FUTURE DIRECTIONS: LONG TERM REDUCTION OF CONTACT FORCE ARTEFACT

The ultimate goal of my research is to understand contact force artefact and design a device that minimizes its effects. My current work quantified some aspects of contact force artefact, though the mechanisms responsible for this artefact remain speculative. Before a device can be designed that minimizes contact force artefact, these mechanisms must be understood.

Experimental evidence suggests that both skin and subcutaneous adipose tissue may play an important role in contact force artefact. Namely, muscle contraction intensity does not affect the trends of contact force effects, and Hb patterns recorded during cyclic loading are not entirely consistent with vascular occlusion. A major limitation of my current work is that STT measurements were made with inexpensive calipers. At the time of the experimental design, I did not appreciate the potential importance of STT on contact force effects. STT measurements were intended for reference and the accuracy of the caliper measurements are not reliable enough for a detailed analysis.

Future studies will be focused on determining the mechanisms responsible for contact force artefact, with specific focus on the influence of vascular occlusion and compression of superficial tissues. These studies will be used to inform the design process for a better NIRS device. Some potential investigations include the following.

1. *Investigate vascular occlusion and superficial tissue compression*: Novel ultrasound computational techniques[98], when combined with contrast

enhancing microbubbles, can create detailed images of microvasculature in rabbit skeletal muscle. This super-resolution ultrasound technique could be used to image tissue under varied contact loads to determine the contributions of vascular occlusion and quantify STT changes under load. If super-resolution ultrasound is recorded in conjunction with NIRS, the results would help clarify the effects of vascular occlusion during elevated contact forces.

2. *Determine the influence of compression on scattering coefficients*: Increased scatterer density has been suggested as a possible mechanism for NIRS contact force artefacts in various tissues[59,69], though this has not been formally documented with experimentation. In a muscle propagation simulation, Sayli *et al*[34] acknowledge that results are sensitive to optical inputs. Ideally, isolated *in vitro* specimens could be used to measure μ_s' and μ_a in adipose and skin under varied compressive forces to help refine estimates.
3. *Simulate interactions among μ_s', SDS and STT on percent re-emitted photons and Hb concentrations*: Data fluctuations presented in Figure 20 suggest that tissue geometry, optical properties and device size may influence signal attenuation. The fluctuations observed in the data should be investigated further.

Future research will help guide the development of novel NIRS devices that will minimize contact force artefact. Given the current findings, I suggest that a device capable of measuring STT in real time would be beneficial. Two potential systems are

(i) a time-domain system capable of measuring backscattering, and (ii) a multimodal system that incorporates ultrasound. Time-domain systems that measure STT have been implemented[33,37], though correlations between ultrasound (gold standard) and NIRS appear to be non-linear[33]. Despite this challenge, there is potential for a time-domain system to compensate for STT if it incorporates previous work based on CW-NIRS[96] where detected intensity is used to compensate for varied STT. Unfortunately, this CW technique is only applicable to occluded muscles in a resting state and it has no way to compensate for varied vascular perfusion based on contact forces. Instead, a multimodal device might be better suited to refining NIRS measurements because the device would combine the structural imaging of ultrasound combined with NIRS-derived Hb data. Multimodal systems are an area of current development. For example, a refined multimodal system has been created to detect lipid rich plaques during intravascular ultrasound[99] and systems have been designed to help detect breast cancer[100,101]. Theoretically, either time-domain NIRS or a multimodal system could be used to help minimise contact force artefact with the aid of real-time STT measurement combined with superficial filtering, but the multimodal device would have the added functionality of imaging microvascular occlusion during NIRS measurements. The extra structural imaging of ultrasound would help to quantify the effects of vascular occlusion during NIRS measurements. The ultimate goal for the novel NIRS device is to minimize all measurement artefacts, not just those related to contact force, so a multimodal approach might be the best solution.

5.4 CONCLUSION

The current work has provided novel information about contact force artefact in NIRS measurements. Perhaps the most salient finding of this work is the demonstration that contact force artefact can contribute to a significant portion of the measured signal and should not be ignored. Clearly, more investigations are required to understand the mechanisms responsible for this artefact before its effects can be removed from measurements. However, the current work provides insights to help steer future investigations in productive directions by quantifying the effects of contact force in transcutaneous NIRS muscle measurements.

REFERENCES

1. Gueverra R, Stothers L, Macnab A. Algorithm construction methodology for diagnostic classification of near-infrared spectroscopy data. *Spectrcoscopy* 2011; **25**: 1-11.

2. Macnab A, Shadgan B. Biomedical applications of wireless continuous wave near infrared spectroscopy. *Biomedical Spectroscopy and Imaging* 2012; **1**: 205-22.

3. Stothers L, Shadgan B, Macnab A. Urological applications of near infrared spectroscopy. *The Canadian Journal of Urology* 2008; **15**(6): 4399-409.

4. Jobsis FF. Noninvasive, infrared monitoring of cerebral and myocardial oxygen sufficiency and circulatory parameters. *Science (New York, NY)* 1977; **198**(4323): 1264-7.

5. Elwell CE, Cooper CE. Making light work: illuminating the future of biomedical optics. *Philosophical Transactions of the Royal Society of London A* 2011; **369**(1955): 4358-79.

6. Cui W, Kumar C, Chance B. Experimental study of migration depth for the photons measured at sample surface. Proceedings of SPIE: Time-Resolved Spectroscopy and Imaging of Tissues; 1991; 1991. p. 180-91.

7. Duncan A, Meek JH, Clemence M, et al. Measurement of cranial optical path length as a function of age using phase resolved near infrared spectroscopy. *Pediatric Research* 1996; **39**(5): 889-94.

8. Duncan A, Meek JH, Clemence M, et al. Optical pathlength measurements on adult head, calf and forearm and the head of the newborn infant using phase resolved optical spectroscopy. *Physics in Medicine & Biology* 1995; **40**(2): 295-304.

9. Strangman G, Franceschini MA, Boas DA. Factors affecting the accuracy of near-infrared spectroscopy concentration calculations for focal changes in oxygenation parameters. *NeuroImage* 2003; **18**(4): 865-79.

10. Patil AV, Safaie J, Moghaddam HA, Wallois F, Grebe R. Experimental investigation of NIRS spatial sensitivity. *Biomedical Optics Express* 2011; **2**(6): 1478-93.

11. Patterson MS, Andersson-Engels S, Wilson BC, Osei EK. Absorption spectroscopy in tissue-simulating materials: a theoretical and experimental study of photon paths. *Applied Optics* 1995; **34**(1): 22-30.

12. Mansouri C, L'Huillier J P, Kashou NH, Humeau A. Depth sensitivity analysis of functional near-infrared spectroscopy measurement using three-dimensional Monte Carlo modelling-based magnetic resonance imaging. *Lasers in Medical Science* 2010; **25**(3): 431-8.

13. Faris F, Thorniley M, Wickramasinghe Y, et al. Non-invasive in vivo near-infrared optical measurement of the penetration depth in the neonatal head. *Clinical Physics and Physiological Measurement* 1991; **12**(4): 353-8.

14. Boas D, Culver J, Stott J, Dunn A. Three dimensional Monte Carlo code for photon migration through complex heterogeneous media including the adult human head. *Optics Express* 2002; **10**(3): 159-70.

15. Chuang CC, Lee YT, Chen CM, Hsieh YS, Liu TC, Sun CW. Patient-oriented simulation based on Monte Carlo algorithm by using MRI data. *Biomedical Engineering Online* 2012; **11**: 21.

16. Zhang Q, Brown EN, Strangman GE. Adaptive filtering for global interference cancellation and real-time recovery of evoked brain activity: a Monte Carlo simulation study. *Journal of Biomedical Optics* 2007; **12**(4): 044014--12.

17. Lee CK, Sun CW, Lee PL, et al. Study of photon migration with various source-detector separations in near-infrared spectroscopic brain imaging based on three-dimensional Monte Carlo modeling. *Optics Express* 2005; **13**(21): 8339-48.

18. Matsushita K, Homma S, Okada E. Influence of adipose tissue on muscle oxygenation measurement with an NIRS instrument. Proceedings of SPIE; 1998; 1998. p. 159-65.

19. Sandell JL, Zhu TC. A review of in-vivo optical properties of human tissues and its impact on PDT. *Journal of Biophotonics* 2011; **4**(11-12): 773-87.

20. Wang X. Estimation of effective scatterer size and number density in near-infrared tomography. Hanover, New Hampshire: Dartmouth College; 2007.

21. Matcher SJ, Elwell CE, Cooper CE, Cope M, Delpy DT. Performance comparison of several published tissue near-infrared spectroscopy algorithms. *Analytical Biochemistry* 1995; **227**(1): 54-68.

22. Mancini DM, Bolinger L, Li H, Kendrick K, Chance B, Wilson JR. Validation of near-infrared spectroscopy in humans. *Journal of applied physiology (Bethesda, Md : 1985)* 1994; **77**(6): 2740-7.

23. Davis ML, Barstow TJ. Estimated contribution of hemoglobin and myoglobin to near infrared spectroscopy. *Respiratory Physiology & Neurobiology* 2013; **186**(2): 180-7.

24. Boushel R, Langberg H, Olesen J, Gonzales-Alonzo J, Bulow J, Kjaer M. Monitoring tissue oxygen availability with near infrared spectroscopy (NIRS) in health and disease. *Scandinavian Journal of Medicine & Science in Sports* 2001; **11**(4): 213-22.

25. Hueber DM, Fantini S, Cerussi AE, Barbieri BB. New optical probe designs for absolute (self-calibrating) NIR tissue hemoglobin measurements. Proceedings of SPIE: Optical Tomography and Spectroscopy of Tissue III; 1999; 1999. p. 618-31.

26. Cope M, Delpy DT. System for long-term measurement of cerebral blood and tissue oxygenation on newborn infants by near infra-red transillumination. *Medical & Biological Engineering & Computing* 1988; **26**(3): 289-94.

27. Piantadosi CA, Hall M, Comfort BJ. Algorithms for in vivo near infrared spectroscopy. *Analytical Biochemistry* 1997; **253**: 277-9.

28. Doornbos RMP, Lang R, Aalders MC, Cross FW, Sterenborg HJCM. The determination of in vivo human tissue optical properties and absolute chromophore concentrations using spatially resolved steady-state diffuse reflectance spectroscopy. *Physics in medicine and biology* 1999; **44**(4): 967.

29. Cooper CE, Springett R. Measurement of cytochrome oxidase and mitochondrial energetics by near-infrared spectroscopy. *Philosophical Transactions of the Royal Society B: Biological Sciences* 1997; **352**(1354): 669-76.

30. van Beekvelt MC, Borghuis MS, van Engelen BG, Wevers RA, Colier WN. Adipose tissue thickness affects in vivo quantitative near-IR spectroscopy in human skeletal muscle. *Clinical Science* 2001; **101**(1): 21-8.

31. Krssak M, Falk Petersen K, Dresner A, et al. Intramyocellular lipid concentrations are correlated with insulin sensitivity in humans: a 1H NMR spectroscopy study. *Diabetologia* 1999; **42**(1): 113-6.

32. Zhou D, Guo Z. Intramyocellular Lipids Versus Intramyocellular Triglycerides. *Magnetic Resonance in Medicine* 2012; **67**(2): 297-9.

33. Geraskin D, Boeth H, Kohl-Bareis M. Optical measurement of adipose tissue thickness and comparison with ultrasound, magnetic resonance imging, and callipers. *Journal of Biomedical Optics* 2009; **14**(4): 044017.

34. Sayli Ö, Aksel E, Akin A. Crosstalk and error analysis of fat layer on continuous wave near-infrared spectroscopy measurements. *Journal of Biomedical Optics* 2008; **13**(6): 064019.

35. Niwayama M, Lin L, Shao J, Kudo N, Yamamoto K. Quantitative measurement of muscle hemoglobin oxygenation using near-infrared spectroscopy with correction for the influence of a subcutaneous fat layer. *Review of Scientific Instruments* 2000; **71**(12): 4571-5.

36. Ohmae E, Nishio S, Oda M, et al. Sensitivity correction for the influence of the fat layer on muscle oxygenation and estimation of fat thickness by time-resolved spectroscopy. *Journal of Biomedical Optics* 2014; **19**(6): 067005.

37. Cooper CE, Penfold SM, Elwell CE, Angus C. Comparison of local adipose tissue content and SRS-derived NIRS muscle oxygenation measurements in 90 individuals. *Advances in Experimental Medicine and Biology* 2010; **662**: 177-81.

38. Hamaoka T, McCully KK, Niwayama M, Chance B. The use of muscle near-infrared spectroscopy in sport, health and medical sciences: recent developments. *Philosophical Transactions Series A: Mathematical, Physical and Engineering Sciences* 2011; **369**(1955): 4591-604.

39. Pellicer A, Bravo Mdel C. Near-infrared spectroscopy: a methodology-focused review. *Seminars in Fetal & Neonatal Medicine* 2011; **16**(1): 42-9.

40. Torricelli A, Contini D, Pifferi A, et al. Time domain functional NIRS imaging for human brain mapping. *NeuroImage* 2014; **85 Pt 1**: 28-50.

41. Scholkmann F, Kleiser S, Metz AJ, et al. A review on continuous wave functional near-infrared spectroscopy and imaging instrumentation and methodology. *NeuroImage* 2014; **85 Pt 1**: 6-27.

42. Gagnon L, Cooper RJ, Yücel MA, Perdue KL, Greve DN, Boas DA. Short separation channel location impacts the performance of short channel regression in NIRS. *NeuroImage* 2012; **59**(3): 2518-28.

43. Saager RB, Berger AJ. Direct characterization and removal of interfering absorption trends in two-layer turbid media. *Journal of the Optical Society of America A, Optics, Image Science, and Vision* 2005; **22**(9): 1874-82.

44. Saager RB, Telleri NL, Berger AJ. Two-detector Corrected Near Infrared Spectroscopy (C-NIRS) detects hemodynamic activation responses more robustly than single-detector NIRS. *NeuroImage* 2011; **55**(4): 1679-85.

45. Scarpa F, Brigadoi S, Cutini S, et al. A reference-channel based methodology to improve estimation of event-related hemodynamic response from fNIRS measurements. *NeuroImage* 2013; **72**: 106-19.

46. Fabbri F, Sassaroli A, Henry ME, Fantini S. Optical measurements of absorption changes in two-layered diffusive media. *Physics in Medicine and Biology* 2004; **49**(7): 1183-201.

47. Zhang Q, Brown EN, Strangman GE. Adaptive filtering to reduce global interference in evoked brain activity detection: a human subject case study. *Journal of Biomedical Optics* 2007; **12**(6): 064009.

48. Zhang Q, Strangman GE, Ganis G. Adaptive filtering to reduce global interference in non-invasive NIRS measures of brain activation: how well and when does it work? *NeuroImage* 2009; **45**(3): 788-94.

49. Takahashi T, Takikawa Y, Kawagoe R, Shibuya S, Iwano T, Kitazawa S. Influence of skin blood flow on near-infrared spectroscopy signals measured on the forehead during a verbal fluency task. *NeuroImage* 2011; **57**(3): 991-1002.

50. Tew GA, Ruddock AD, Saxton JM. Skin blood flow differentially affects near-infrared spectroscopy-derived measures of muscle oxygen saturation and blood volume at rest and during dynamic leg exercise. *European Journal of Applied Physiology* 2010; **110**(5): 1083-9.

51. Finocchietti S, Takahashi K, Okada K, Watanabe Y, Graven-Nielsen T, Mizumura K. Deformation and pressure propagation in deep tissue during mechanical painful pressure stimulation. *Medical & Biological Engineering & Computing* 2013; **51**(1-2): 113-22.

52. Felici F, Quaresima V, Fattorini L, Sbriccoli P, Filligoi GC, Ferrari M. Biceps brachii myoelectric and oxygenation changes during static and sinusoidal isometric exercises. *Journal of Electromyography and Kinesiology* 2009; **19**(2): e1-11.

53. Kell RT, Farag M, Bhambhani Y. Reliability of erector spinae oxygenation and blood volume responses using near-infrared spectroscopy in healthy males. *European Journal of Applied Physiology* 2004; **91**(5-6): 499-507.

54. Noponen TE, Kotilahti K, Nissila I, Kajava T, Merilainen PT. Effects of improper source coupling in frequency-domain near-infrared spectroscopy. *Physics in Medicine and Biology* 2010; **55**(10): 2941-60.

55. Davis J, Kaufman KR, Lieber RL. Correlation between active and passive isometric force and intramuscular pressure in the isolated rabbit tibialis anterior muscle. *Journal of Biomechanics* 2003; **36**(4): 505-12.

56. Thornton GM, Schwab TD, Oxland TR. Fatigue is more damaging than creep in ligament revealed by modulus reduction and residual strength. *Annals of Biomedical Engineering* 2007; **35**(10): 1713-21.

57. Matcher SJ, Cope M, Delpy DT. Use of the water absorption spectrum to quantify tissue chromophore concentration changes in near-infrared spectroscopy. *Physics in Medicine and Biology* 1994; **39**(1): 177-96.

58. Ti Y, Lin WC. Effects of probe contact pressure on in vivo optical spectroscopy. *Optics Express* 2008; **16**(6): 4250-62.

59. Reif R, Amorosino MS, Calabro KW, A'Amar O, Singh SK, Bigio IJ. Analysis of changes in reflectance measurements on biological tissues subjected to different probe pressures. *Journal of Biomedical Optics* 2008; **13**(1): 010502.

60. Carp SA, Kauffman T, Fang Q, et al. Compression-induced changes in the physiological state of the breast as observed through frequency domain photon migration measurements. *Journal of Biomedical Optics* 2006; **11**(6): 064016.

61. Lim L, Nichols B, Rajaram N, Tunnell JW. Probe pressure effects on human skin diffuse reflectance and fluorescence spectroscopy measurements. *Journal of Biomedical Optics* 2011; **16**(1): 011012.

62. Delgado Atencio JA, Orozco Guillén EE, Vázquez y Montiel S, et al. Influence of probe pressure on human skin diffuse reflectance spectroscopy measurements. *Optical Memory and Neural Networks* 2009; **18**(1): 6-14.

63. Willemse J. The mechanism of tissue optical properties change induced by tissue deformation: Academisch Medisch Centrum; 2016.

64. Cugmas B, Bregar M, Burmen M, Pernus F, Likar B. Impact of contact pressure-induced spectral changes on soft-tissue classification in diffuse reflectance spectroscopy: problems and solutions. *Journal of Biomedical Optics* 2014; **19**(3): 37002.

65. Chan EK, Sorg B, Protsenko D, O'Neil M, Motamedi M, Welch AJ. Effects of compression on soft tissue optical properties. *IEEE Journal of Selected Topics in Quantum Electronics* 1996; **2**(4): 943-50.

66. Vogt WC, Izquierdo-Roman A, Nichols B, Lim L, Tunnell JW, Rylander CG. Effects of mechanical indentation on diffuse reflectance spectra, light transmission, and intrinsic optical properties in ex vivo porcine skin. *Lasers in Surgery and Medicine* 2012; **44**(4): 303-9.

67. Bregar M, Bürmen M, Aljančič U, Cugmas B, Pernuš F, Likar B. Contact pressure–aided spectroscopy. *Journal of Biomedical Optics* 2014; **19**(2): 020501-.

68. Cugmas B, Bürmen M, Bregar M, Pernuš F, Likar B. Pressure-induced near infrared spectra response as a valuable source of information for soft tissue classification. *Journal of Biomedical Optics* 2013; **18**(4): 047002-.

69. Cheng X, Xu X. Study of the pressure effect in near-infrared spectroscopy. *Biomedical Optics* 2003; **4955**: 397-406.

70. Finocchietti S, Morch CD, Arendt-Nielsen L, Graven-Nielsen T. Effects of adipose thickness and muscle hardness on pressure pain sensitivity. *The Clinical Journal of Pain* 2011; **27**(5): 414-24.

71. Geerligs M, Peters G, Ackermans P, Oomens C, Baaijens F. Linear viscoelastic behavior of subcutaneous adipose tissue. *Biorheology* 2008; **45**: 677-88.

72. Chen W, Liu R, Xu K, Wang RK. Influence of contact state on NIR diffuse reflectance spectroscopy in vivo. *Journal of Physics D: Applied Physics* 2005; **38**(15): 2691.

73. Carp SA, Selb J, Fang Q, et al. Dynamic functional and mechanical response of breast tissue to compression. *Optics Express* 2008; **16**(20): 16064-78.

74. Shadgan B, Reid WD, Harris RL, Jafari S, Powers SK, O'Brien PJ. Hemodynamic and oxidative mechanisms of tourniquet-induced muscle injury: near-infrared spectroscopy for the orthopedics setting. *Journal of Biomedical Optics* 2012; **17**(8): 081408-1.

75. Toomey C, McCreesh K, Leahy S, Jakeman P. Technical considerations for accurate measurement of subcutaneous adipose tissue thickness using B-mode ultrasound. *Ultrasound* 2011; **19**(2): 91-6.

76. Jacques SL. Optical properties of biological tissues: a review. *Physics in Medicine and Biology* 2013; **58**(11): R37-61.

77. Homma S, Fukunaga T, Kagaya A. Influence of adipose tissue thickness on near infrared spectroscopic signal in the measurement of human muscle. *Journal of Biomedical Optics* 1996; **1**(4): 418-24.

78. Bringard A, Denis R, Belluye N, Perrey S. Effects of compression tights on calf muscle oxygenation and venous pooling during quiet resting in supine and standing positions. *Journal of Sports Medicine and Physical Fitness* 2006; **46**(4): 548-54.

79. Holland K, Sechopoulos I, Mann RM, den Heeten GJ, van Gils CH, Karssemeijer N. Influence of breast compression pressure on the performance of population-based mammography screening. *Breast Cancer Research* 2017; **19**(1): 126.

80. Branderhorst W, de Groot JE, Highnam R, et al. Mammographic compression--a need for mechanical standardization. *European Journal of Radiology* 2015; **84**(4): 596-602.

81. Murray A, Marjanovic D. Optical assessment of recovery of tissue blood supply after removal of externally applied pressure. *Medical and Biological Engineering and Computing* 1997; **35**(4): 425-7.

82. Yamamoto K, Niwayama M, Lin L, Shiga T, Kudo N, Takahashi M. Near-infrared muscle oximeter that can correct the influence of a subcutaneous fat layer. *Proceddings of SPIE* 1998; **3257**: 146-55.

83. Yang Y, Soyemi O, Landry M, Soller B. Influence of a fat layer on the near infrared spectra of human muscle: quantitative analysis based on two-layered Monte Carlo simulations and phantom experiments. *Optics Express* 2005; **13**(5): 1570-9.

84. Okada E, Delpy DT. Near-infrared light propagation in an adult head model. II. Effect of superficial tissue thickness on the sensitivity of the near-infrared spectroscopy signal. *Applied Optics* 2003; **42**(16): 2915-22.

85. Wang L, Jacques SL, Zheng L. MCML—Monte Carlo modeling of light transport in multi-layered tissues. *Computer Methods and Programs in Biomedicine* 1995; **47**(2): 131-46.

86. Binzoni T, Leung TS, Gandjbakhche AH, Rüfenacht D, Delpy DT. The use of the Henyey-Greenstein phase function in Monte Carlo simulations in biomedical optics. *Physics in Medicine and Biology* 2006; **51**(17): N313-22.

87. Ding H, Lu JQ, Wooden WA, Kragel PJ, Hu XH. Refractive indices of human skin tissues at eight wavelengths and estimated dispersion relations between 300 and 1600 nm. *Physics in Medicine and Biology* 2006; **51**(6): 1479-89.

88. Bolin FP, Preuss LE, Taylor RC, Ference RJ. Refractive index of some mammalian tissues using a fiber optic cladding method. *Applied Optics* 1989; **28**(12): 2297-303.

89. Tearney GJ, Brezinski ME, Southern JF, Bouma BE, Hee MR, Fujimoto JG. Determination of the refractive index of highly scattering human tissue by optical coherence tomography. *Optics Letters* 1995; **20**(21): 2258.

90. Dirckx JJ, Kuypers LC, Decraemer WF. Refractive index of tissue measured with confocal microscopy. *Journal of Biomedical Optics* 2005; **10**(4): 44014.

91. Laurent A, Mistretta F, Bottigioli D, et al. Echographic measurement of skin thickness in adults by high frequency ultrasound to assess the appropriate microneedle length for intradermal delivery of vaccines. *Vaccine* 2007; **25**(34): 6423-30.

92. Shadgan B, Guenette JA, Sheel AW, Reid WD. Sternocleidomastoid muscle deoxygenation in response to incremental inspiratory threshold loading measured by near infrared spectroscopy. *Respiratory Physiology & Neurobiology* 2011; **178**(2): 202-9.

93. Leahy S, Toomey C, McCreesh K, O'Neill C, Jakeman P. Ultrasound Measurement of Subcutaneous Adipose Tissue Thickness Accurately Predicts Total and Segmental Body Fat of Young Adults. *Ultrasound in Medicine and Biology* 2012; **38**(1): 28-34.

94. Franceschini M, Fantini S, Paunescu A, Maier J, Gratton E. Influence of a superficial layer in the quantitative spectroscopic study of strongly scattering media. *Optical Society of America* 1998; **37**(31): 7447-58.

95. Hunter RJ, Patterson MS, Farrell TJ, Hayward JE. Haemoglobin oxygenation of a two-layer tissue-simulating phantom from time-resolved reflectance: effect of top layer thickness. *Physics in Medicine and Biology* 2002; **47**(2): 193-208.

96. Yamamoto K, Niwayama M, Lin L, Shiga T, Kudo N, Takahashi M. Accurate NIRS measurement of muscle oxygenation by correcting the influence of a subcutaneous fat layer. *Proceedings of SPIE* 1998; **3194**: 166-73.

97. Bowen TS, Rossiter HB, Benson AP, et al. Slowed oxygen uptake kinetics in hypoxia correlate with the transient peak and reduced spatial distribution of absolute skeletal muscle deoxygenation. *Experimental Physiology* 2013; **98**(11): 1585-96.

98. Zhang J, Li N, Dong F, et al. Ultrasound Microvascular Imaging Based on Super-Resolution Radial Fluctuations. *Journal of Ultrasound in Medicine* 2020; **39**(8).

99. Wilkinson SE, Madder RD. Intracoronary near-infrared spectroscopy—role and clinical applications. *Cardiovascular Diagnosis and Therapy* 2020.

100. Ewing J. Design and instrumentation of a multimodal imaging system for breast cancer detection. Columbus Ohio: Ohio State University; 2008.

101. Zimmermann BB, Deng B, Singh B, et al. Multimodal breast cancer imaging using coregistered dynamic diffuse optical tomography and digital breast tomosynthesis. *Journal of Biomedical Optics* 2017; **22**(4): 46008-1--10.

APPENDIX A

The following unlabelled figures depict data from all statics contact force trials. The figure titles indicate the measurement location, muscle contraction intensity and contact according to the following convention: Muscle-%MVC-Contact Force (for example, VL-70-20N is a measurement from vastus lateralis during a 70% MVC contraction with 20 N of contact force.

O_2Hb is red; HHb is blue; tHb is green. The black traces on the NIRS graphs indicate subjects with higher STT. The cut off for these “high” values was arbitrarily chosen, and they do not represent outlier cut offs. BB STT > 6 mm; ED STT > 3 mm; SCM STT > 3 mm; VL STT > 8 mm. The intention of the black traces was to explore the effects of STT on statics contact force artefact and no formal analysis was completed with these cut off values.

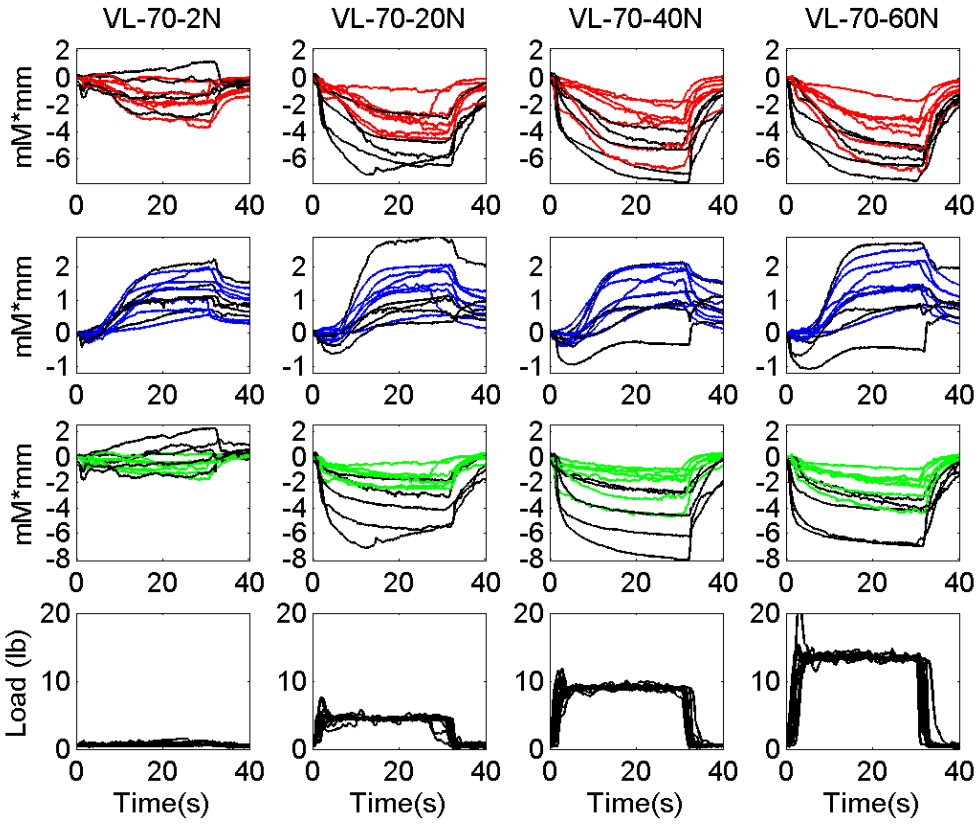
VL-70-2N
VL-70-20N
VL-70-40N
VL-70-60N
mM*mm
Load (lb)
Time(s)

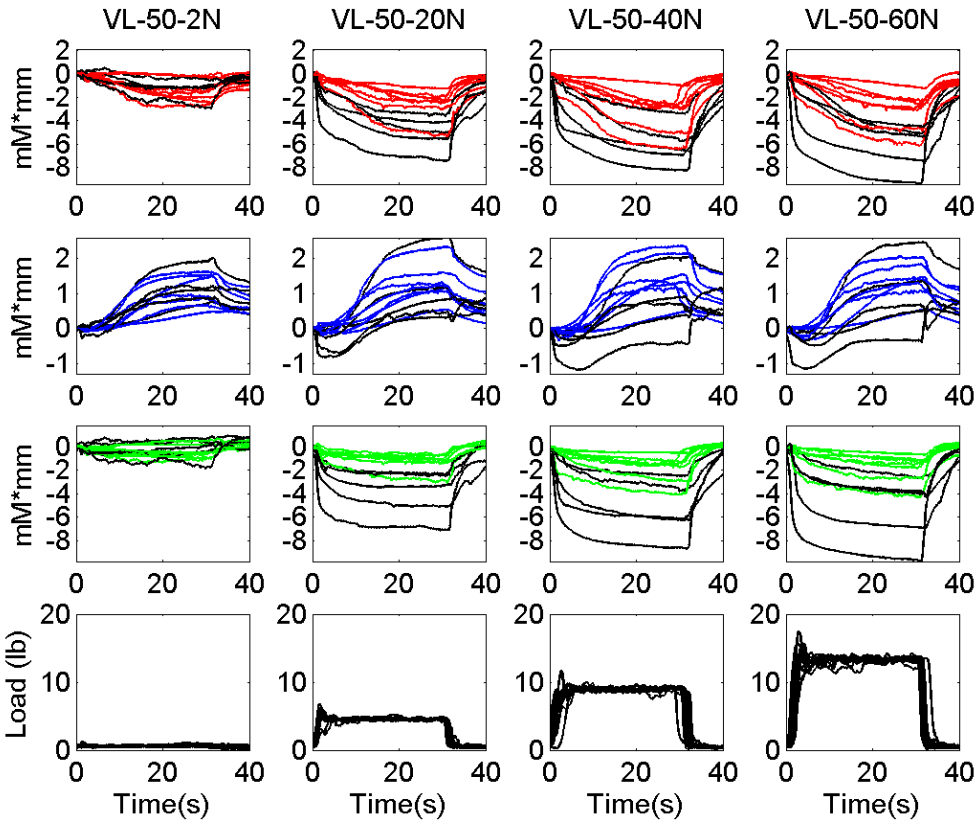
VL-50-2N
VL-50-20N
VL-50-40N
VL-50-60N
mM*mm
Load (lb)
Time(s)

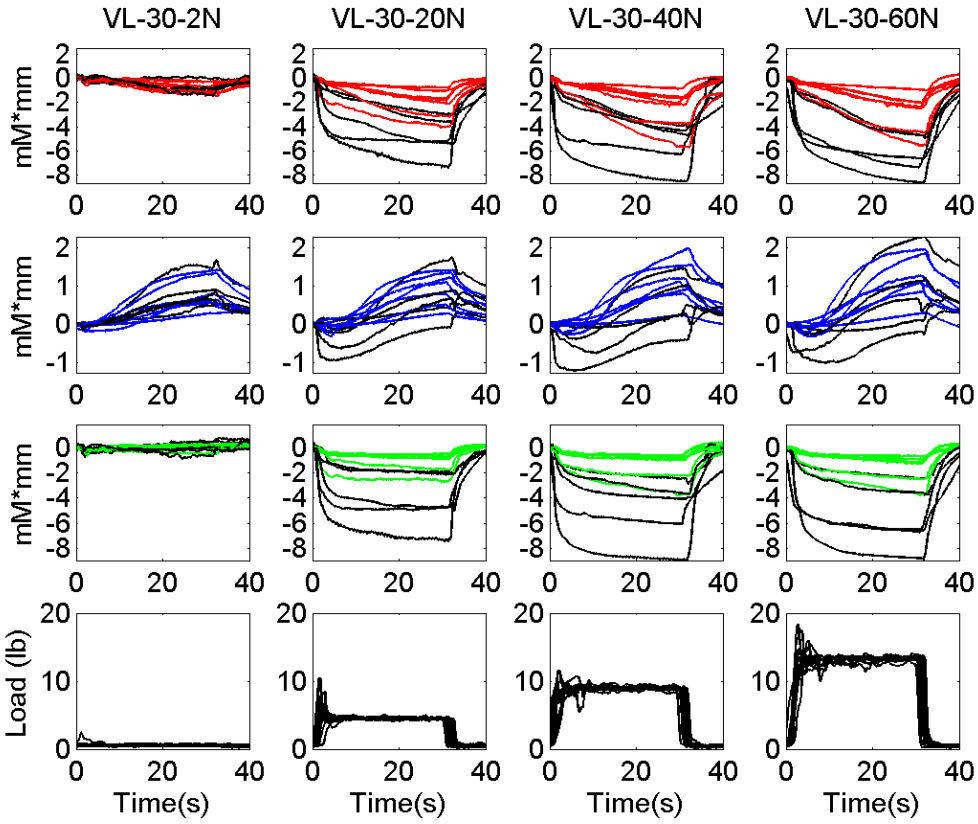
VL-30-2N
VL-30-20N
VL-30-40N
VL-30-60N
mM*mm
Load (lb)
Time(s)

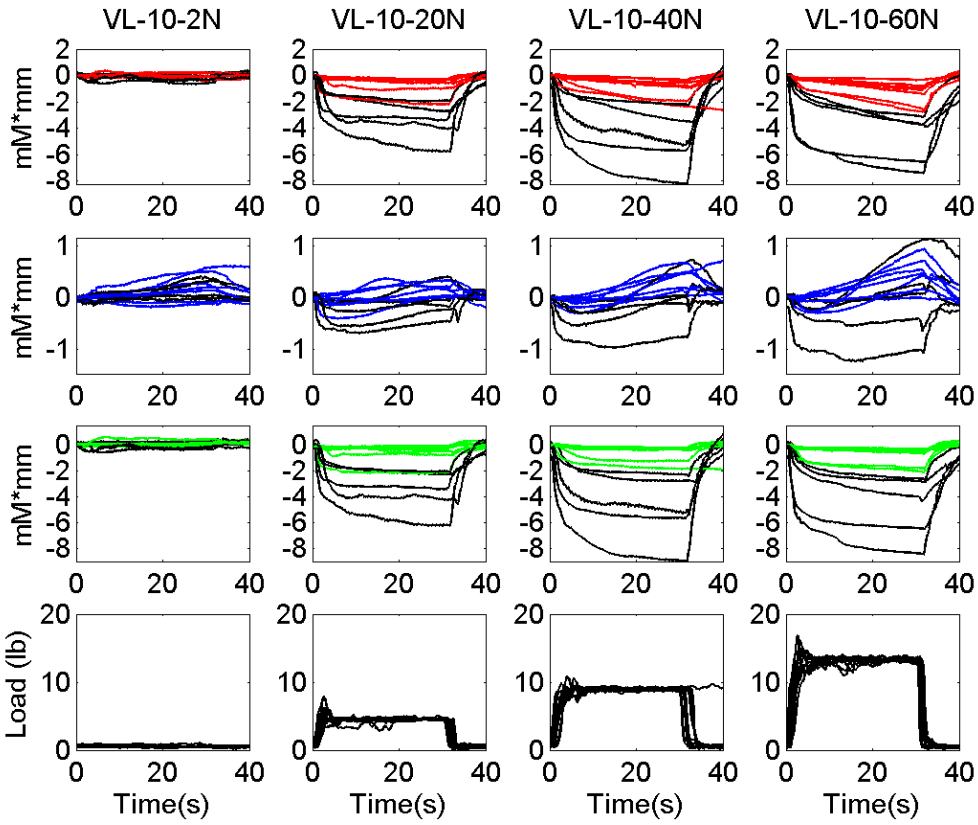
VL-10-2N
VL-10-20N
VL-10-40N
VL-10-60N
mM*mm
Load (lb)
Time(s)

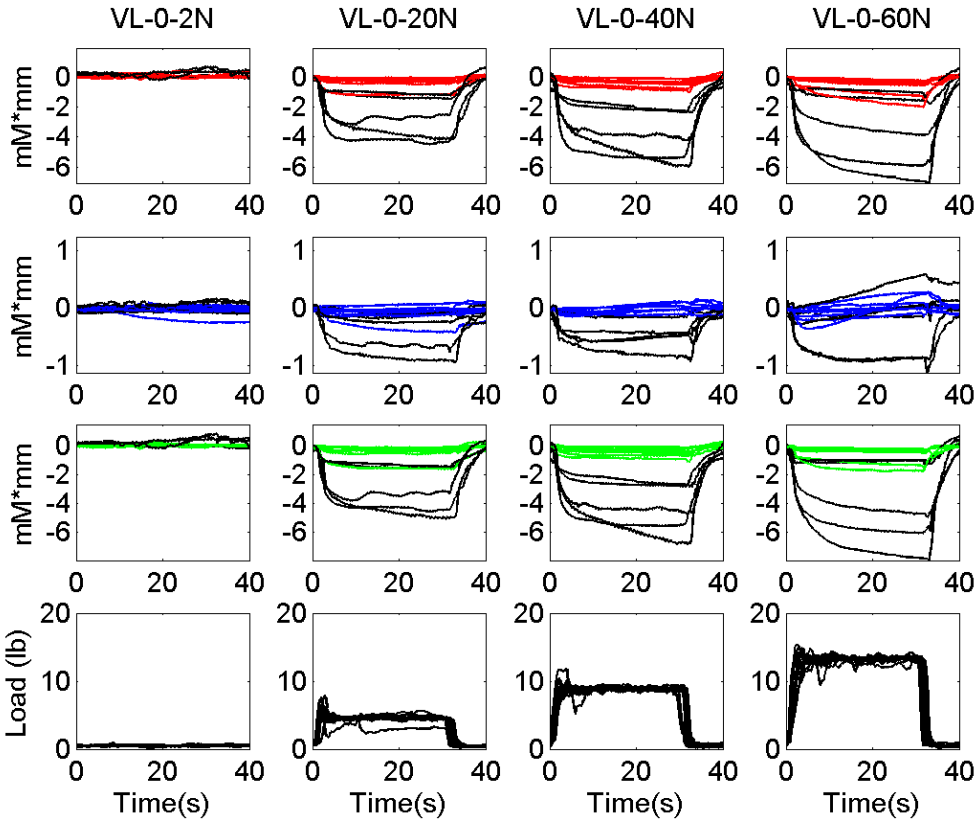
VL-0-2N
VL-0-20N
VL-0-40N
VL-0-60N
mM*mm
Load (lb)
Time(s)

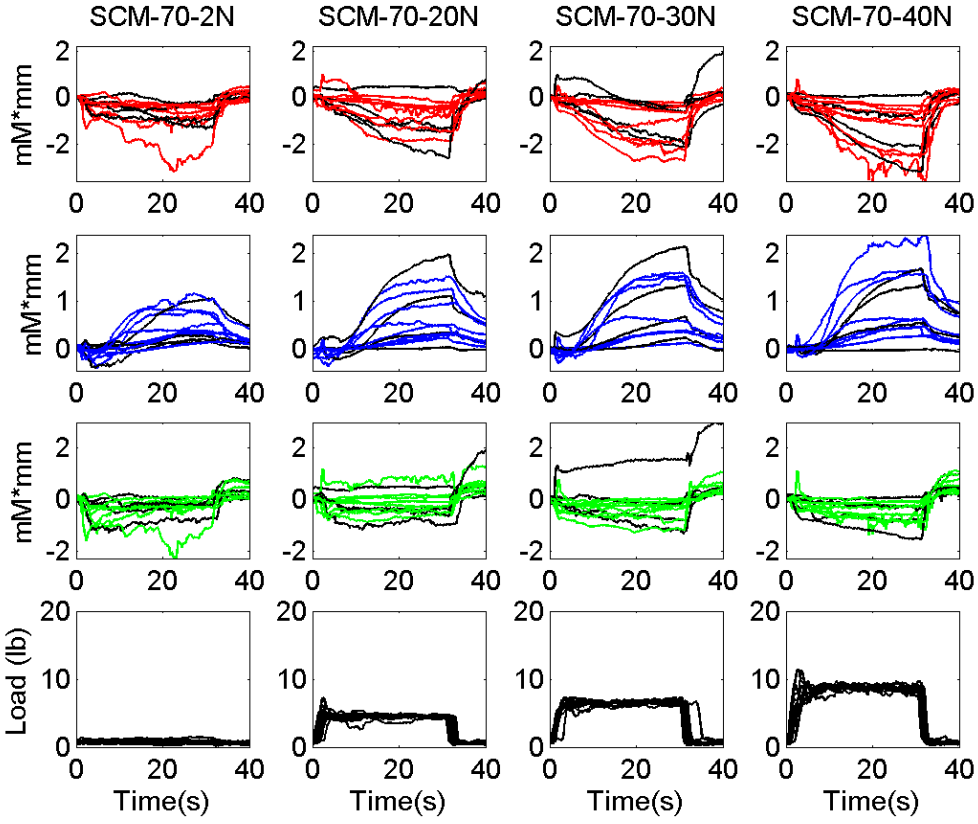
SCM-70-2N
SCM-70-20N
SCM-70-30N
SCM-70-40N
mM*mm
Load (lb)
Time(s)

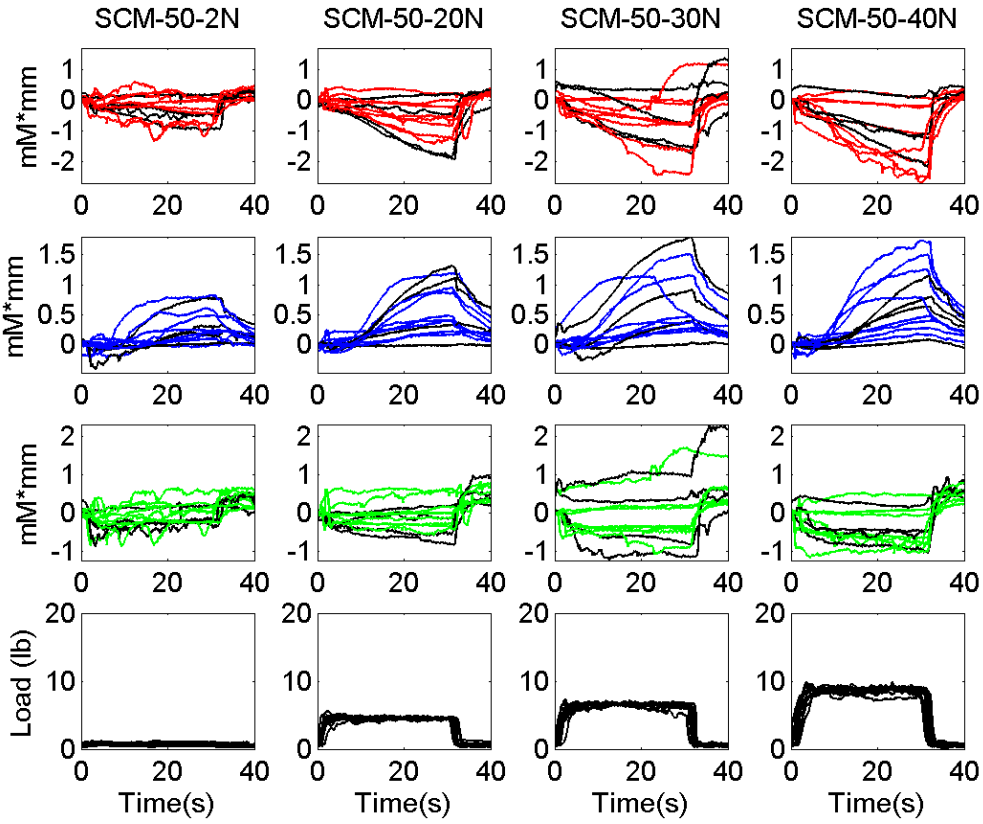
SCM-50-2N
SCM-50-20N
SCM-50-30N
SCM-50-40N
mM*mm
Load (lb)
Time(s)

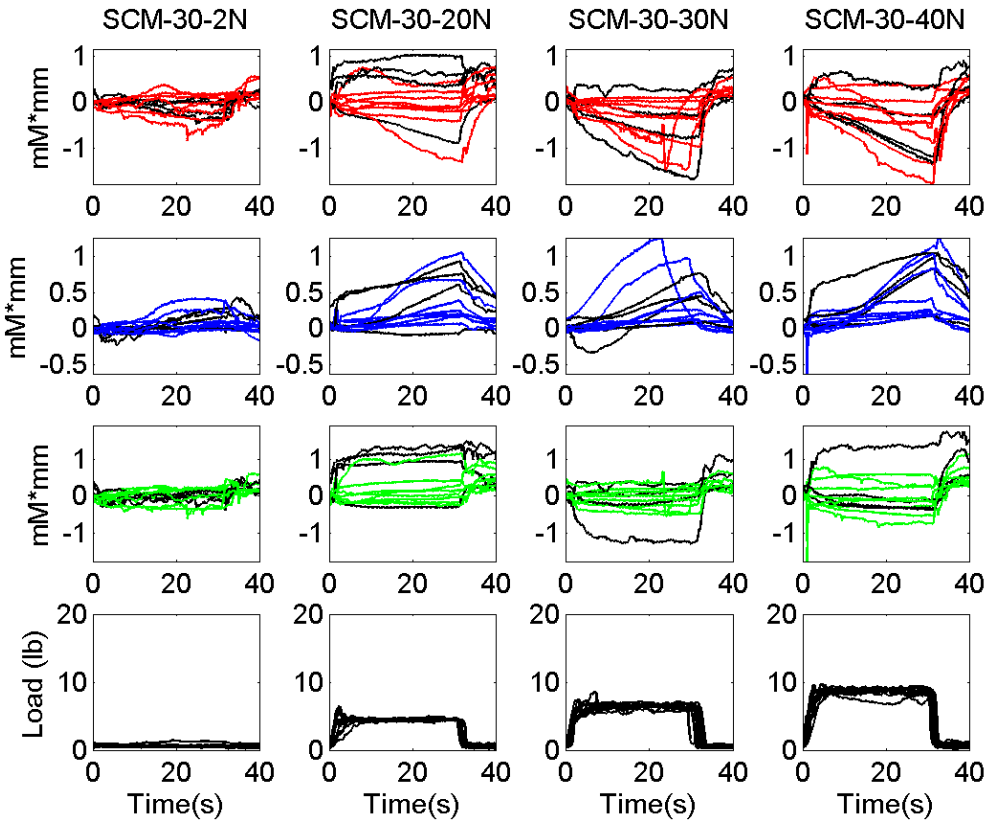
SCM-30-2N
SCM-30-20N
SCM-30-30N
SCM-30-40N
mM*mm
Load (lb)
Time(s)

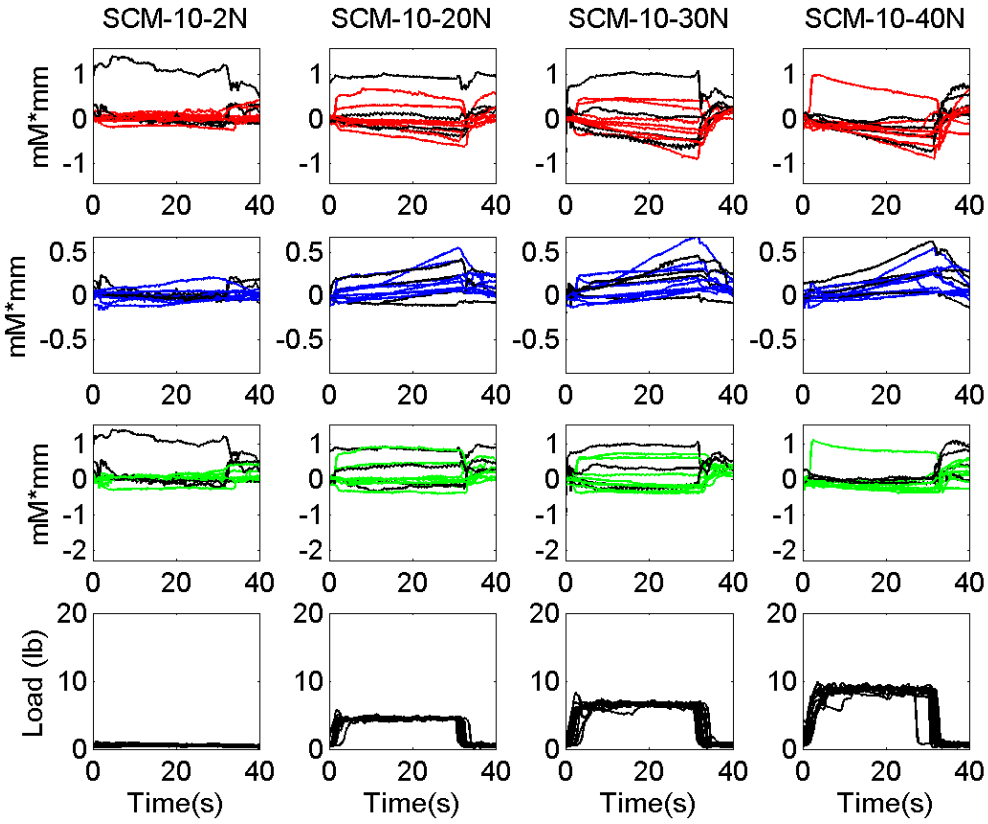
SCM-10-2N
SCM-10-20N
SCM-10-30N
SCM-10-40N
mM*mm
Load (lb)
Time(s)

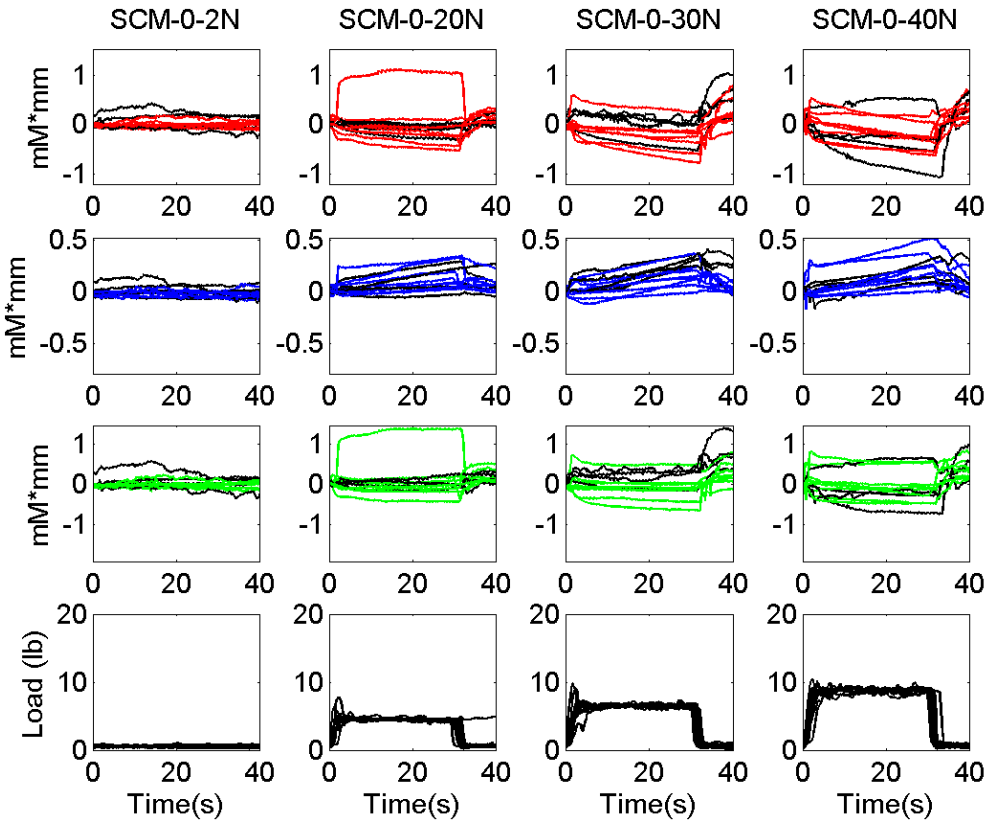
SCM-0-2N
SCM-0-20N
SCM-0-30N
SCM-0-40N
mM*mm
Load (lb)
Time(s)

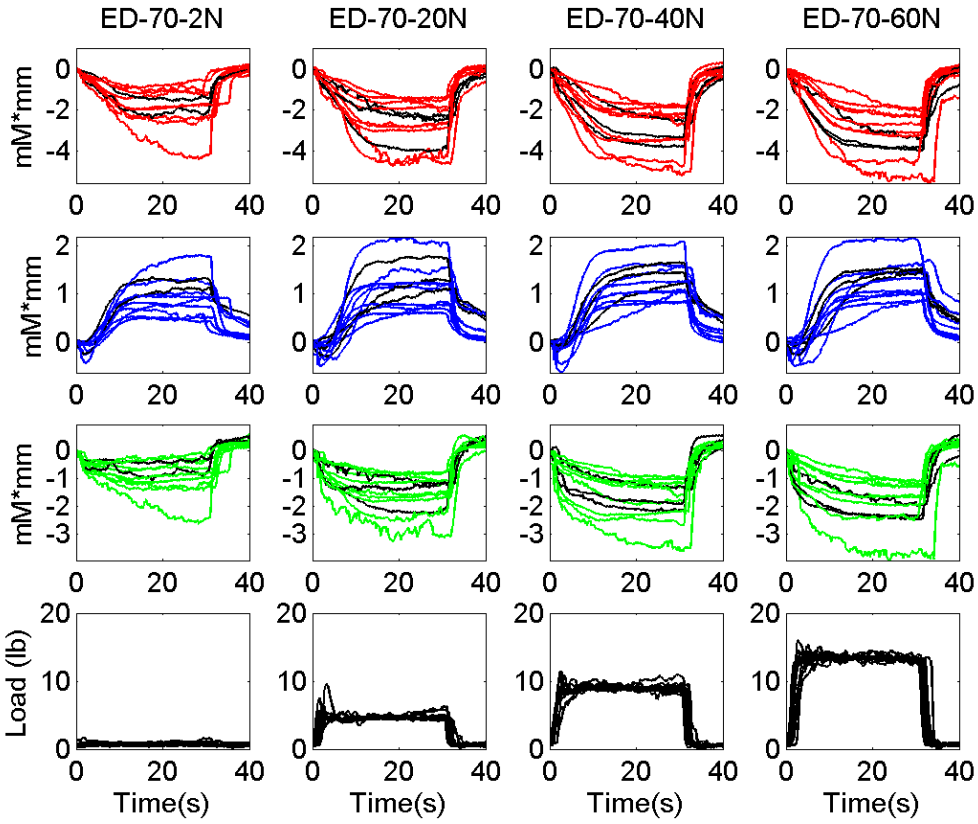
ED-70-2N
ED-70-20N
ED-70-40N
ED-70-60N
mM*mm
Load (lb)
Time(s)

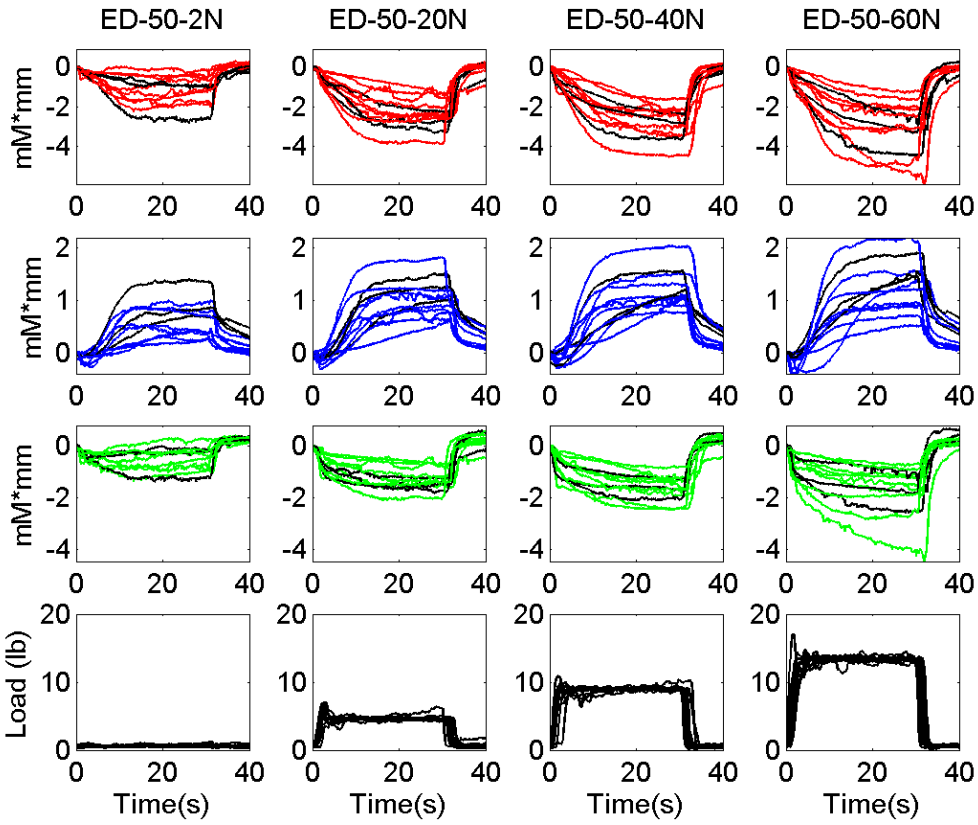
ED-50-2N
ED-50-20N
ED-50-40N
ED-50-60N
mM*mm
Load (lb)
Time(s)

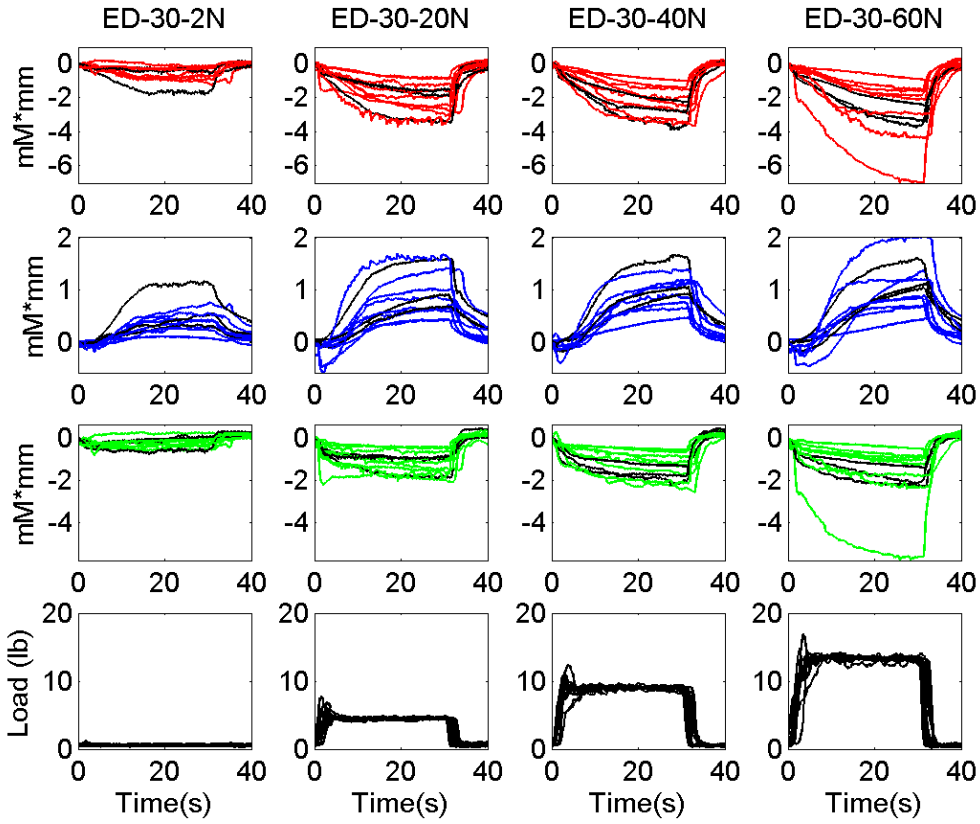
ED-30-2N
ED-30-20N
ED-30-40N
ED-30-60N
mM*mm
Load (lb)
Time(s)

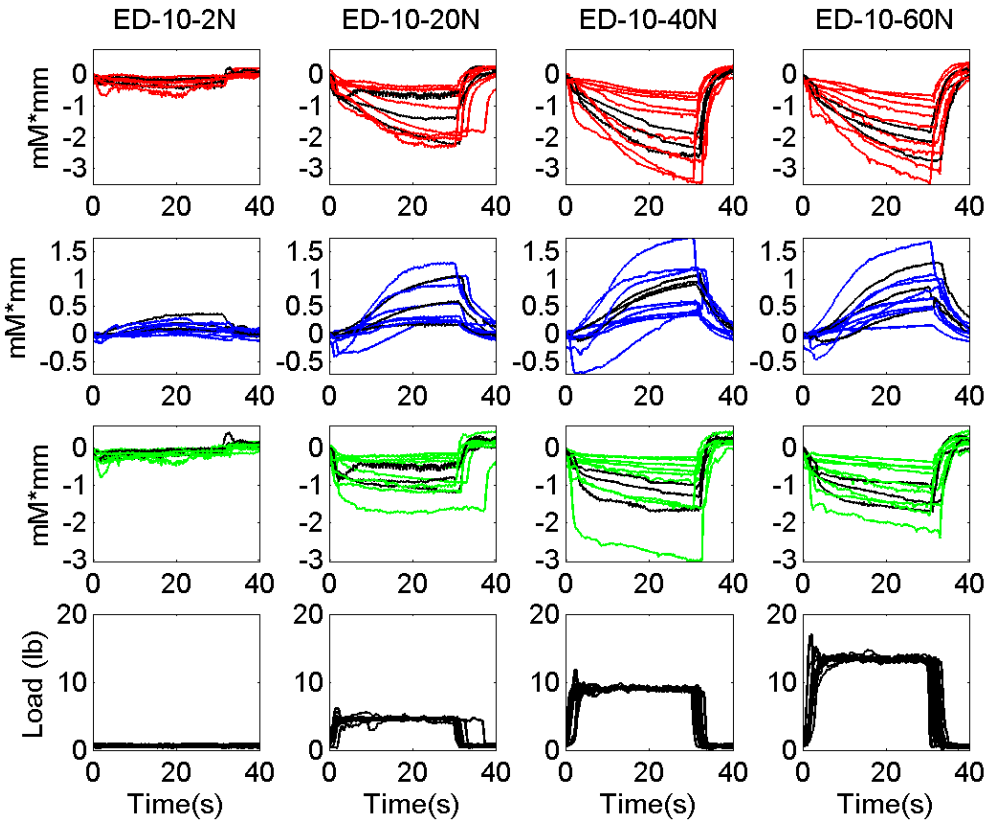
ED-10-2N
ED-10-20N
ED-10-40N
ED-10-60N
mM*mm
Load (lb)
Time(s)

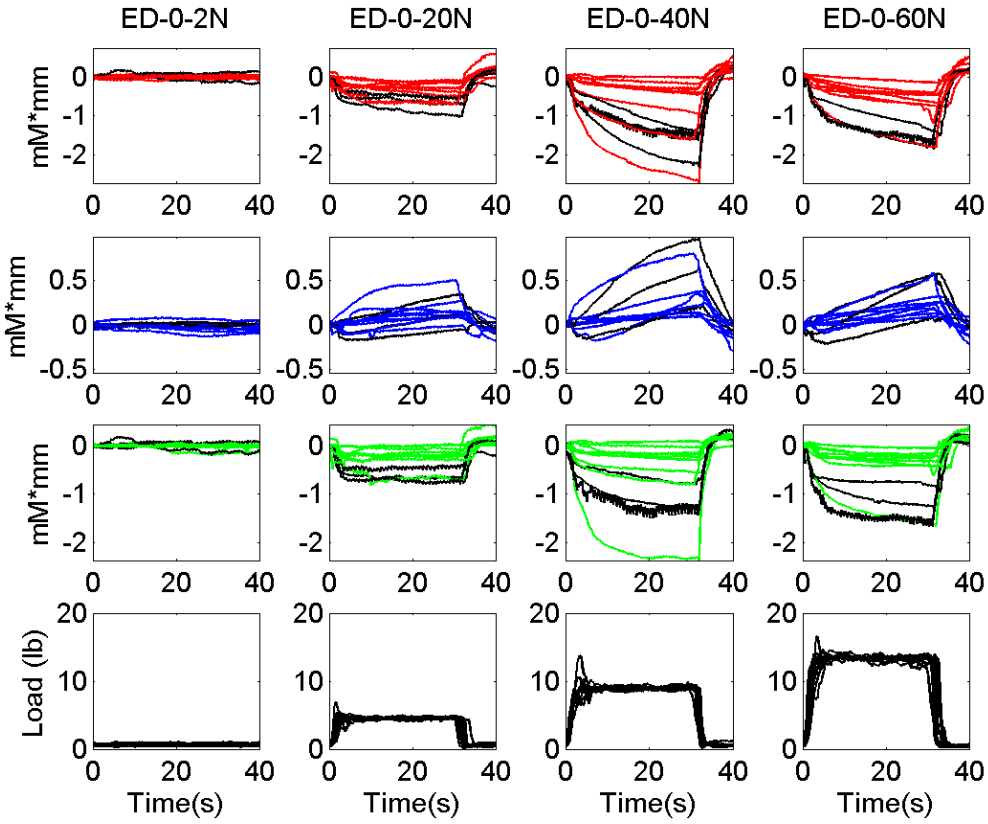
ED-0-2N
ED-0-20N
ED-0-40N
ED-0-60N
mM*mm
Load (lb)
Time(s)

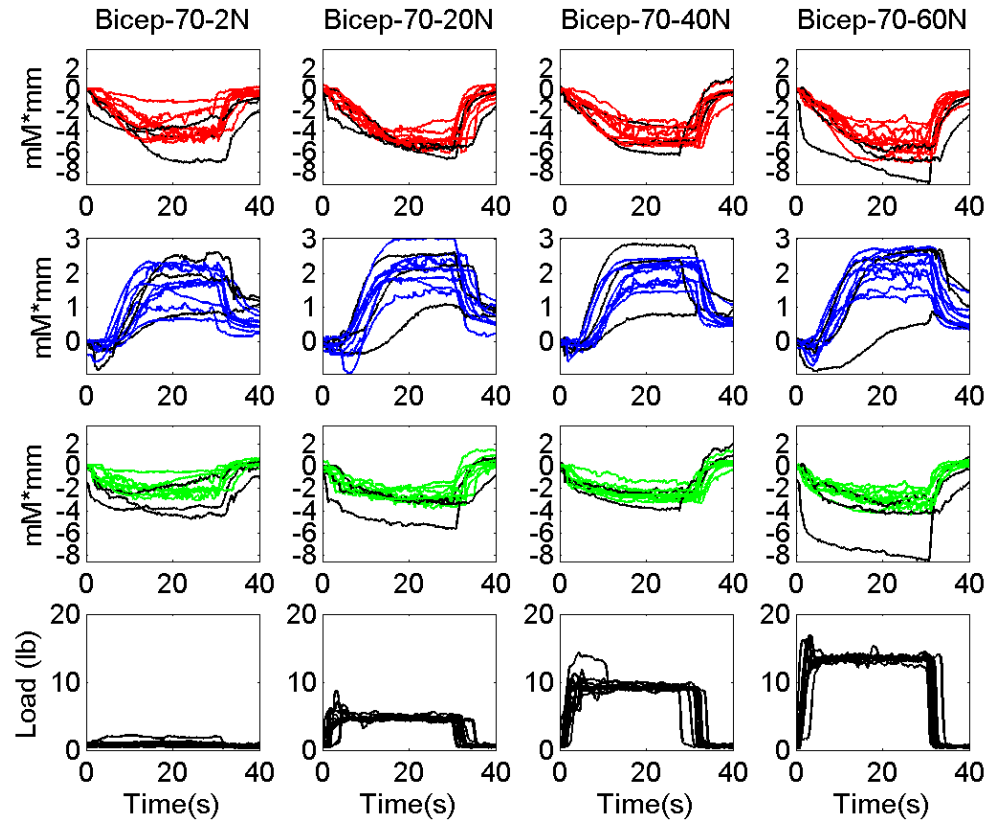
Bicep-70-2N
Bicep-70-20N
Bicep-70-40N
Bicep-70-60N
mM*mm
Load (lb)
Time(s)

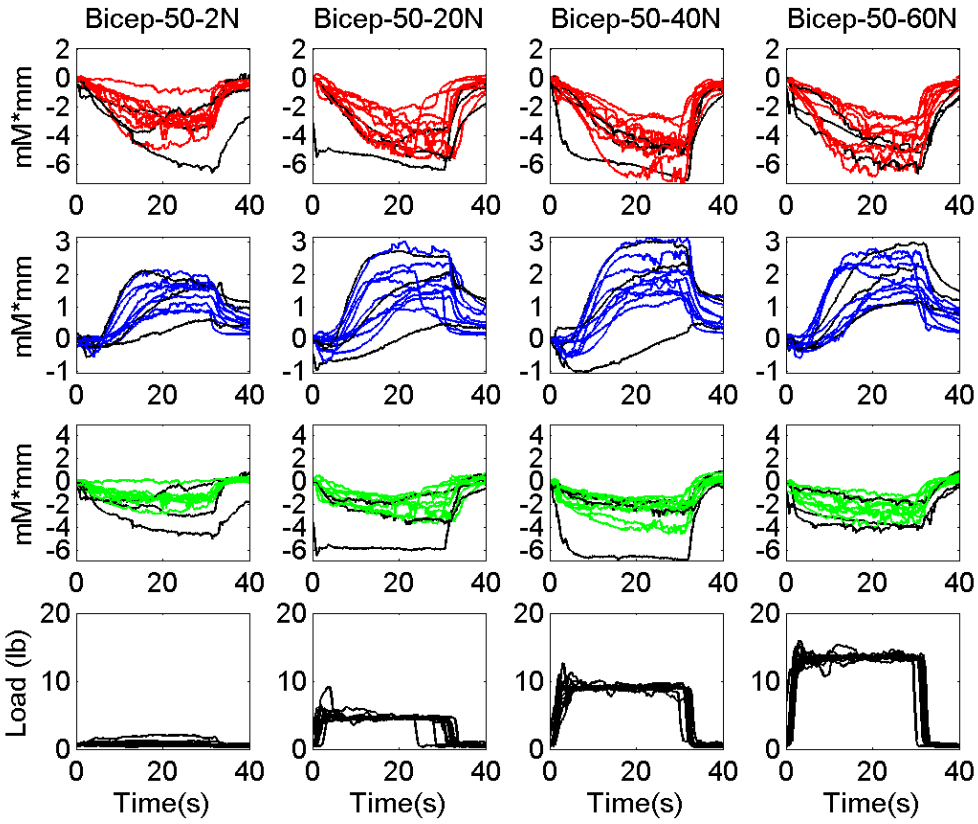
Bicep-50-2N
Bicep-50-20N
Bicep-50-40N
Bicep-50-60N
mM*mm
Load (lb)
Time(s)

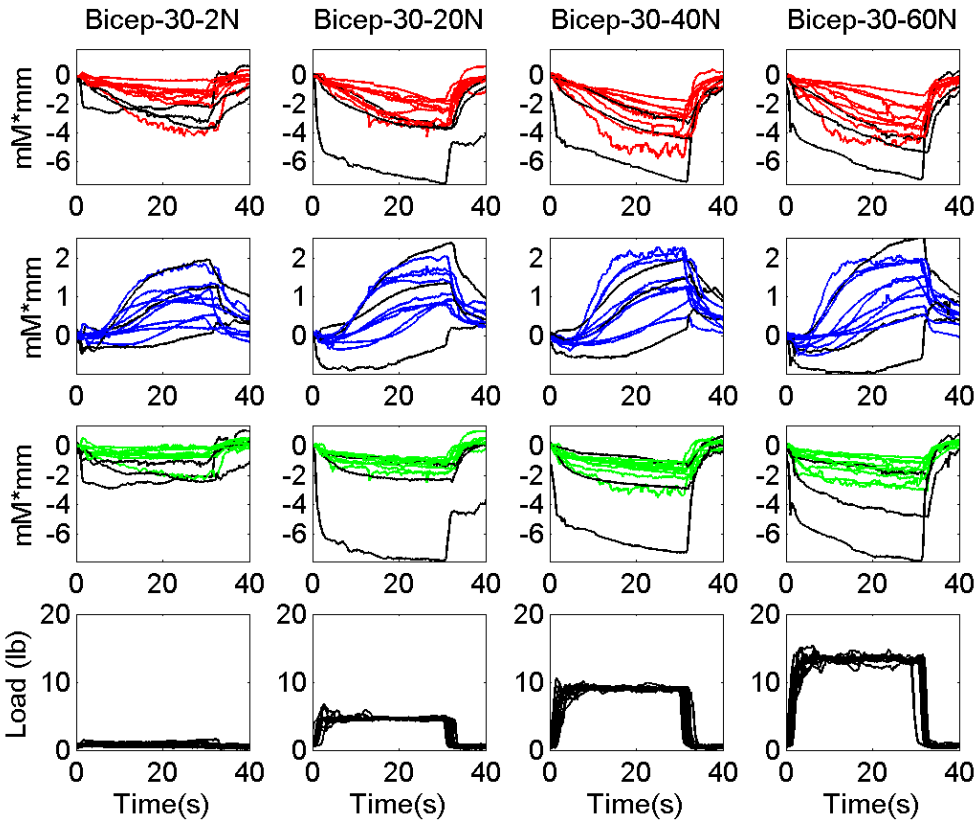
Bicep-30-2N
Bicep-30-20N
Bicep-30-40N
Bicep-30-60N
mM*mm
Load (lb)
Time(s)

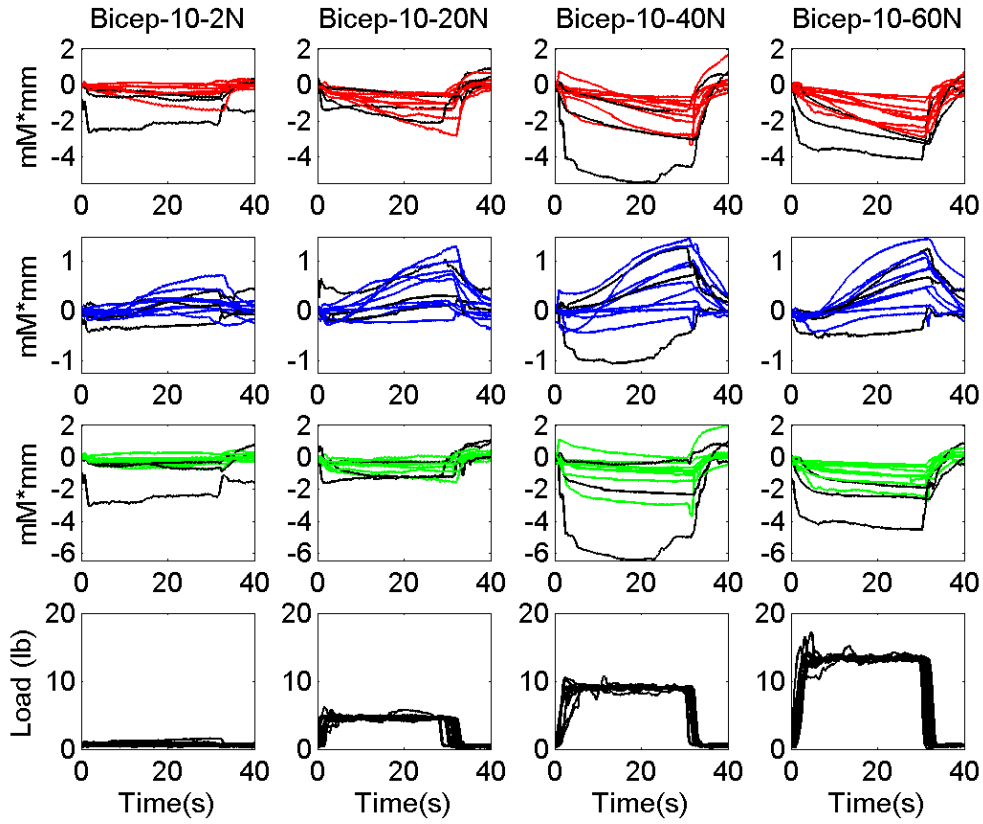
Bicep-10-2N
Bicep-10-20N
Bicep-10-40N
Bicep-10-60N
mM*mm
Load (lb)
Time(s)

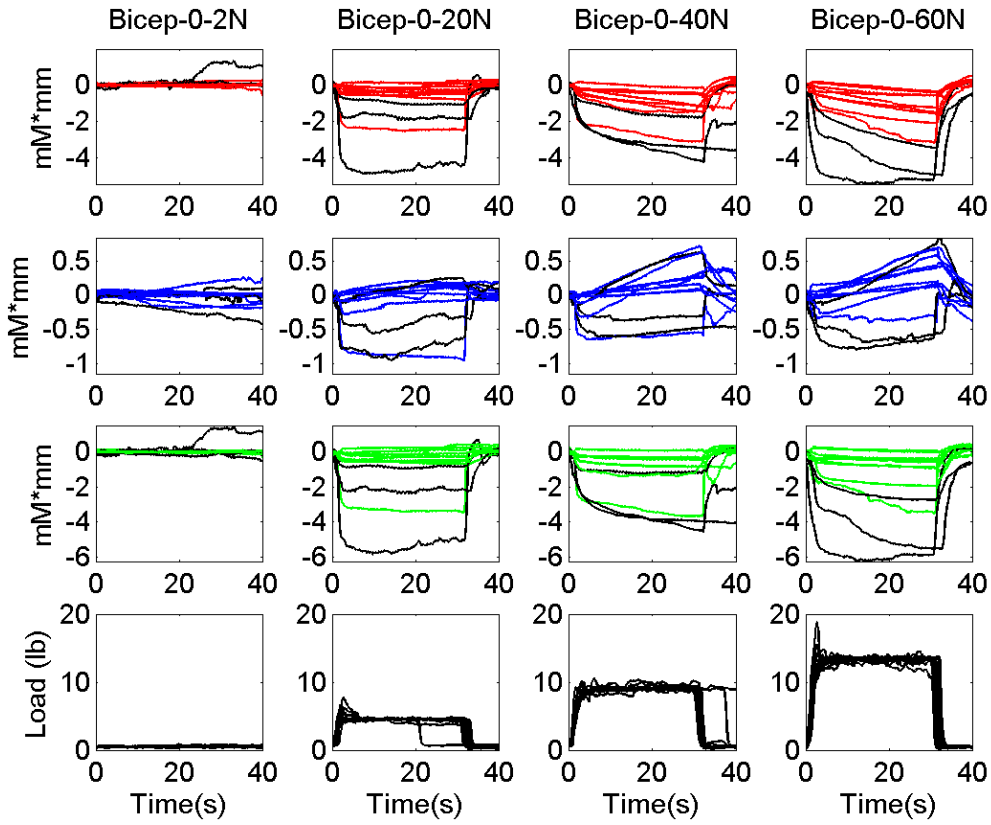
Bicep-0-2N
Bicep-0-20N
Bicep-0-40N
Bicep-0-60N
mM*mm
Load (lb)
Time(s)

APPENDIX B

The following figures show individual trial data for each subject. The subject number, period of loading, STT and contact force are noted in the title of each chart. Note that STT values displayed are skinfold values (Skinfold = 2xSTT).

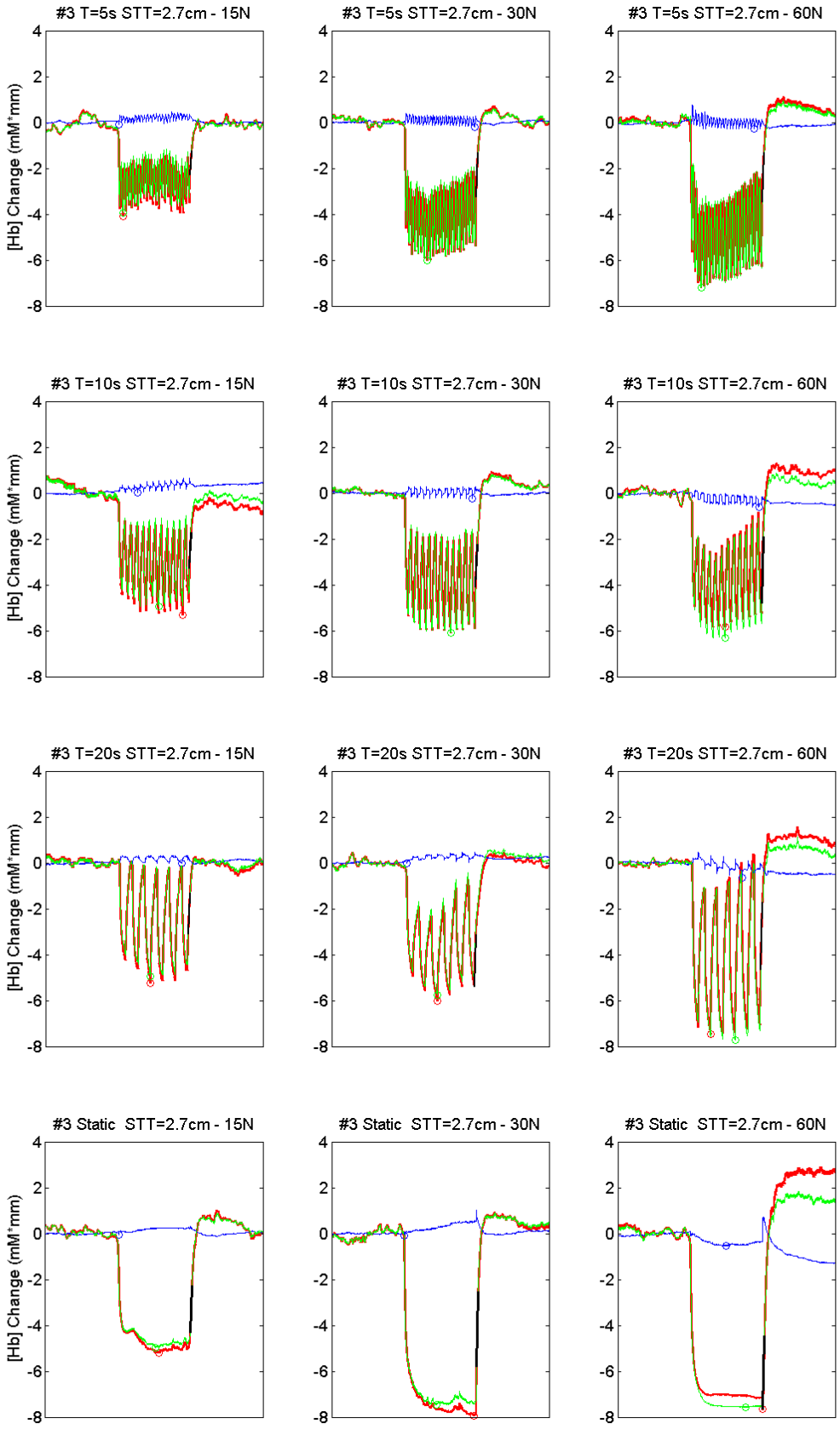
#3 T=5s STT=2.7cm - 15N
#3 T=5s STT=2.7cm - 30N
#3 T=5s STT=2.7cm - 60N
#3 T=10s STT=2.7cm - 15N
#3 T=10s STT=2.7cm - 30N
#3 T=10s STT=2.7cm - 60N
#3 T=20s STT=2.7cm - 15N
#3 T=20s STT=2.7cm - 30N
#3 T=20s STT=2.7cm - 60N
#3 Static STT=2.7cm - 15N
#3 Static STT=2.7cm - 30N
#3 Static STT=2.7cm - 60N
[Hb] Change (mM*mm)
4
2
0
-2
-4
-6
-8

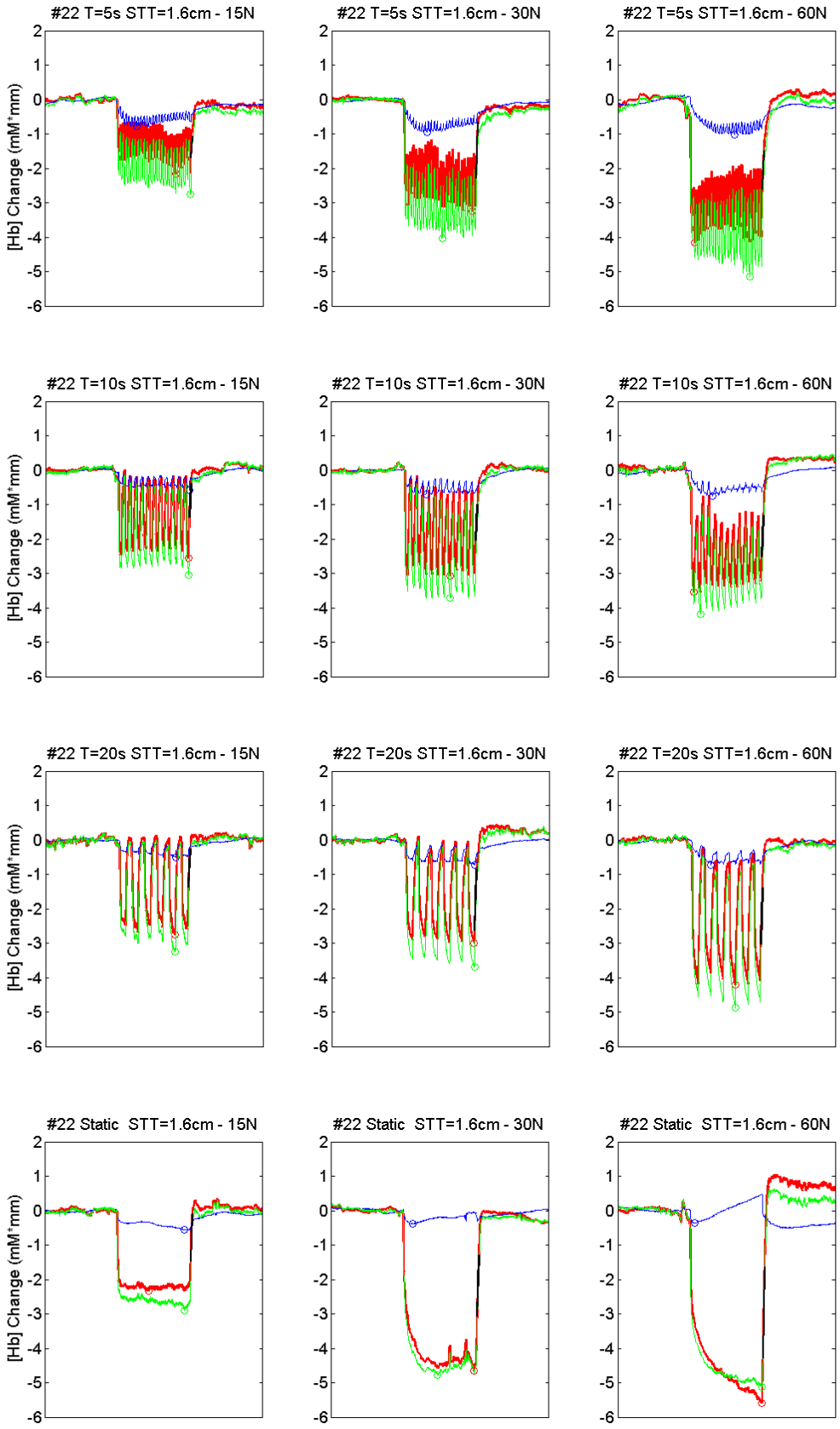
#22 T=5s STT=1.6cm - 15N
#22 T=5s STT=1.6cm - 30N
#22 T=5s STT=1.6cm - 60N
#22 T=10s STT=1.6cm - 15N
#22 T=10s STT=1.6cm - 30N
#22 T=10s STT=1.6cm - 60N
#22 T=20s STT=1.6cm - 15N
#22 T=20s STT=1.6cm - 30N
#22 T=20s STT=1.6cm - 60N
#22 Static STT=1.6cm - 15N
#22 Static STT=1.6cm - 30N
#22 Static STT=1.6cm - 60N
[Hb] Change (mM*mm)
2
1
0
-1
-2
-3
-4
-5
-6

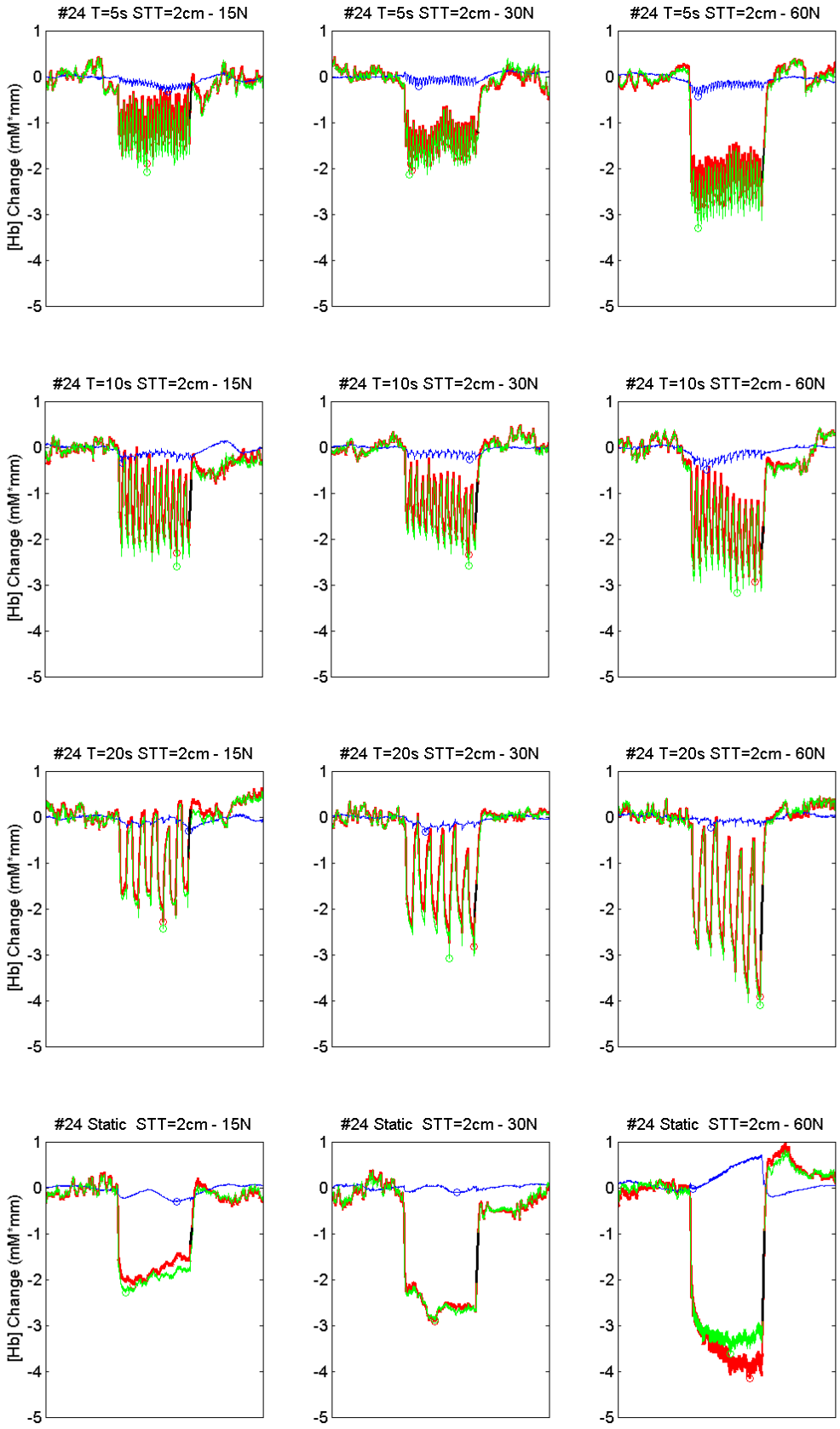
#24 T=5s STT=2cm - 15N
#24 T=5s STT=2cm - 30N
#24 T=5s STT=2cm - 60N
#24 T=10s STT=2cm - 15N
#24 T=10s STT=2cm - 30N
#24 T=10s STT=2cm - 60N
#24 T=20s STT=2cm - 15N
#24 T=20s STT=2cm - 30N
#24 T=20s STT=2cm - 60N
#24 Static STT=2cm - 15N
#24 Static STT=2cm - 30N
#24 Static STT=2cm - 60N
[Hb] Change (mM*mm)
1
0
-1
-2
-3
-4
-5

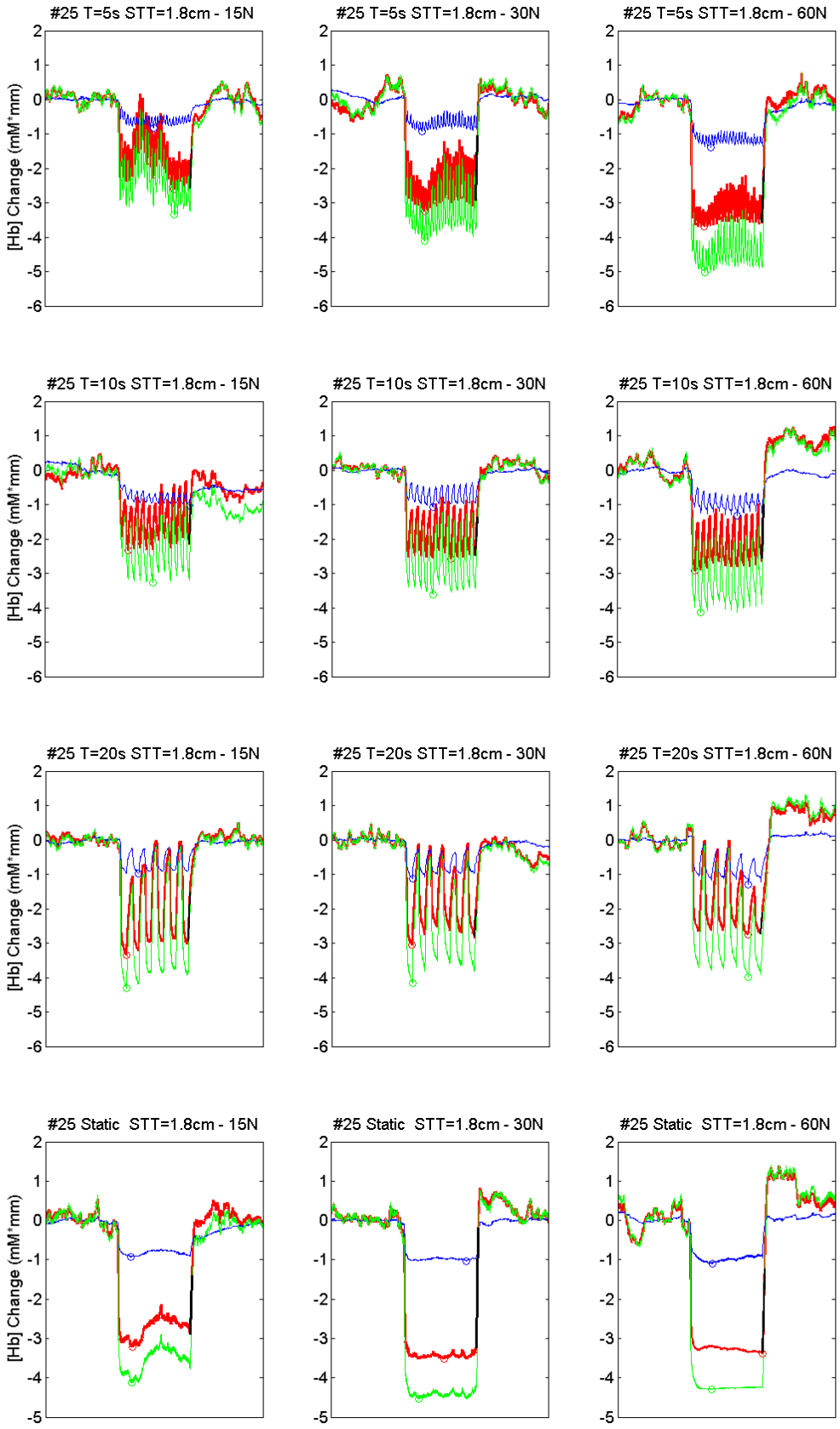
#25 T=5s STT=1.8cm - 15N
#25 T=5s STT=1.8cm - 30N
#25 T=5s STT=1.8cm - 60N
#25 T=10s STT=1.8cm - 15N
#25 T=10s STT=1.8cm - 30N
#25 T=10s STT=1.8cm - 60N
#25 T=20s STT=1.8cm - 15N
#25 T=20s STT=1.8cm - 30N
#25 T=20s STT=1.8cm - 60N
#25 Static STT=1.8cm - 15N
#25 Static STT=1.8cm - 30N
#25 Static STT=1.8cm - 60N
[Hb] Change (mM*mm)

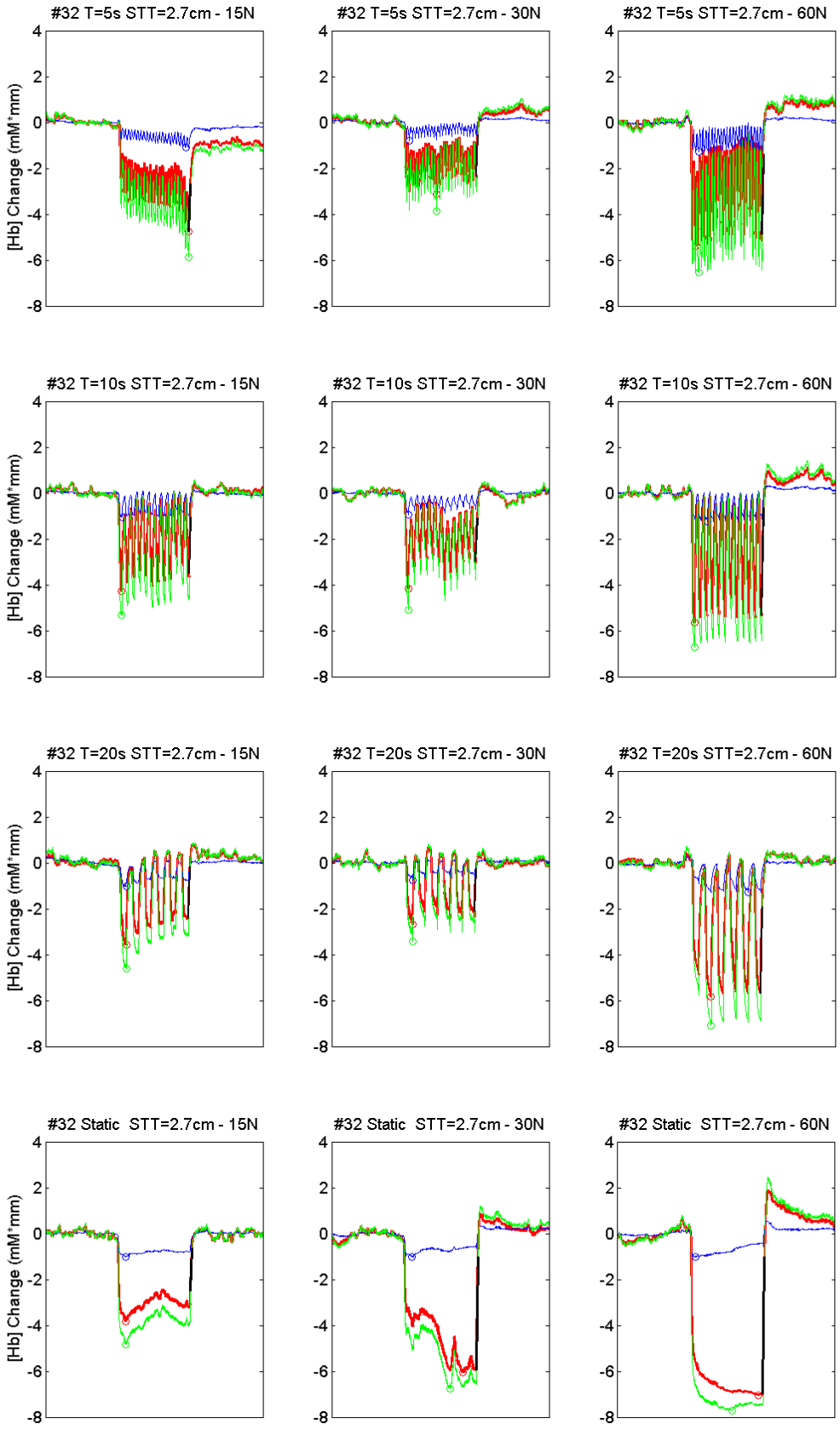
#32 T=5s STT=2.7cm - 15N
#32 T=5s STT=2.7cm - 30N
#32 T=5s STT=2.7cm - 60N
#32 T=10s STT=2.7cm - 15N
#32 T=10s STT=2.7cm - 30N
#32 T=10s STT=2.7cm - 60N
#32 T=20s STT=2.7cm - 15N
#32 T=20s STT=2.7cm - 30N
#32 T=20s STT=2.7cm - 60N
#32 Static STT=2.7cm - 15N
#32 Static STT=2.7cm - 30N
#32 Static STT=2.7cm - 60N
[Hb] Change (mM*mm)
4
2
0
-2
-4
-6
-8

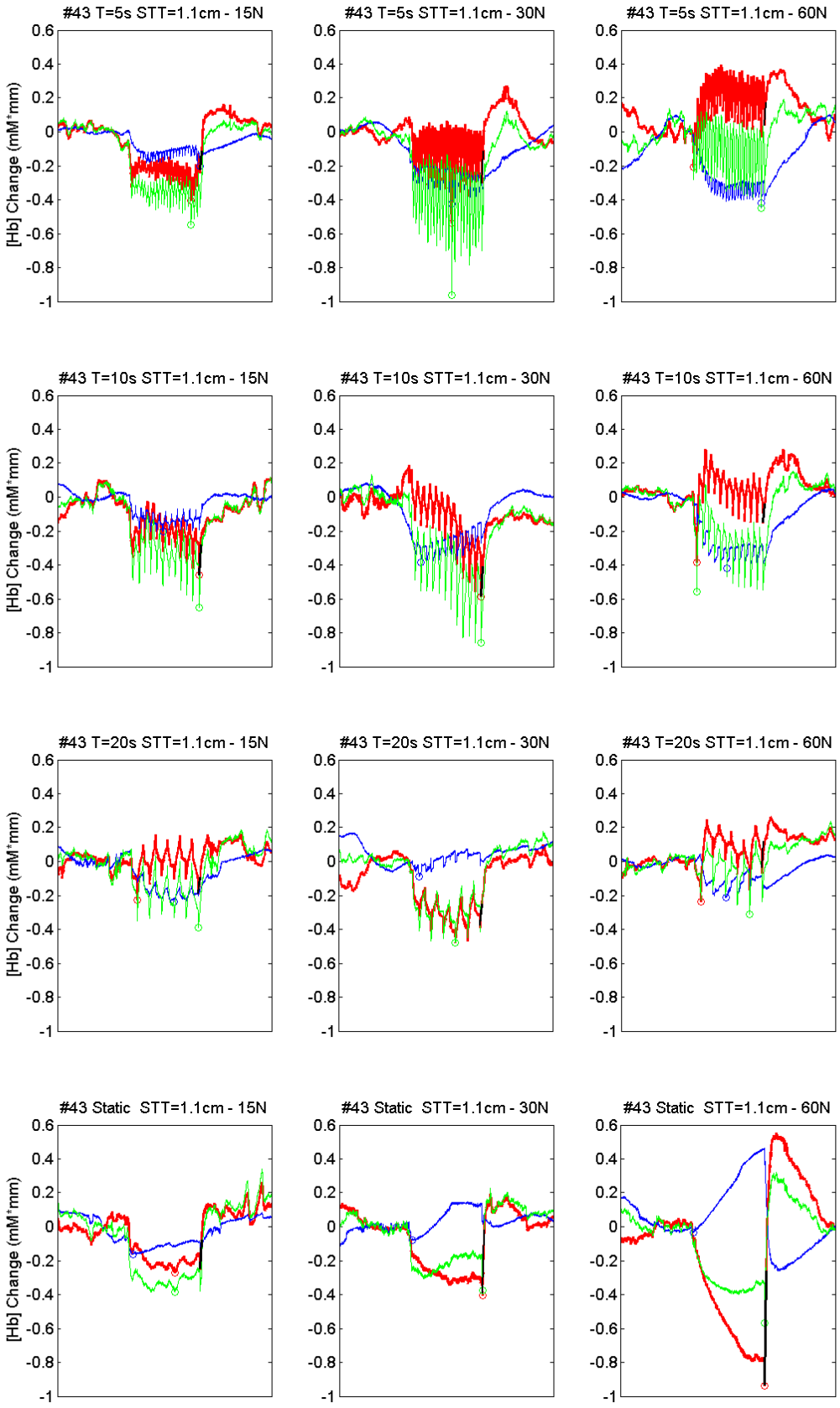
#43 T=5s STT=1.1cm - 15N
#43 T=5s STT=1.1cm - 30N
#43 T=5s STT=1.1cm - 60N
#43 T=10s STT=1.1cm - 15N
#43 T=10s STT=1.1cm - 30N
#43 T=10s STT=1.1cm - 60N
#43 T=20s STT=1.1cm - 15N
#43 T=20s STT=1.1cm - 30N
#43 T=20s STT=1.1cm - 60N
#43 Static STT=1.1cm - 15N
#43 Static STT=1.1cm - 30N
#43 Static STT=1.1cm - 60N
[Hb] Change (mM*mm)
0.6
0.4
0.2
0
-0.2
-0.4
-0.6
-0.8
-1

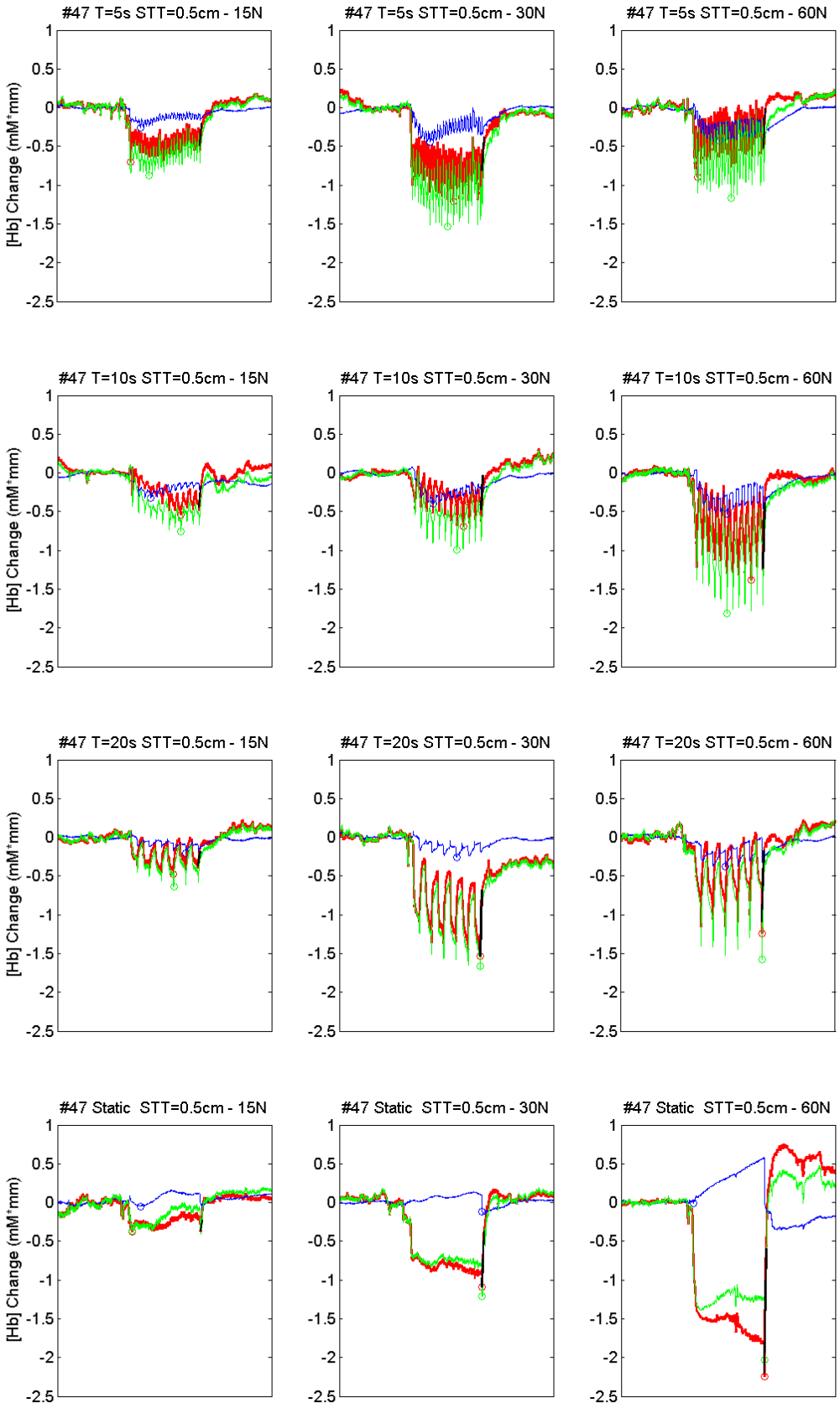
#47 T=5s STT=0.5cm - 15N
#47 T=5s STT=0.5cm - 30N
#47 T=5s STT=0.5cm - 60N
#47 T=10s STT=0.5cm - 15N
#47 T=10s STT=0.5cm - 30N
#47 T=10s STT=0.5cm - 60N
#47 T=20s STT=0.5cm - 15N
#47 T=20s STT=0.5cm - 30N
#47 T=20s STT=0.5cm - 60N
#47 Static STT=0.5cm - 15N
#47 Static STT=0.5cm - 30N
#47 Static STT=0.5cm - 60N
[Hb] Change (mM*mm)
1
0.5
0
-0.5
-1
-1.5
-2
-2.5

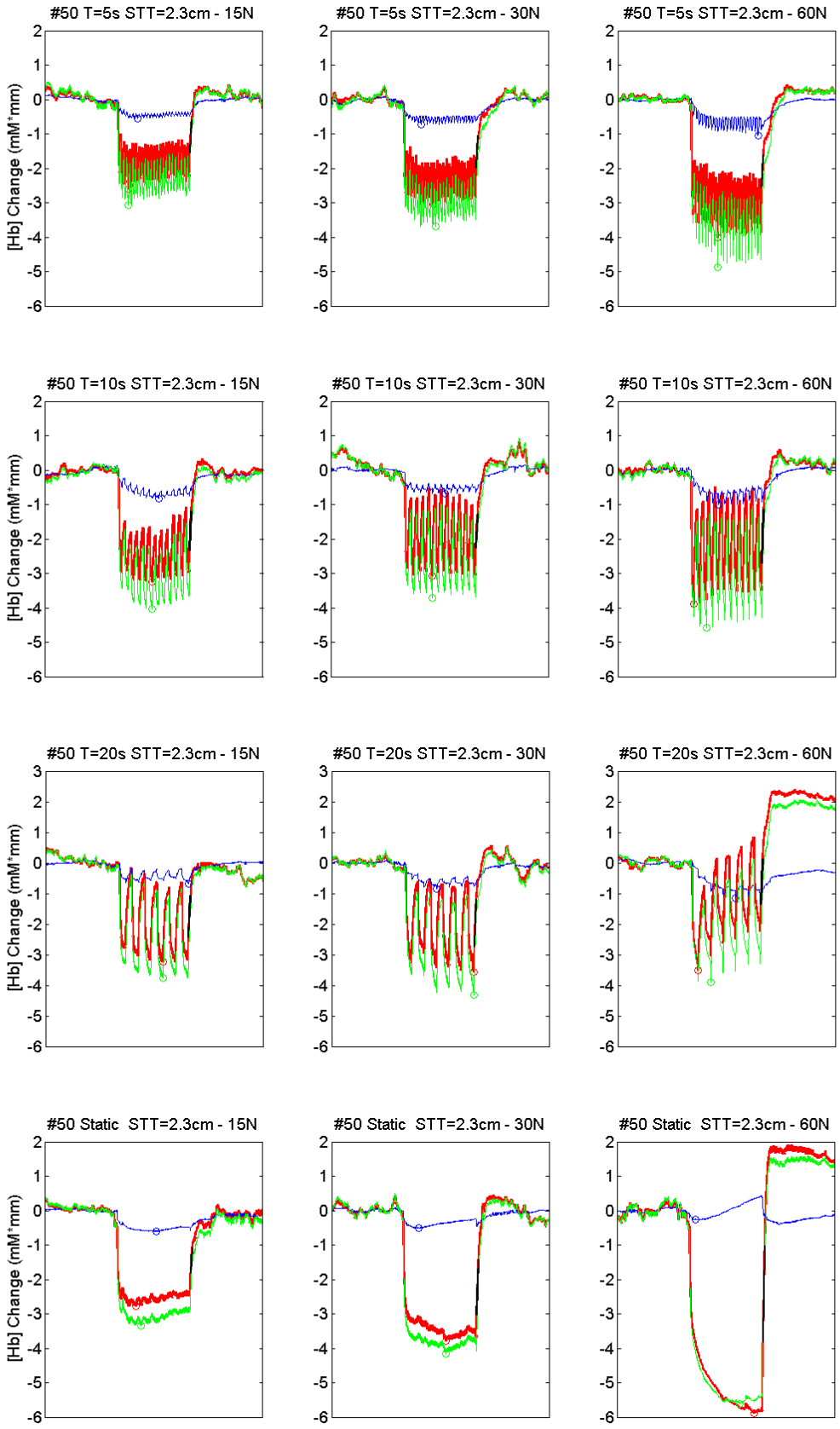
#50 T=5s STT=2.3cm - 15N
#50 T=5s STT=2.3cm - 30N
#50 T=5s STT=2.3cm - 60N
#50 T=10s STT=2.3cm - 15N
#50 T=10s STT=2.3cm - 30N
#50 T=10s STT=2.3cm - 60N
#50 T=20s STT=2.3cm - 15N
#50 T=20s STT=2.3cm - 30N
#50 T=20s STT=2.3cm - 60N
#50 Static STT=2.3cm - 15N
#50 Static STT=2.3cm - 30N
#50 Static STT=2.3cm - 60N
[Hb] Change (mM*mm)

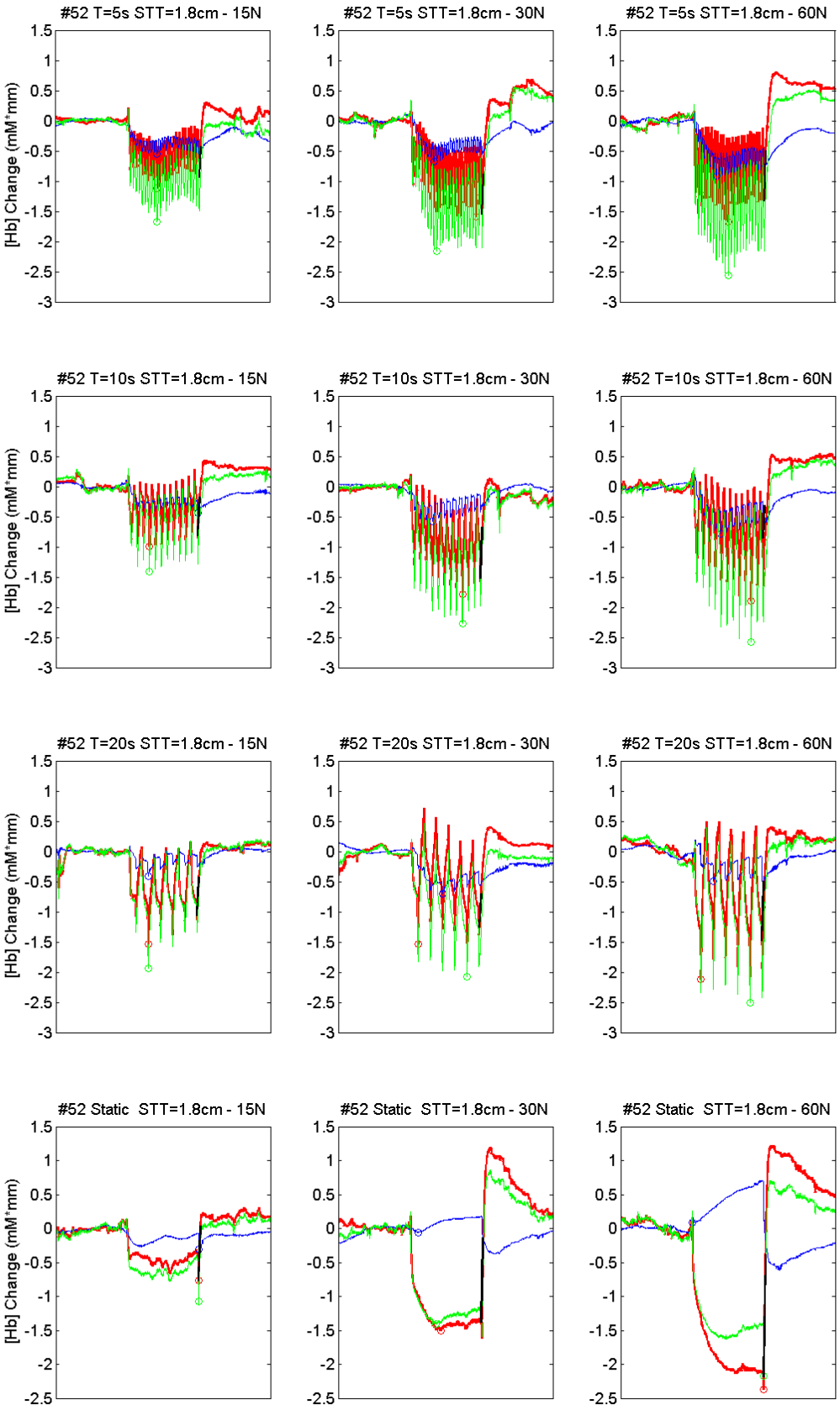
#52 T=5s STT=1.8cm - 15N
#52 T=5s STT=1.8cm - 30N
#52 T=5s STT=1.8cm - 60N
#52 T=10s STT=1.8cm - 15N
#52 T=10s STT=1.8cm - 30N
#52 T=10s STT=1.8cm - 60N
#52 T=20s STT=1.8cm - 15N
#52 T=20s STT=1.8cm - 30N
#52 T=20s STT=1.8cm - 60N
#52 Static STT=1.8cm - 15N
#52 Static STT=1.8cm - 30N
#52 Static STT=1.8cm - 60N
[Hb] Change (mM*mm)

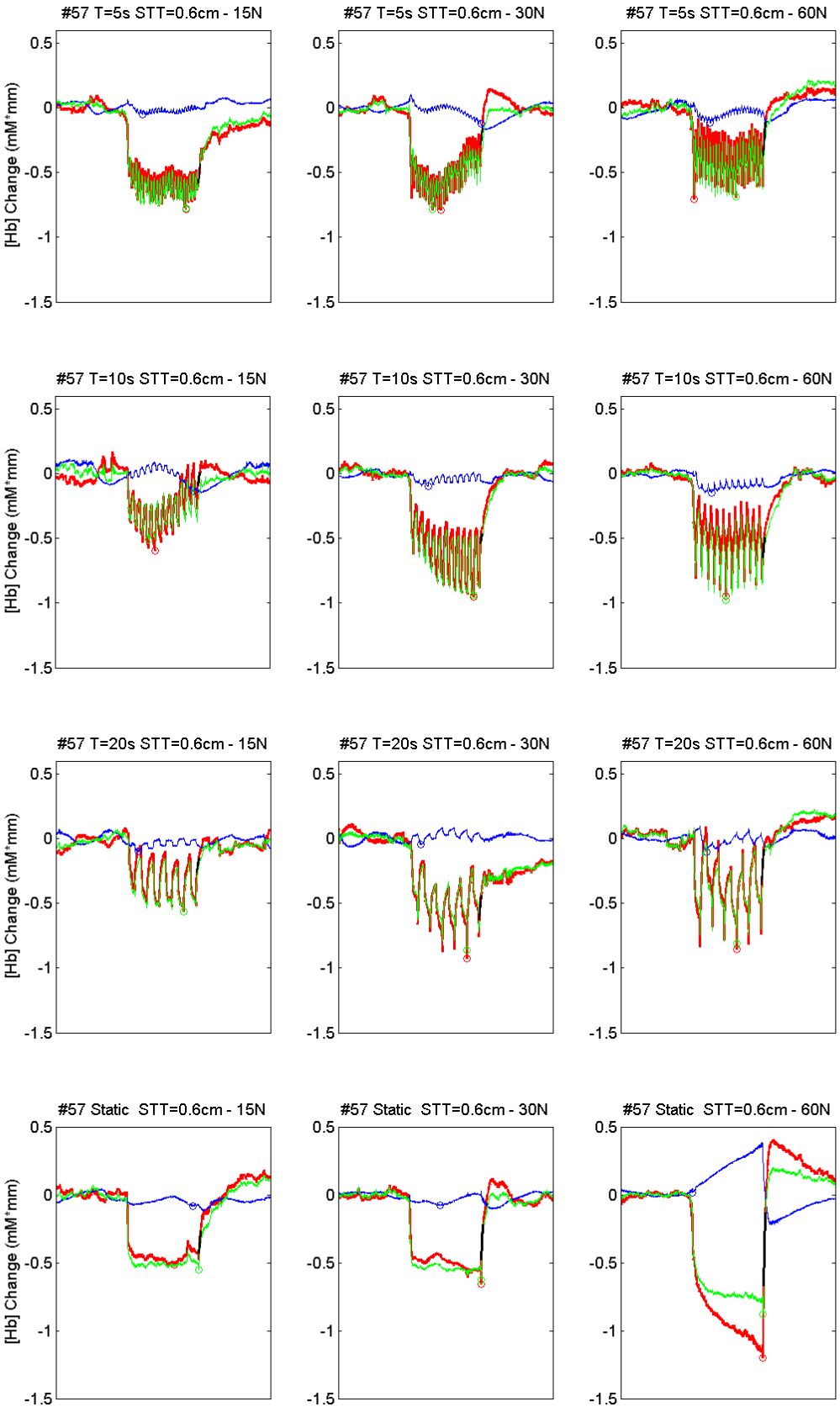
#57 T=5s STT=0.6cm - 15N
#57 T=5s STT=0.6cm - 30N
#57 T=5s STT=0.6cm - 60N
#57 T=10s STT=0.6cm - 15N
#57 T=10s STT=0.6cm - 30N
#57 T=10s STT=0.6cm - 60N
#57 T=20s STT=0.6cm - 15N
#57 T=20s STT=0.6cm - 30N
#57 T=20s STT=0.6cm - 60N
#57 Static STT=0.6cm - 15N
#57 Static STT=0.6cm - 30N
#57 Static STT=0.6cm - 60N
[Hb] Change (mM*mm)
0.5
0
-0.5
-1
-1.5

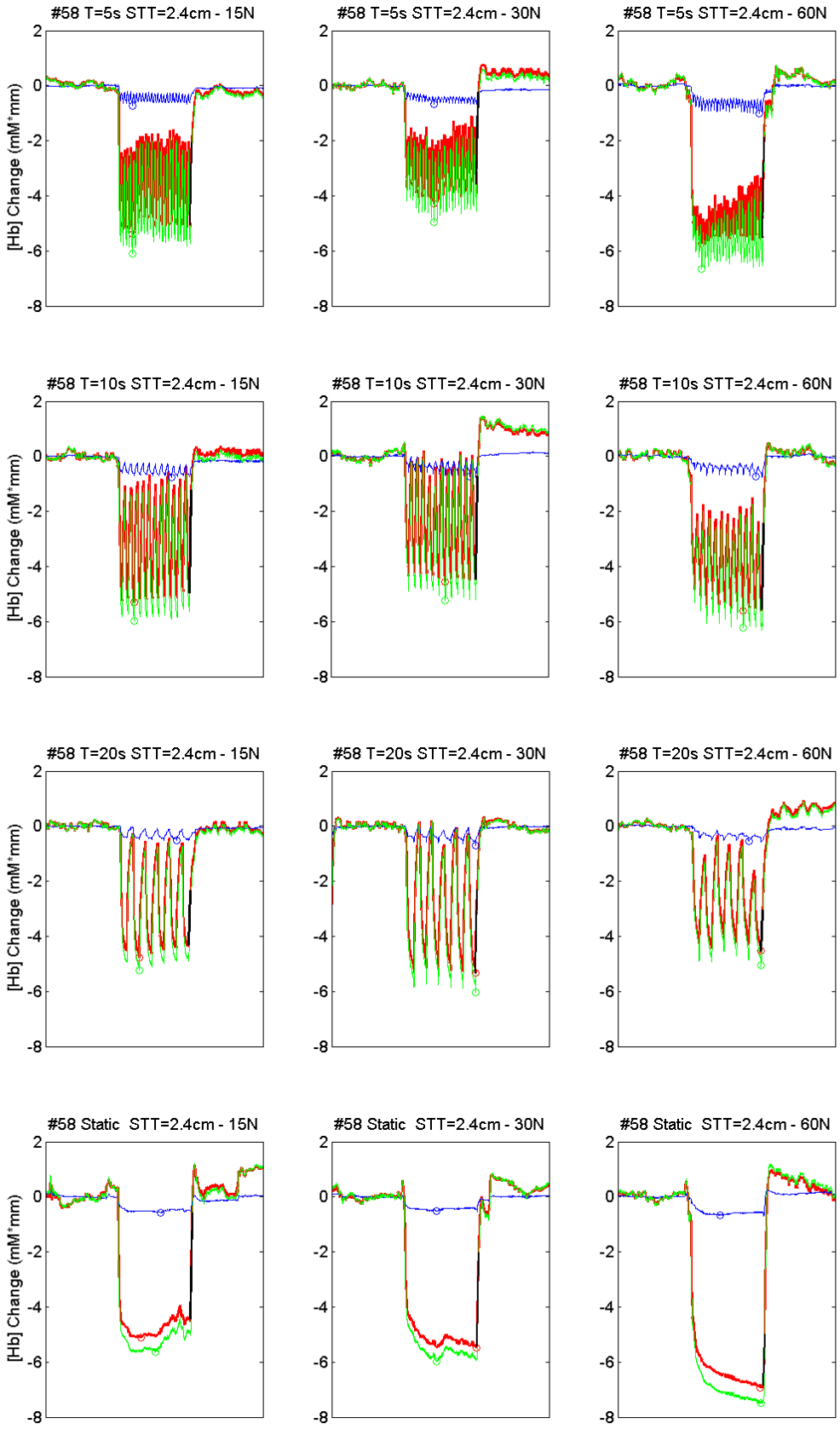
#58 T=5s STT=2.4cm - 15N
#58 T=5s STT=2.4cm - 30N
#58 T=5s STT=2.4cm - 60N
#58 T=10s STT=2.4cm - 15N
#58 T=10s STT=2.4cm - 30N
#58 T=10s STT=2.4cm - 60N
#58 T=20s STT=2.4cm - 15N
#58 T=20s STT=2.4cm - 30N
#58 T=20s STT=2.4cm - 60N
#58 Static STT=2.4cm - 15N
#58 Static STT=2.4cm - 30N
#58 Static STT=2.4cm - 60N
[Hb] Change (mM*mm)
2
0
-2
-4
-6
-8

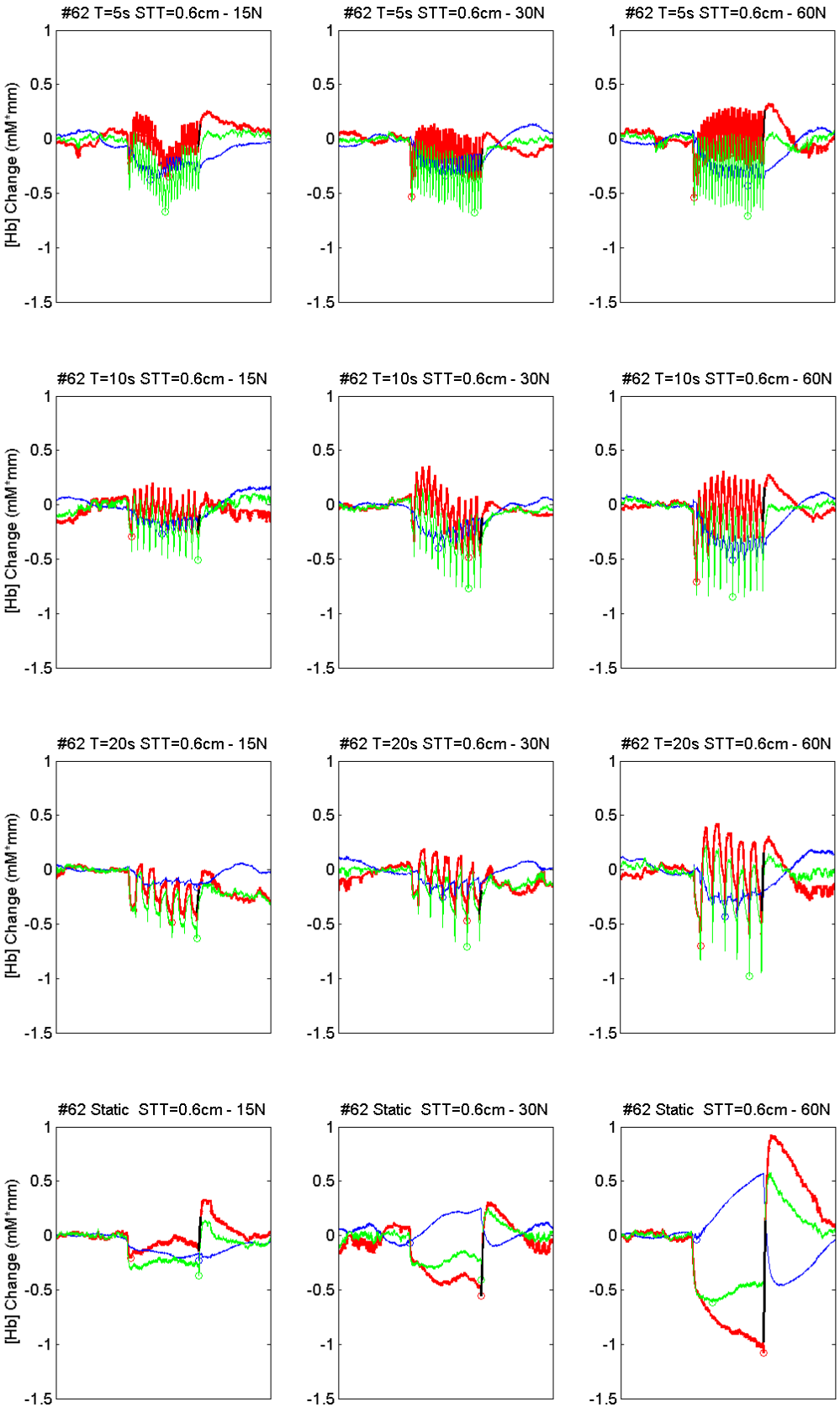
#62 T=5s STT=0.6cm - 15N
#62 T=5s STT=0.6cm - 30N
#62 T=5s STT=0.6cm - 60N
#62 T=10s STT=0.6cm - 15N
#62 T=10s STT=0.6cm - 30N
#62 T=10s STT=0.6cm - 60N
#62 T=20s STT=0.6cm - 15N
#62 T=20s STT=0.6cm - 30N
#62 T=20s STT=0.6cm - 60N
#62 Static STT=0.6cm - 15N
#62 Static STT=0.6cm - 30N
#62 Static STT=0.6cm - 60N
[Hb] Change (mM*mm)
1
0.5
0
-0.5
-1
-1.5

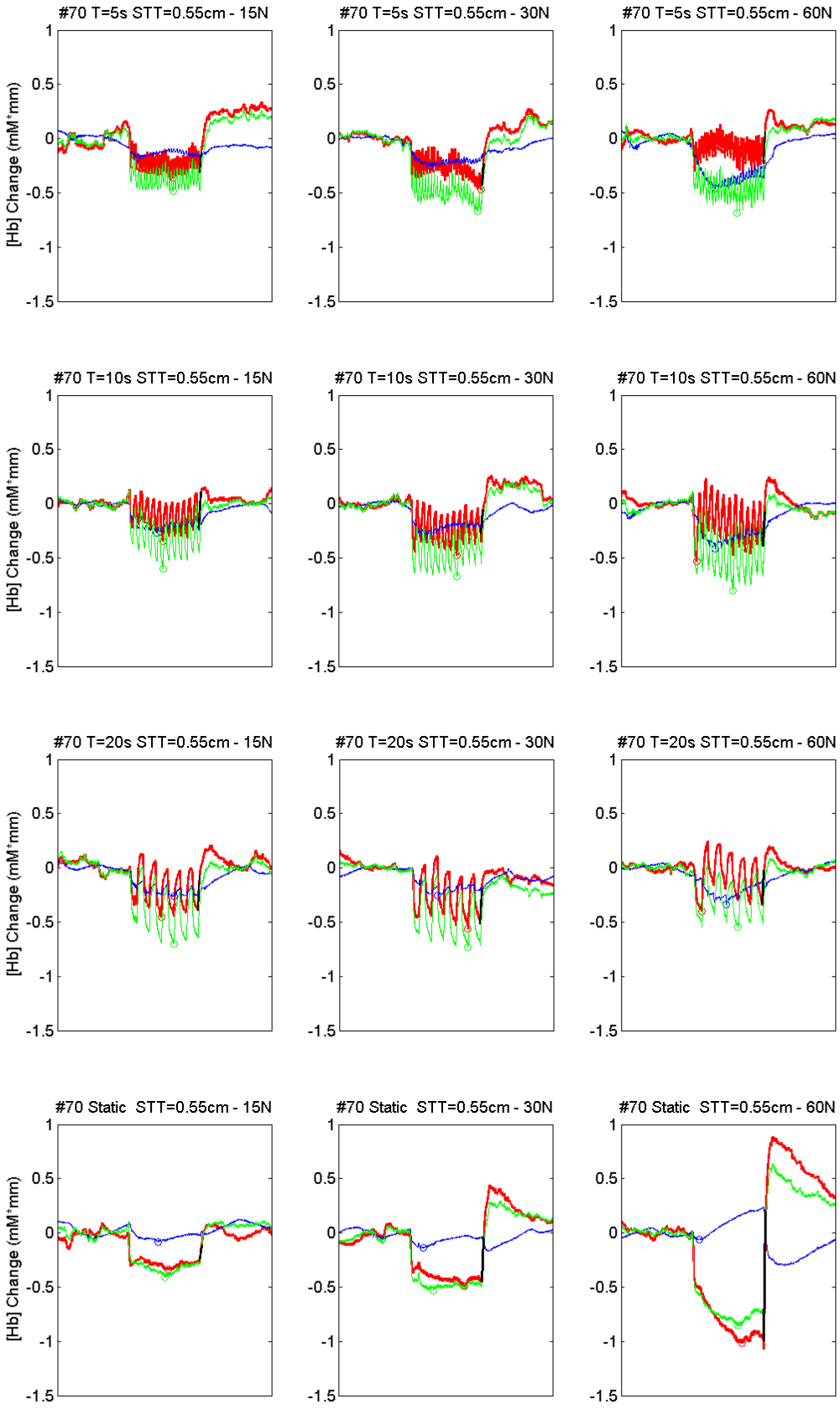
#70 T=5s STT=0.55cm - 15N
#70 T=5s STT=0.55cm - 30N
#70 T=5s STT=0.55cm - 60N
#70 T=10s STT=0.55cm - 15N
#70 T=10s STT=0.55cm - 30N
#70 T=10s STT=0.55cm - 60N
#70 T=20s STT=0.55cm - 15N
#70 T=20s STT=0.55cm - 30N
#70 T=20s STT=0.55cm - 60N
#70 Static STT=0.55cm - 15N
#70 Static STT=0.55cm - 30N
#70 Static STT=0.55cm - 60N
[Hb] Change (mM*mm)
1
0.5
0
-0.5
-1
-1.5

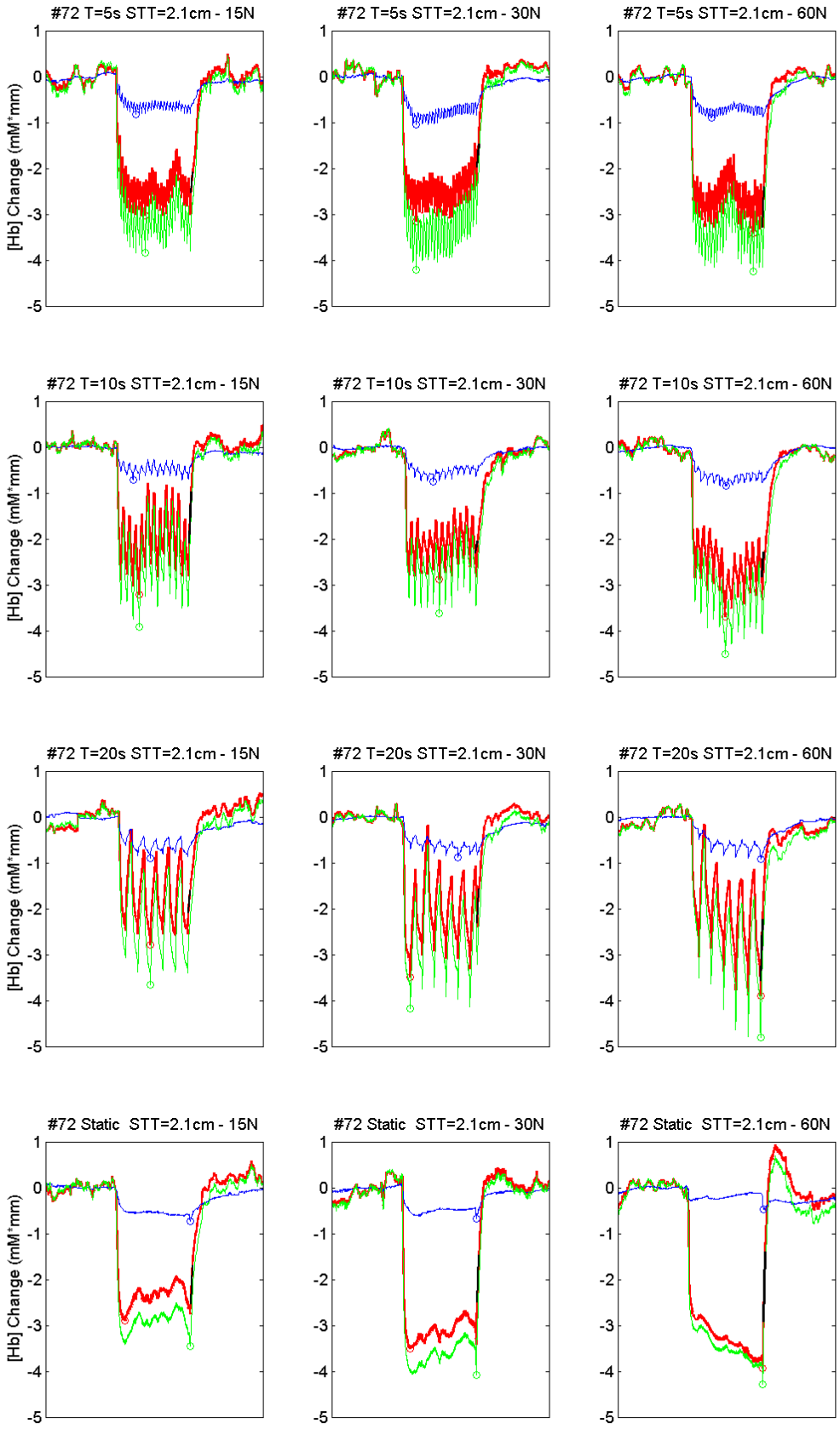
#72 T=5s STT=2.1cm - 15N
#72 T=5s STT=2.1cm - 30N
#72 T=5s STT=2.1cm - 60N
#72 T=10s STT=2.1cm - 15N
#72 T=10s STT=2.1cm - 30N
#72 T=10s STT=2.1cm - 60N
#72 T=20s STT=2.1cm - 15N
#72 T=20s STT=2.1cm - 30N
#72 T=20s STT=2.1cm - 60N
#72 Static STT=2.1cm - 15N
#72 Static STT=2.1cm - 30N
#72 Static STT=2.1cm - 60N
[Hb] Change (mM*mm)
1
0
-1
-2
-3
-4
-5

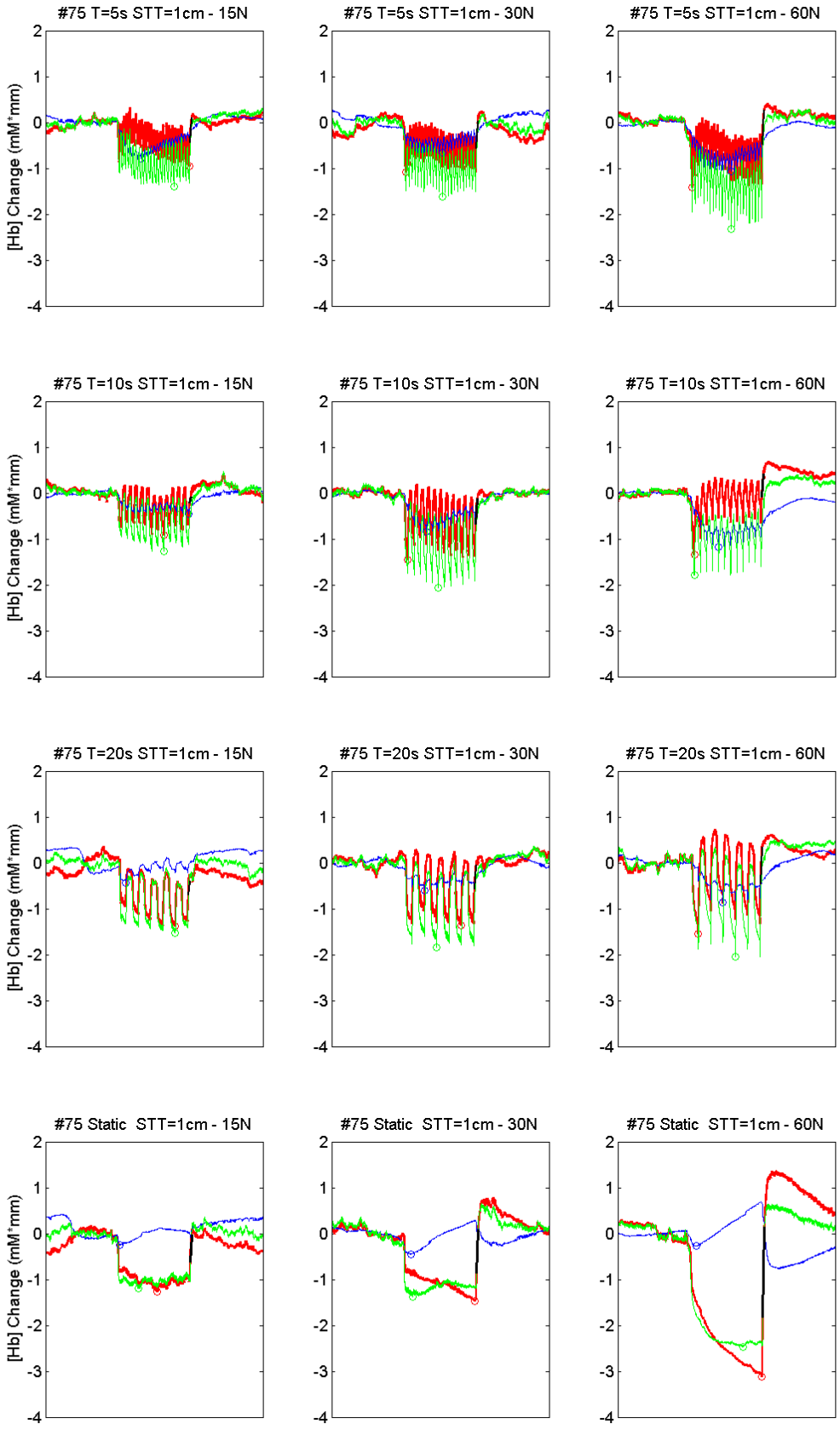
#75 T=5s STT=1cm - 15N
#75 T=5s STT=1cm - 30N
#75 T=5s STT=1cm - 60N
#75 T=10s STT=1cm - 15N
#75 T=10s STT=1cm - 30N
#75 T=10s STT=1cm - 60N
#75 T=20s STT=1cm - 15N
#75 T=20s STT=1cm - 30N
#75 T=20s STT=1cm - 60N
#75 Static STT=1cm - 15N
#75 Static STT=1cm - 30N
#75 Static STT=1cm - 60N
[Hb] Change (mM*mm)
2
1
0
-1
-2
-3
-4

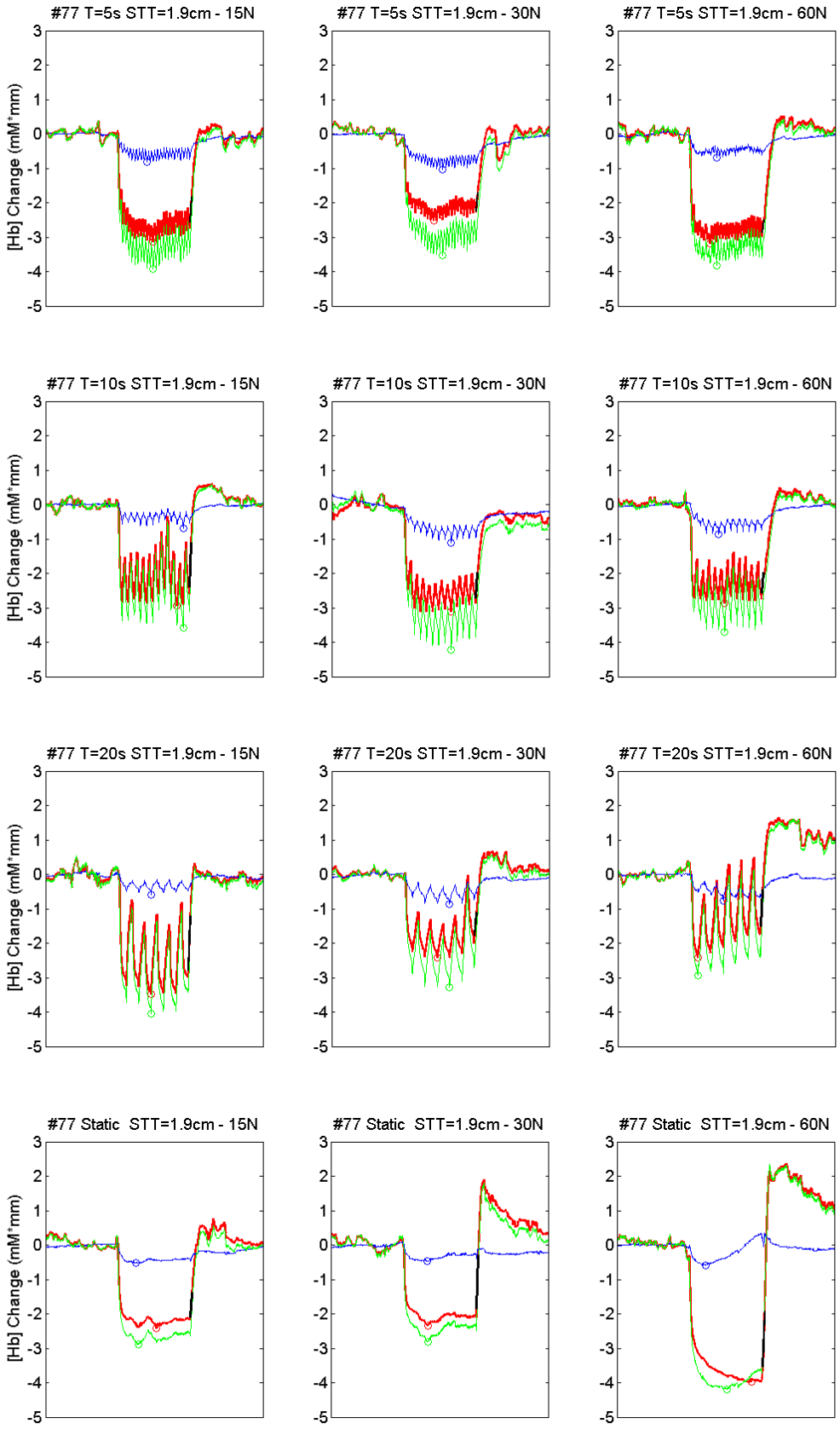
#77 T=5s STT=1.9cm - 15N
#77 T=5s STT=1.9cm - 30N
#77 T=5s STT=1.9cm - 60N
#77 T=10s STT=1.9cm - 15N
#77 T=10s STT=1.9cm - 30N
#77 T=10s STT=1.9cm - 60N
#77 T=20s STT=1.9cm - 15N
#77 T=20s STT=1.9cm - 30N
#77 T=20s STT=1.9cm - 60N
#77 Static STT=1.9cm - 15N
#77 Static STT=1.9cm - 30N
#77 Static STT=1.9cm - 60N
[Hb] Change (mM*mm)
3
2
1
0
-1
-2
-3
-4
-5

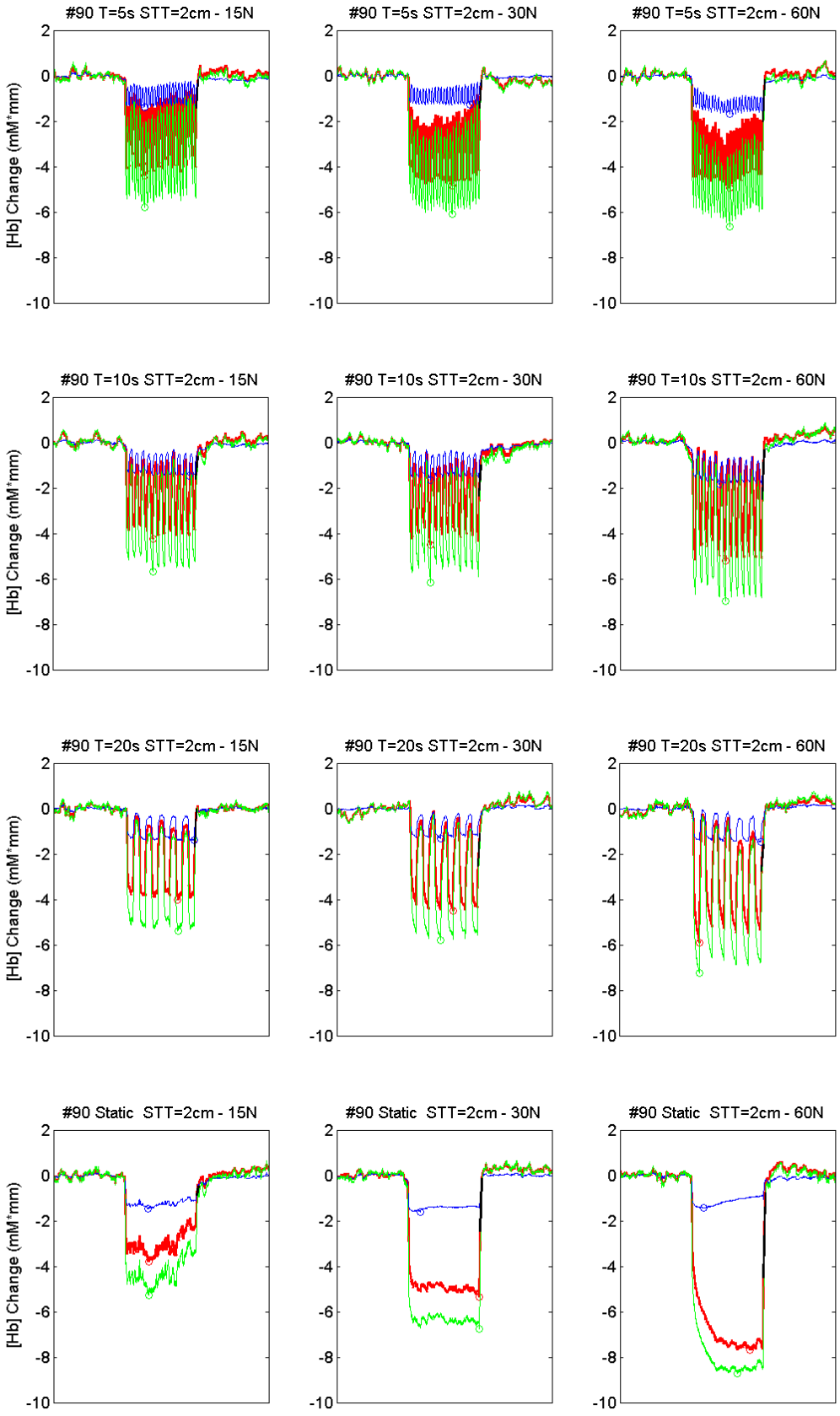
#90 T=5s STT=2cm - 15N
#90 T=5s STT=2cm - 30N
#90 T=5s STT=2cm - 60N
#90 T=10s STT=2cm - 15N
#90 T=10s STT=2cm - 30N
#90 T=10s STT=2cm - 60N
#90 T=20s STT=2cm - 15N
#90 T=20s STT=2cm - 30N
#90 T=20s STT=2cm - 60N
#90 Static STT=2cm - 15N
#90 Static STT=2cm - 30N
#90 Static STT=2cm - 60N
[Hb] Change (mM*mm)
2
0
-2
-4
-6
-8
-10

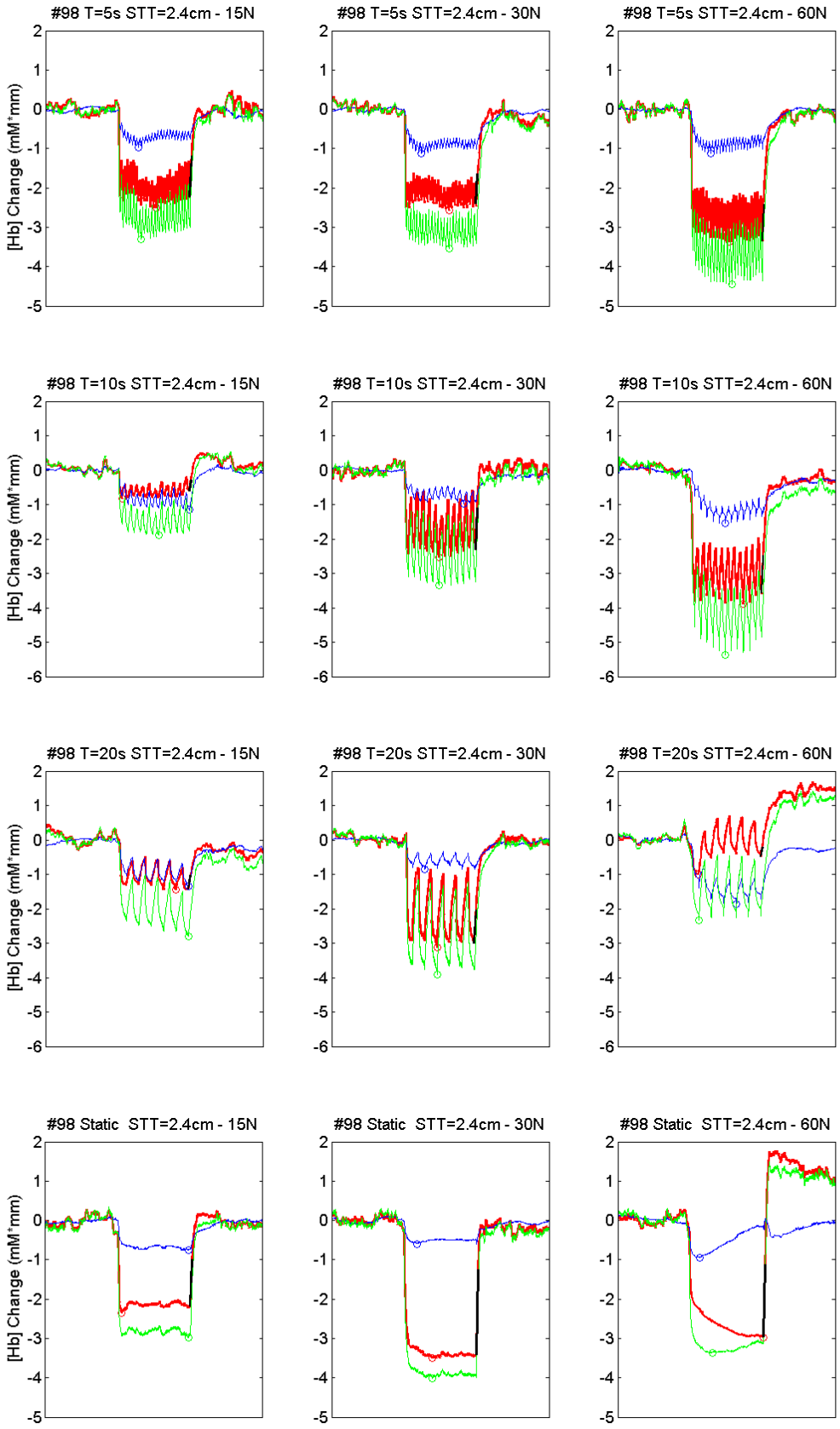
#98 T=5s STT=2.4cm - 15N
#98 T=5s STT=2.4cm - 30N
#98 T=5s STT=2.4cm - 60N
#98 T=10s STT=2.4cm - 15N
#98 T=10s STT=2.4cm - 30N
#98 T=10s STT=2.4cm - 60N
#98 T=20s STT=2.4cm - 15N
#98 T=20s STT=2.4cm - 30N
#98 T=20s STT=2.4cm - 60N
#98 Static STT=2.4cm - 15N
#98 Static STT=2.4cm - 30N
#98 Static STT=2.4cm - 60N
[Hb] Change (mM*mm)

APPENDIX C

The following figure are the complete set of spatial sensitivity maps for simulations at all STT and SDS. All SDS for each STT are displayed on one page and the titles indicate the values of STT and SDS.

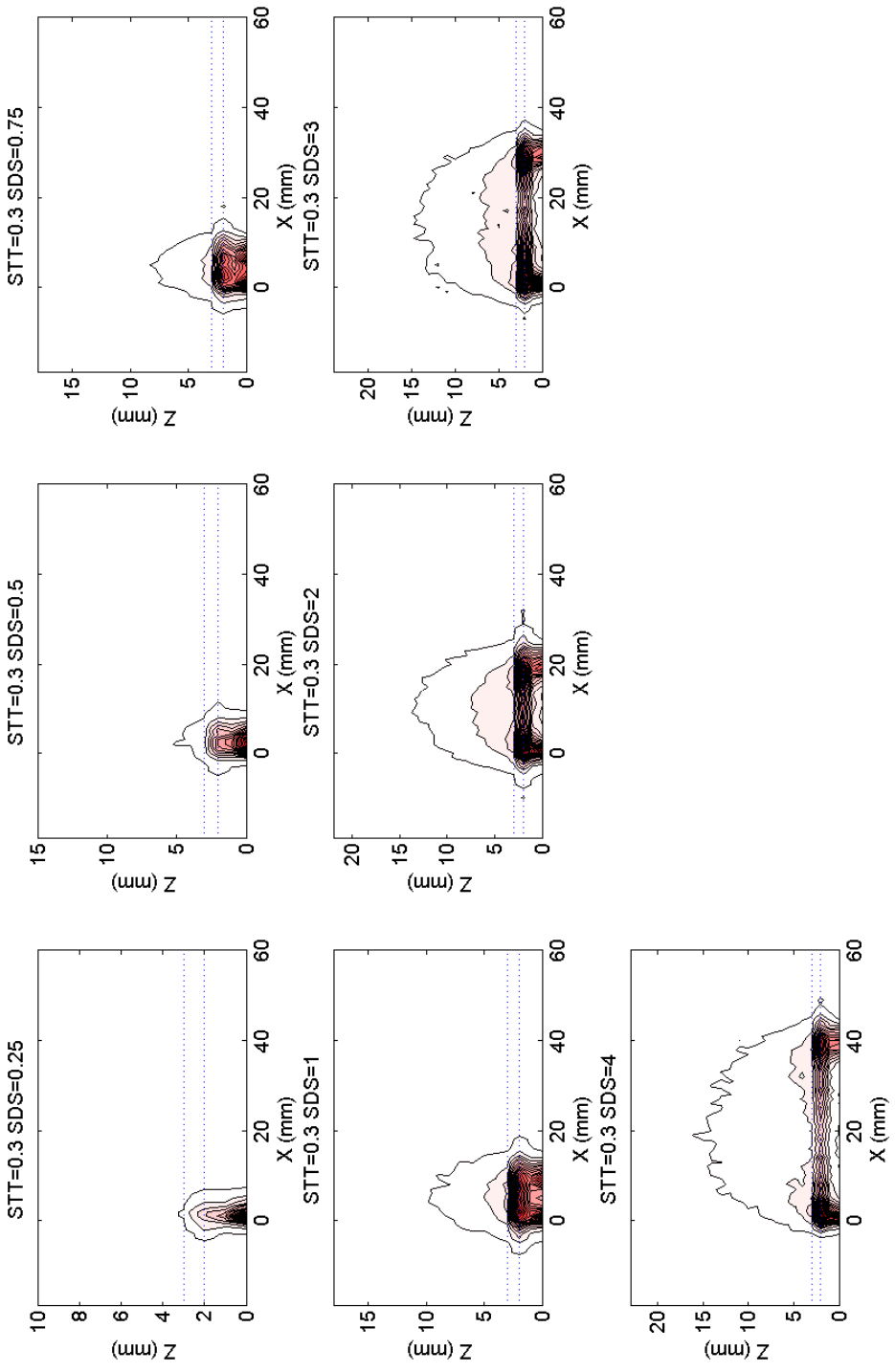
STT=0.3 SDS=0.25
STT=0.3 SDS=0.5
STT=0.3 SDS=0.75
STT=0.3 SDS=1
STT=0.3 SDS=2
STT=0.3 SDS=3
STT=0.3 SDS=4
Z (mm)
X (mm)

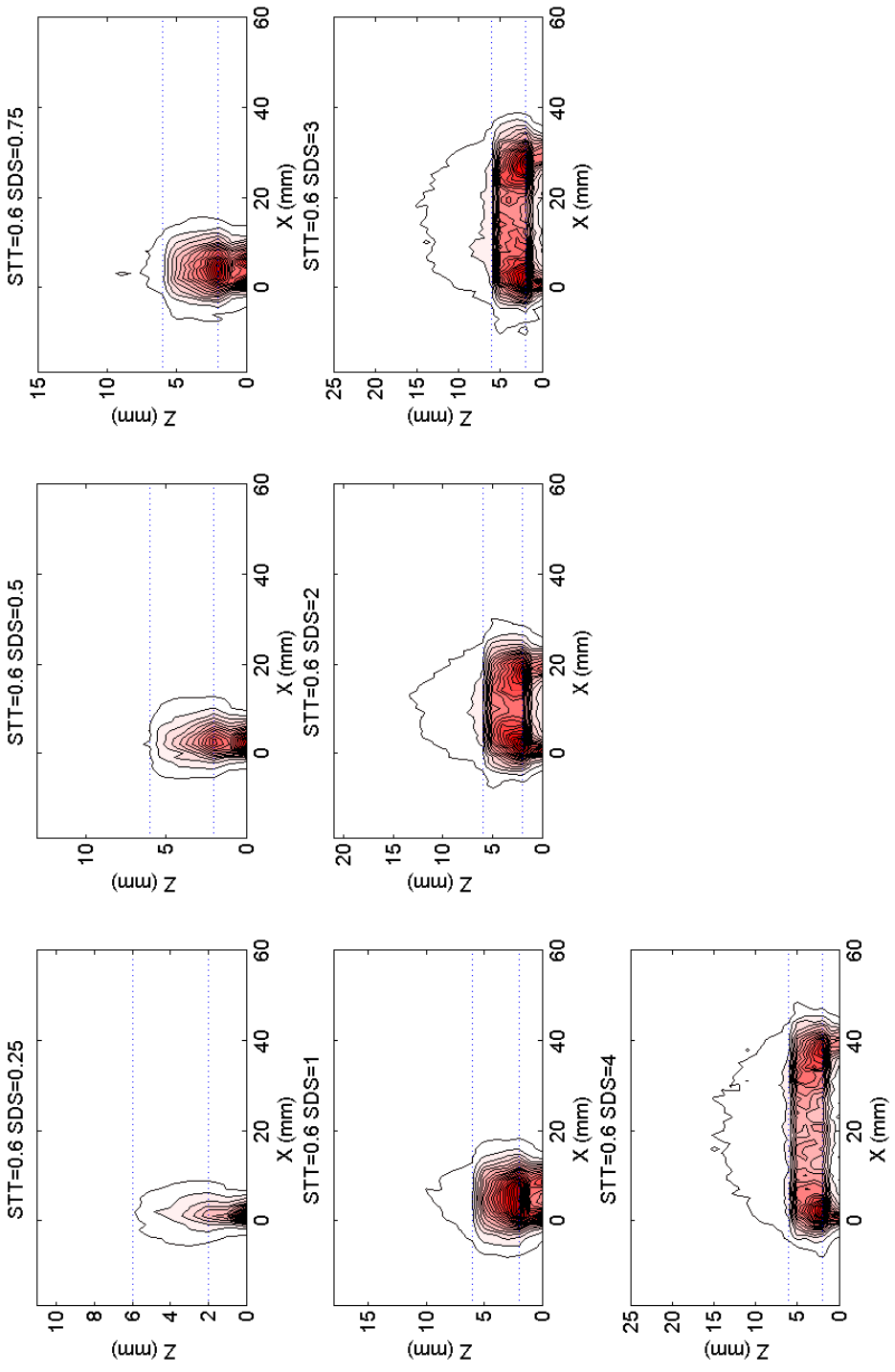
STT=0.6 SDS=0.25
STT=0.6 SDS=0.5
STT=0.6 SDS=0.75
STT=0.6 SDS=1
STT=0.6 SDS=2
STT=0.6 SDS=3
STT=0.6 SDS=4
Z (mm)
X (mm)

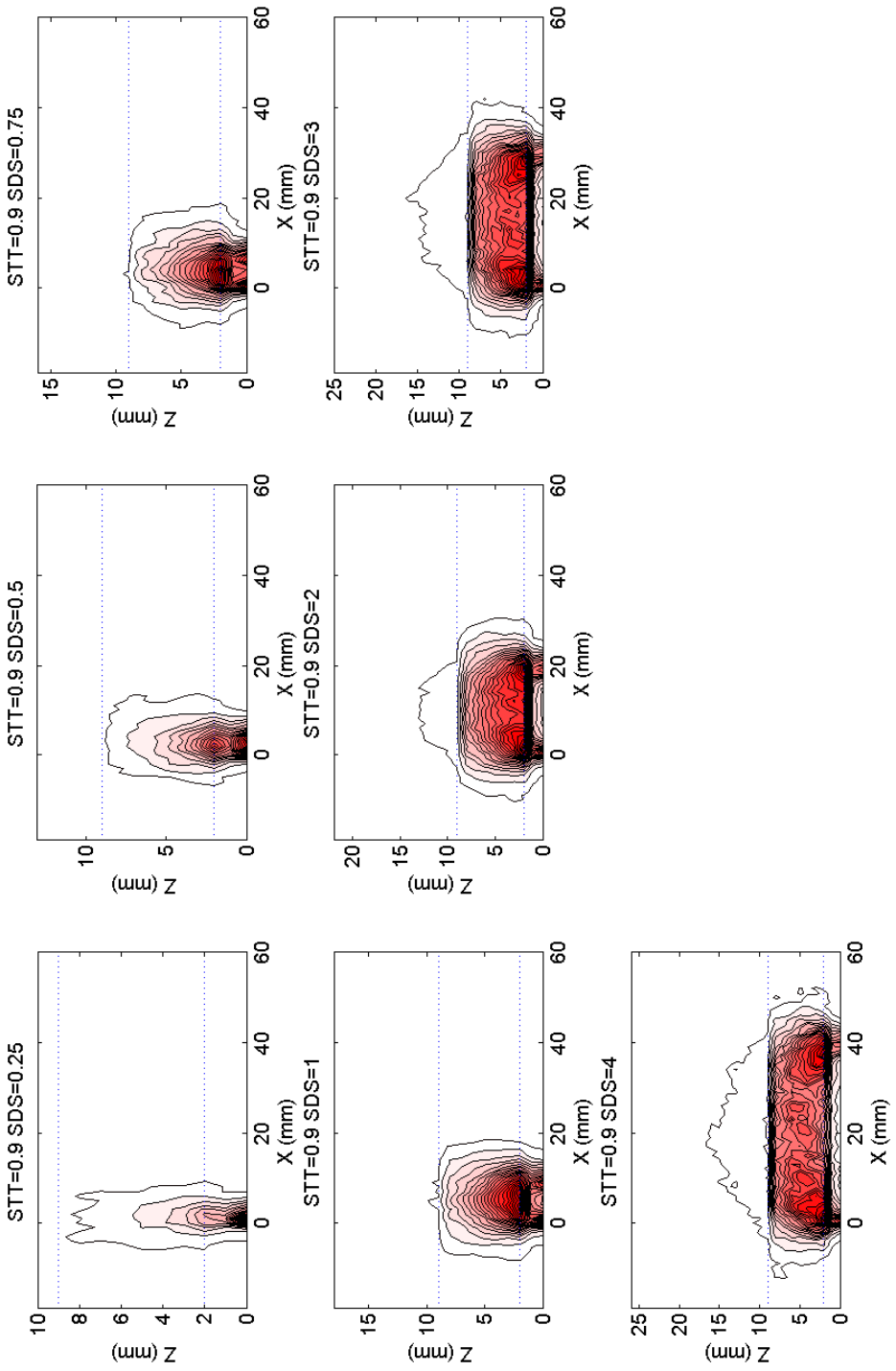
STT=0.9 SDS=0.25
STT=0.9 SDS=0.5
STT=0.9 SDS=0.75
STT=0.9 SDS=1
STT=0.9 SDS=2
STT=0.9 SDS=3
STT=0.9 SDS=4
Z (mm)
X (mm)

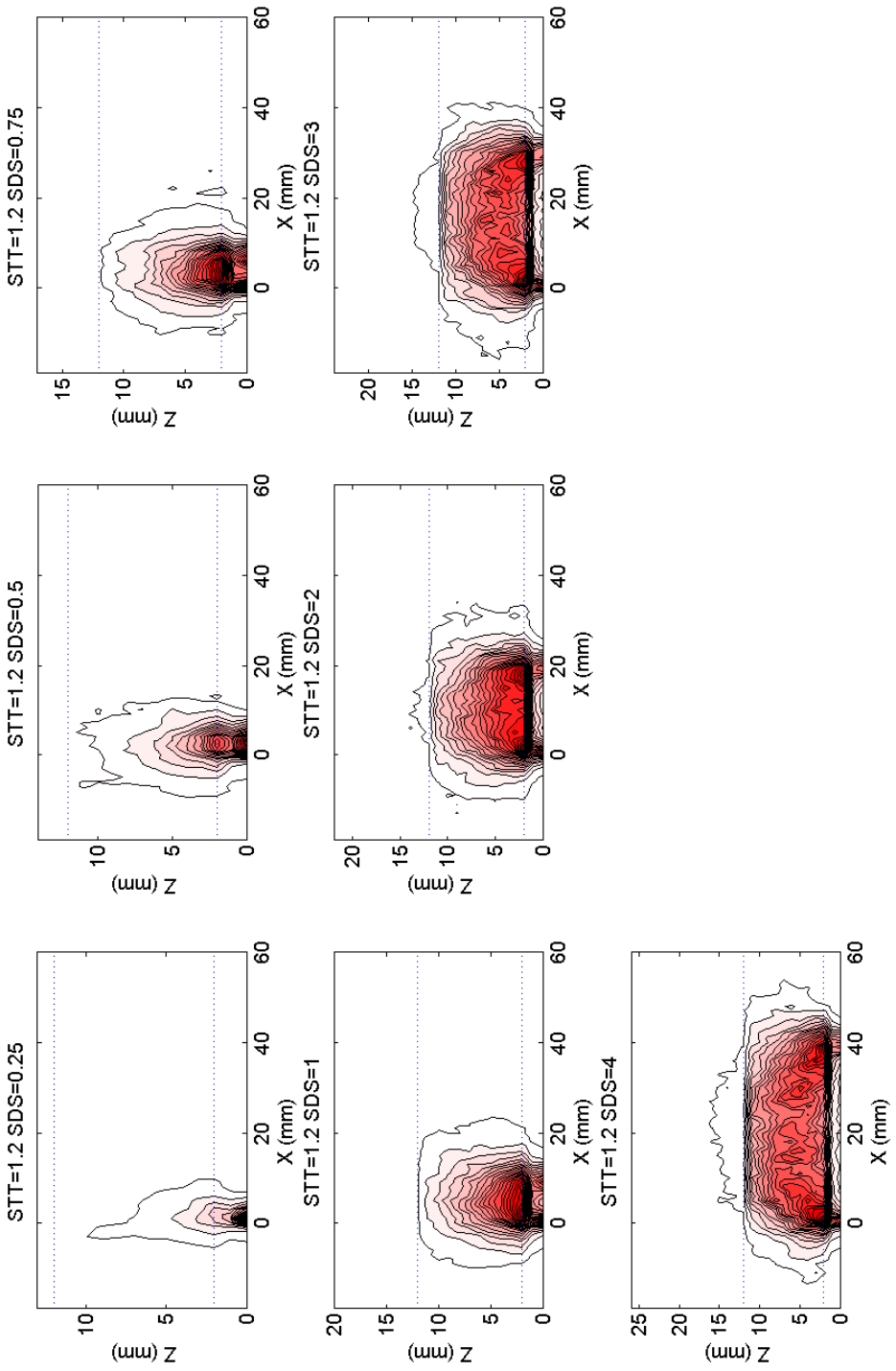
STT=1.2 SDS=0.25
STT=1.2 SDS=0.5
STT=1.2 SDS=0.75
STT=1.2 SDS=1
STT=1.2 SDS=2
STT=1.2 SDS=3
STT=1.2 SDS=4
X (mm)
Z (mm)

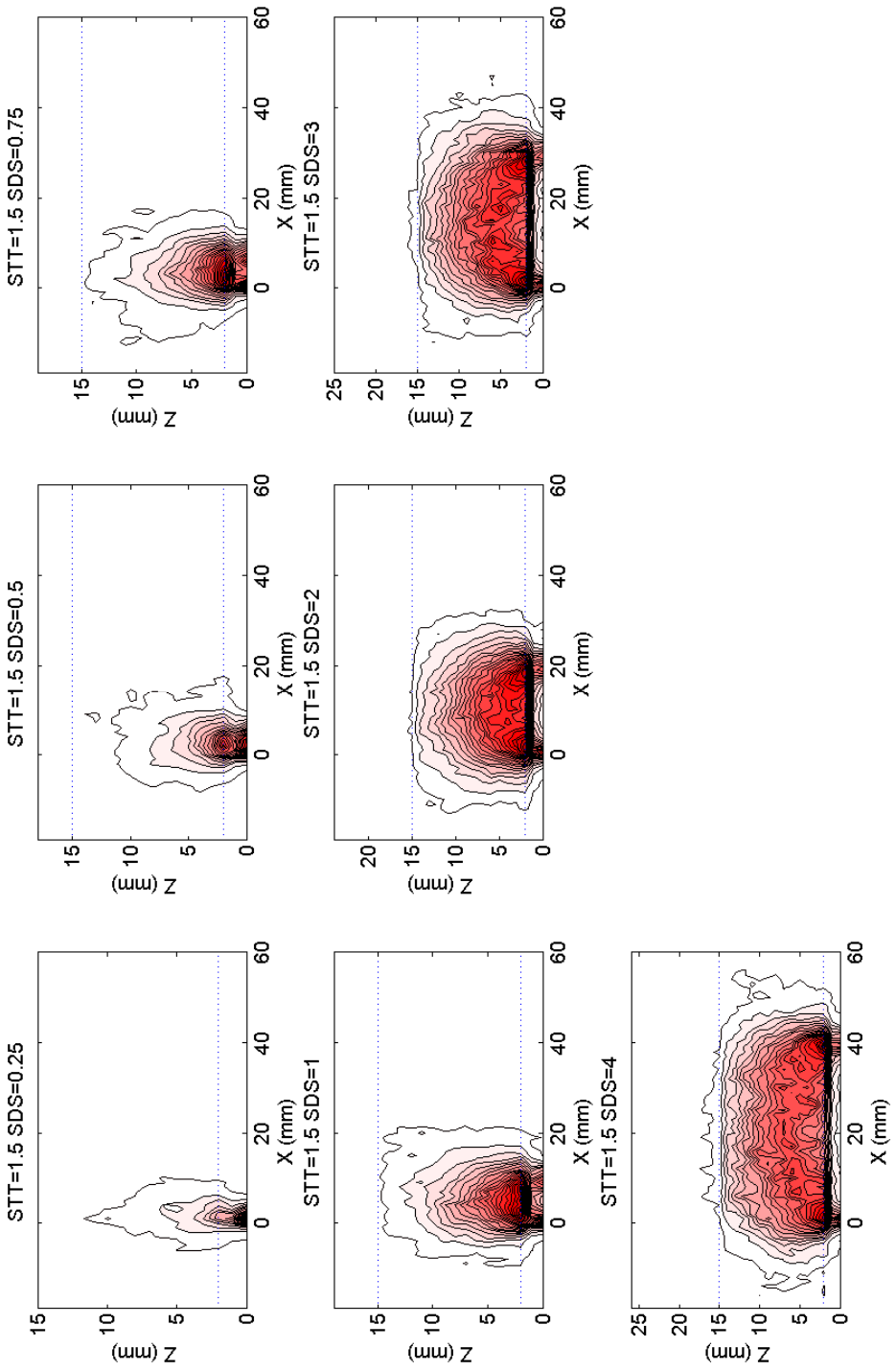
STT=1.5 SDS=0.25
STT=1.5 SDS=0.5
STT=1.5 SDS=0.75
STT=1.5 SDS=1
STT=1.5 SDS=2
STT=1.5 SDS=3
STT=1.5 SDS=4
Z (mm)
X (mm)

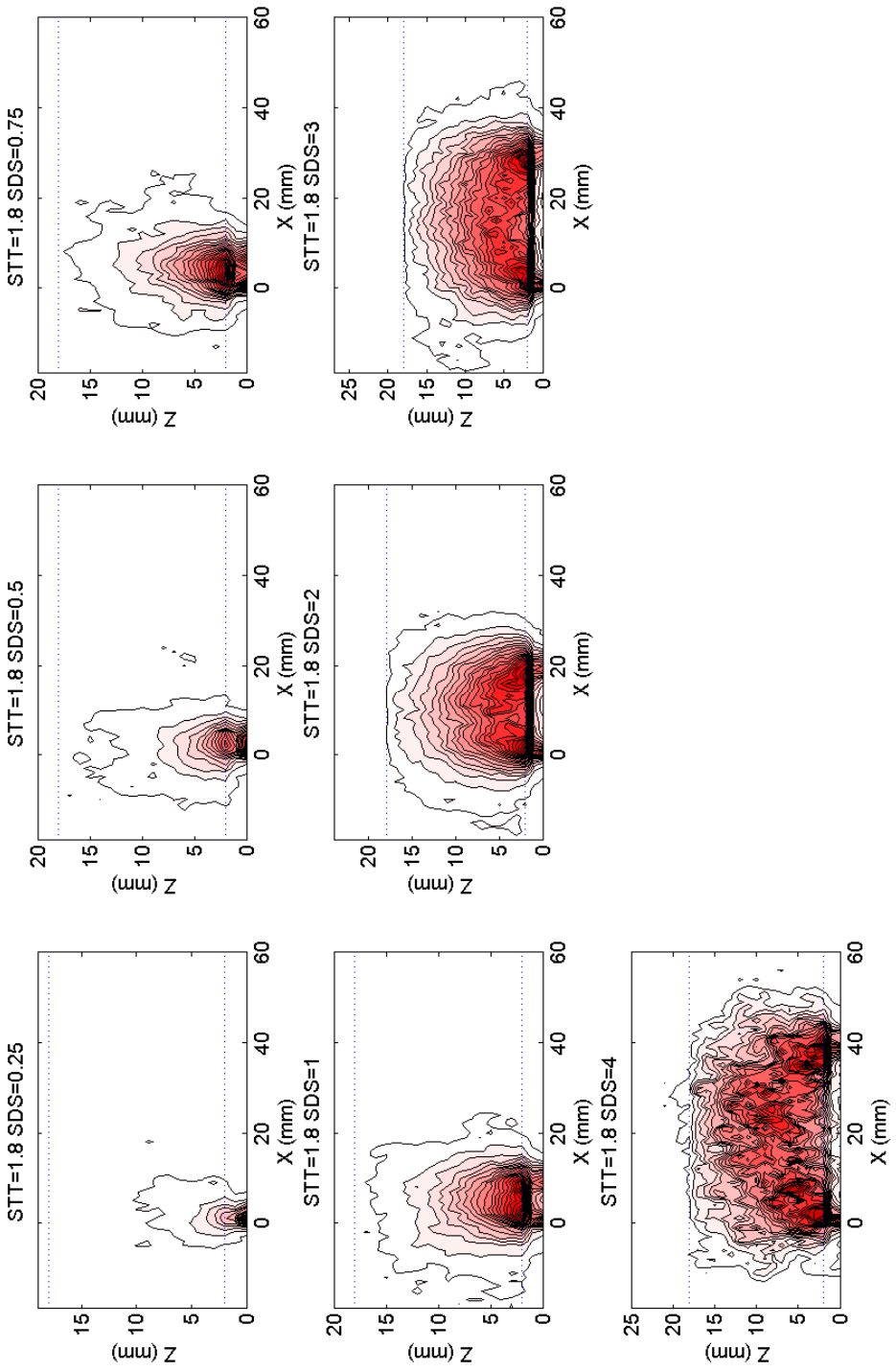
STT=1.8 SDS=0.25
STT=1.8 SDS=0.5
STT=1.8 SDS=0.75
STT=1.8 SDS=1
STT=1.8 SDS=2
STT=1.8 SDS=3
STT=1.8 SDS=4
Z (mm)
X (mm)

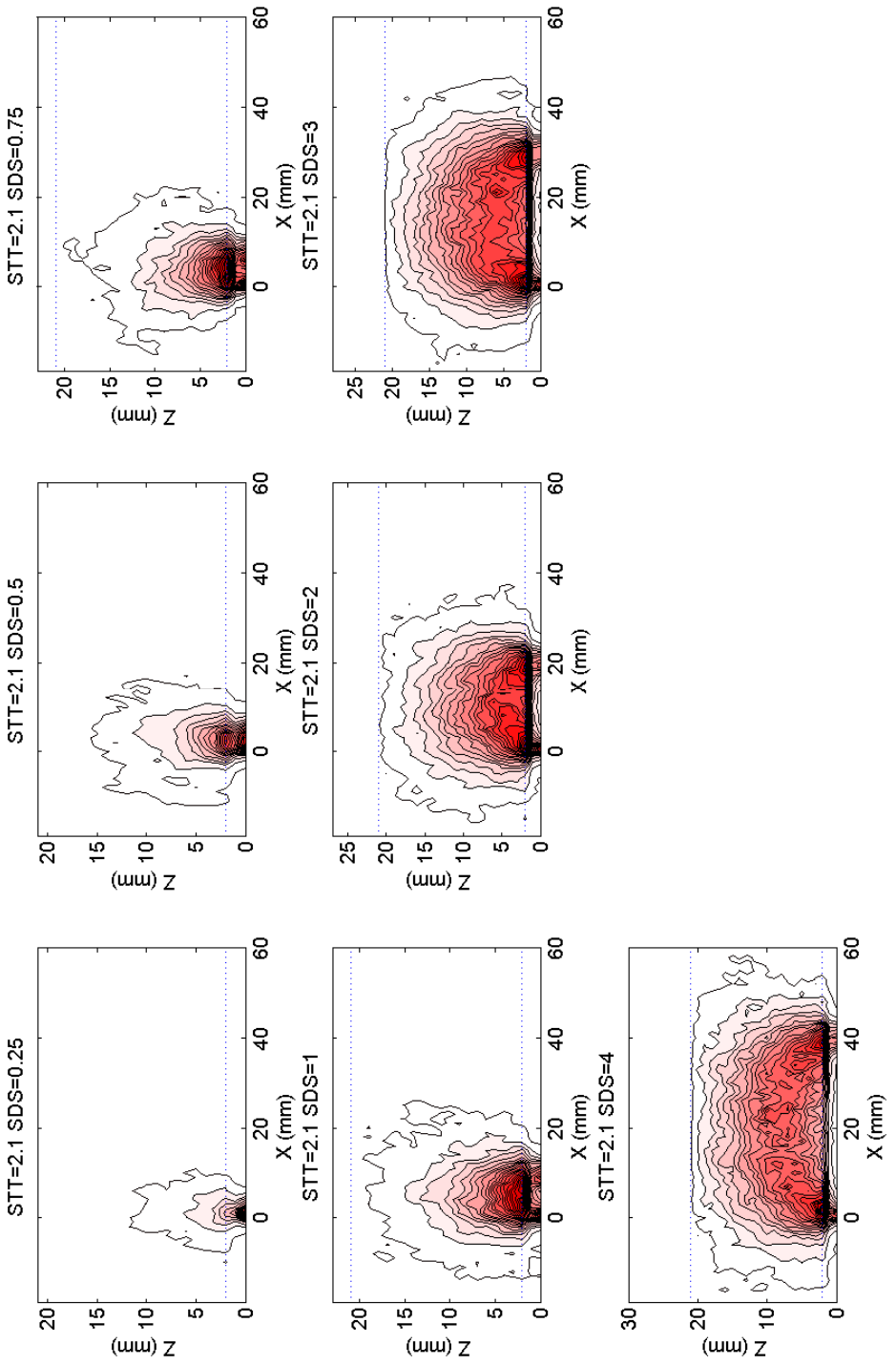
STT=2.1 SDS=0.25
STT=2.1 SDS=0.5
STT=2.1 SDS=0.75
STT=2.1 SDS=1
STT=2.1 SDS=2
STT=2.1 SDS=3
STT=2.1 SDS=4
Z (mm)
X (mm)

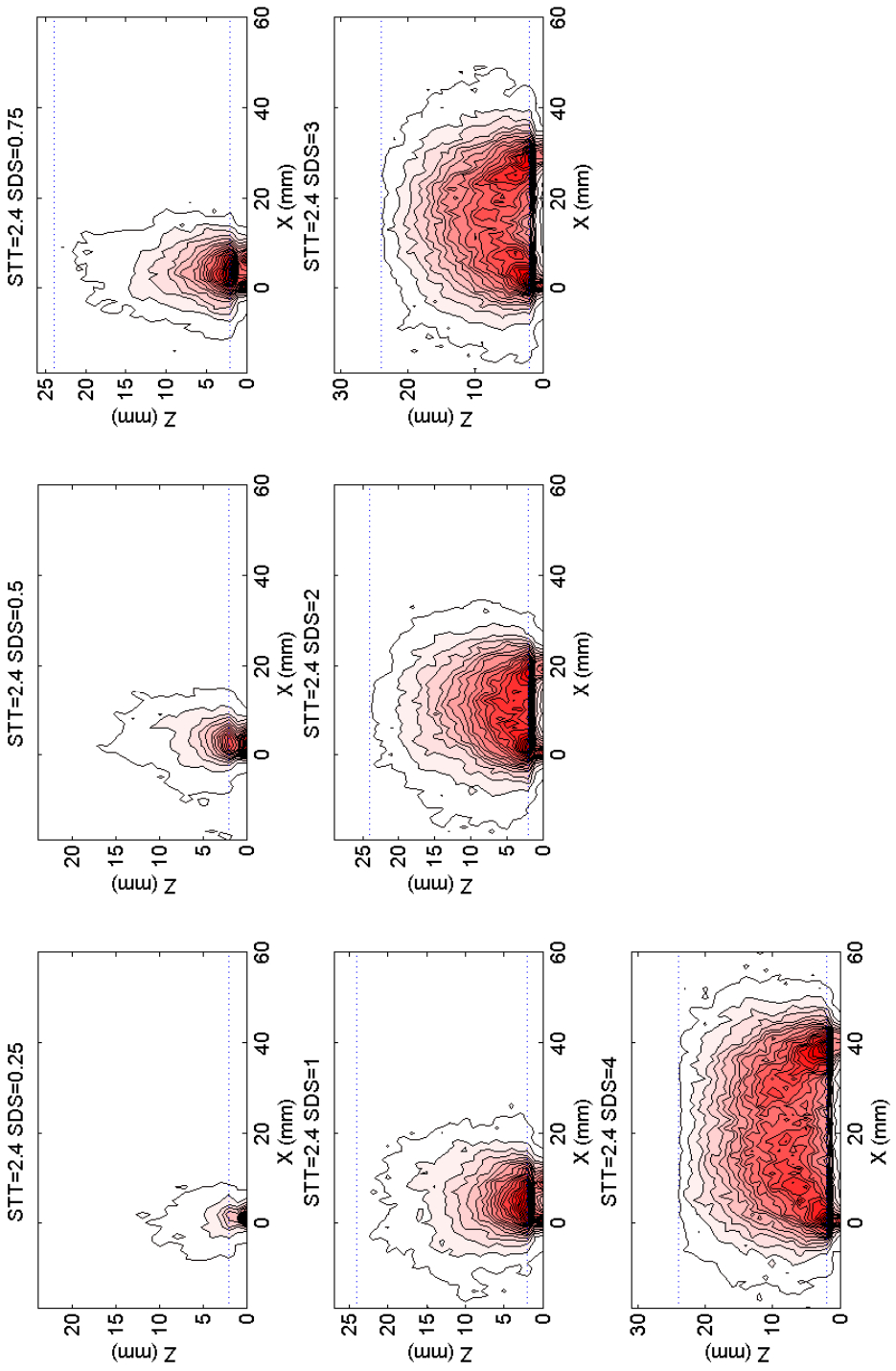
STT=2.4 SDS=0.25
STT=2.4 SDS=0.5
STT=2.4 SDS=0.75
STT=2.4 SDS=1
STT=2.4 SDS=2
STT=2.4 SDS=3
STT=2.4 SDS=4
Z (mm)
X (mm)